AEROSPACE REPORT NO.
ATR-78(7474)-1

CR 151596

Space Shuttle Pogo Studies

Prepared by R. F. COPPOLINO, M. H. LOCK, and S. RUBIN
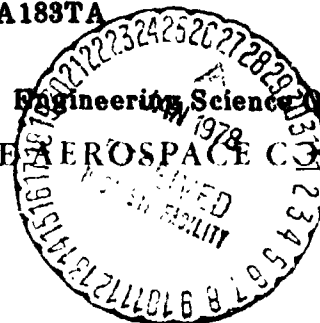**Vehicle Engineering Division**

October 1977

Prepared for
NATIONAL AERONAUTICS AND SPACE ADMINISTRATION
LYNDON B. JOHNSON SPACE CENTER
Houston, Texas 77058

Contract No. NAS9-14142
DRL T-1025
Line Item No. MA183TA

Engineering Science Operations

THE AEROSPACE CORPORATION

SPACE SHUTTLE POGO STUDIES

l7 October 1977

Prepared for

National Aeronautics and Space Administration
Lyndon B. Johnson Space Center
Houston, Texas 77058

Prepared by

R. N. Coppolino
M. H. Lock
S. Rubin

The Aerospace Corporation
El Segundo, California

SPACE SHUTTLE POGO STUDIES

Approved

S. Rubin, Senior Staff Engineer
Vehicle Integrity Subdivision
Vehicle Engineering Division

A.G. Norem, Director
Vehicle Integrity Subdivision
Vehicle Engineering Division

FOREWORD

This report describes the results of pogo stability investigations under-
taken at The Aerospace Corporation during the one-year period beginning
October 1975. These investigations were a continuation of the studies reported
in Ref. 4 under NASA contract NAS9-14142; the NASA(JSC) Technical Monitor
was Dr. H.H. Doiron. The authors would like to acknowledge the work of
R.E. Orth in programming support for the studies, the contribution to the
transfer function error analysis by Dr. J.S. Bendat, and the constructive
comments of Dr. Doiron during the course of the investigation.

ABSTRACT

Another phase of the study of pogo suppression during Space Shuttle Main Engine (SSME) operation was conducted as a follow-on to the study reported in Ref. 4. The latest available structural modal data (from model 5.3A) were incorporated and stability studies with the planar multiengine model were conducted for the lox system at the liftoff time of flight. The sensitivit of the system stability was determined selectively for dispersed values of certain critical system parameters on the basis of previous studies and recent experimental findings. The dispersions involved were (1) tolerance on structural natural frequencies, (2) increased downcomer axial motion in the 2.54-Hz structural mode along with high pump gains, (3) decrease resistance of the low pressure oxidizer turbopump (LPOTP), and (4) a large upward shift of the frequency of the upper SSME structural mode to about 30 Hz. In all cases the presence of the baseline accumulators virtually eliminated the destabilizations occurring in the absence of accumulators.

Studies of the stability consequence of reduced accumulator compliance at liftoff yielded a minimum recommended compliance equivalent to that provided by a gox volume of 0.007 m^3 (0.25 ft^3). A limited study of the consequence of accumulator failure showed that loss of function of the upper SSME accumulator led to instability under toleranced conditions in the shifted upper SSME structural mode.

Although not investigated in this study, it should be noted for completeness that previous investigations have identified a potential for instability in the separation mode introduced by the accumulator (fluid oscillation between accumulator and the high pressure oxidizer turbopump (HPOTP). These earlier studies showed that accumulator resistance can be highly effective in eliminating such an instability.

Study of the refinement of the analytical model of the LPOTP was initiated by investigation of curve fitted transfer functions and by the formulation of a first-cut physical model, all based upon recent data from dynamic testing of a quarter-scale model impeller. Although both approaches showed promise, certain questions remain to be resolved before an implementation into the system stability model can be made with confidence. Further studies are planned.

A preliminary sensitivity analysis for pogo stability during operat n of the orbital maneuvering subsystem (OMS) was performed. Included were the development of OMS pod structural and propulsion system models. The results of the study revealed a strong destabilizing interaction in a high-gain engine axial mode, as well as a potential for other destabilizing interactions. An initial evaluation indicated the possible benefit of small accumulators.

Investigations were made of various sources of error in the experimental measurement of frequency response functions as a result of system noise. An error estimate was developed to account for random errors due to the noise, with application to both fixed and swept frequency sinusoidal testing. Application to the planning of a test was exemplified. The results are meaningful for the planning and interpretation of dynamic response from propulsion tests.

CONTENTS

CONTENTS

CONTENTS (Concluded)

TABLES

FIGURES

FIGURES (Continued)

FIGURES (Concluded)

NOMENCLATURE

Units: M (mass), F (force), L (length), T (time)

a, b	factors
a_x^2, a_y^2	mean square error quantities for x, y: Eqs. (48) and (49)
A	area, $[L^2]$
B	fluid bulk modulus, $[FL^{-5}]$
B_e	effective analysis bandwidth, Hz, $[T^{-1}]$
C	fluid compliance (volume change per pressure change) $[F^{-1}L^5]$
E[ ]	expected value of bracketed quantity
EI	flexural stiffness, $[FL^2]$
f	frequency, Hz, $[T^{-1}]$
F	force, $[F]$
g	gravitational acceleration, $[LT^{-2}]$
$G_{xx}(f)$	autospectral density function for x(t)
$G_{xy}(f)$	cross-spectral density function for x(t) and y(t)
h	length or fluid head, $[L]$
H	pump blade spacing, $[L]$
$H_{xy}(f)$	frequency response of y(t) relative to x(t)
i	imaginary unit, $\sqrt{-1}$
i(t)	external excitation
I	identity matrix
K	dilatational stiffness constant, $[FL^{-5}]$, or stiffness matrix
K_c	coefficient matrix for combustion state equations

NOMENCLATURE (Continued)

ℓ_t	tank length, $[L]$
L	inertance, $[FL^{-5}T^2$ or $ML^{-4}]$
$\dot{m}$	oscillatory mass flow, $[MT^{-1}]$
$m+1$	pump gain
$m(t), n(t)$	self-noise signals in $x(t), y(t)$
M	mass $[M]$, or mass matrix
M_{tfp}, M_{top}	fuel, oxidizer tank propellant mass at 100% fill condition, $[M]$
M_{tfs}, M_{tos}	fuel, oxidizer tank structural mass, $[M]$
$\mathcal{M}$	bending moment, $[FL]$
n_d	number of independent estimates in FFT spectral analysis
P	oscillatory pressure, $[FL^{-2}]$
$\bar{P}_v$	vapor pressure, $[FL^{-2}]$
q	generalized displacement vector
Ω	oscillatory volumetric flow $[L^3T^{-1}]$
$\hat{r}$	rms uncertainty radius on $\hat{H}$
R	resistance, $[FL^{-5}T]$
s	Laplace variable, $s = \sigma + i\omega$, $[T^{-1}]$
$T(f)$	analysis time for sinusoidal signal at frequency f, $[T]$
T_{total}	total analysis time, $[T]$
$u(t), v(t)$	response in $x(t), y(t)$ caused by $i(t)$
u_o, v_o	sinusoidal amplitude of $u(t), v(t)$
U_a	pump inlet axial velocity, $[LT^{-1}]$

U_{tip}	tip speed of pump inducer, $[LT^{-1}]$
V, v	generalized velocity vectors, Eqs. (30) and (40), respectively
x	structural displacement, $[L]$
X_c	vector of chamber state variables $(X_1 \ldots, X_8)$
$x(t), y(t)$	measured system responses; $x(t) = u(t) + m(t)$, $y(t) = v(t) + n(t)$
$z(t)$	noise in single-input/single-output model; Figure F-2
a, β	noise-to-signal ratio for $x(t)$, $y(t)$; Eq. (F-3)
$\gamma_{xy}^2(f)$	coherence function between $x(t)$ and $y(t)$
Γ	load distribution matrix
$\Delta \zeta$	damping loss due to feedback
$\Delta \hat{\phi}_{xy}$	rms uncertainty of ϕ_{xy}
ϵ	normalized rms error
ζ, ζ_o	damping ratio, open loop modal damping ratio
θ	circumferential angle
Θ	relative volumetric flow displacement, $[L^3]$
μ, ν	OMS, RCS tank fractional fill levels
ρ	fluid density $[ML^{-3}]$
σ_p	pump cavitation number, $(\overline{P}_u - \overline{P}_v)/\frac{1}{2}\rho U_{tip}^2$
τ_r	chamber residence time, $[T]$
τ_{df}, τ_{do}	fuel, oxidizer combustion delay times, $[T]$
φ	mode shape parameter
ϕ	mode matrix

ϕ_{xy}	phase angle of H_{xy}; Eq. (F-7)
ψ	constraint matrix
ω	angular frequency, $[T^{-1}]$
ω_o	open loop structural mode frequency, $[T^{-1}]$
Ω	pump flow impedance parameter, Eqs. (14) and (15)

Subscripts and Location Designators

a	accumulator
c	chamber
d	downstream
e	engine
f	fuel
hp	high pressure pump
j	injector
ℓ	line
ℓp	low pressure pump
c	oxidizer
p	pump or propellant
s	structural
t	tank
t'	tank bottom
u	upstream

Special Notation

(	estimate of quantity

underline denotes nondimensionalized quantity

NOMENCLATURE (Concluded)

Abbreviations

ALRC	Aerojet Liquid Rocket Company
DOF	degree of freedom
FFT	fast Fourier transform
LPOTP	low pressure oxidizer turbopump
MDAC	McDonnell Douglas Astronautics Company
MPS	main propulsion subsystem
OME	orbital maneuvering engine
OMS	orbital maneuvering subsystem
RI/SD	Rockwell International/Space Division
SSME	Space Shuttle main engine

1. POGO SUPPRESSION FOR MAIN PROPULSION SUBSYSTEM OPERATION

This section of the report describes the continuation of the stability studies undertaken by The Aerospace Corporation in support of pogo suppression during operation of the main propulsion subsystem (MPS). Earlier studies presented initial analyses of the Shuttle pogo susceptibility (Ref. 1) and the use of single equivalent engine stability models to investigate the effectiveness of passive and active suppressors (Refs. 2 and 3, respectively). These studies were followed by the development of a multiengine pitch-plane stability model (Ref. 4) under the initial phase of the current contract with the NASA Johnson Space Center (JSC).

Included in this section are an outline of the analytical model and numerical procedures employed to determine the system stability, a discussion of the numerical input data for the structure and the propulsion system, and the results of the updated stability analyses.

1.1 ANALYTICAL MODEL AND NUMERICAL PROCEDURES

The launch configuration of the Space Shuttle, shown in Figure 1, comprises the orbiter vehicle, and external tank, and two solid rocket boosters. The external tank contains a forward liquid oxygen tank and an aft liquid hydrogen tank for supply of the three SSME's located on the orbiter vehicle. The relative location of the lox tank and the SSME's (see schematic in Figure 1) necessitates an extensive length of feedline. The total length is about 40 m (130 ft), which introduces several propulsion system modes in the frequency range of interest.

The multiengine pitch-plane model developed in Ref. 4 was employed as the basis for the present system stability analysis. The model comprises the vehicle structure, the SSME's and the elements of the MPS associated with the lox circuit. The hydrogen system does not appear in the model since early assessment of the pogo problem indicated that the hydrogen system
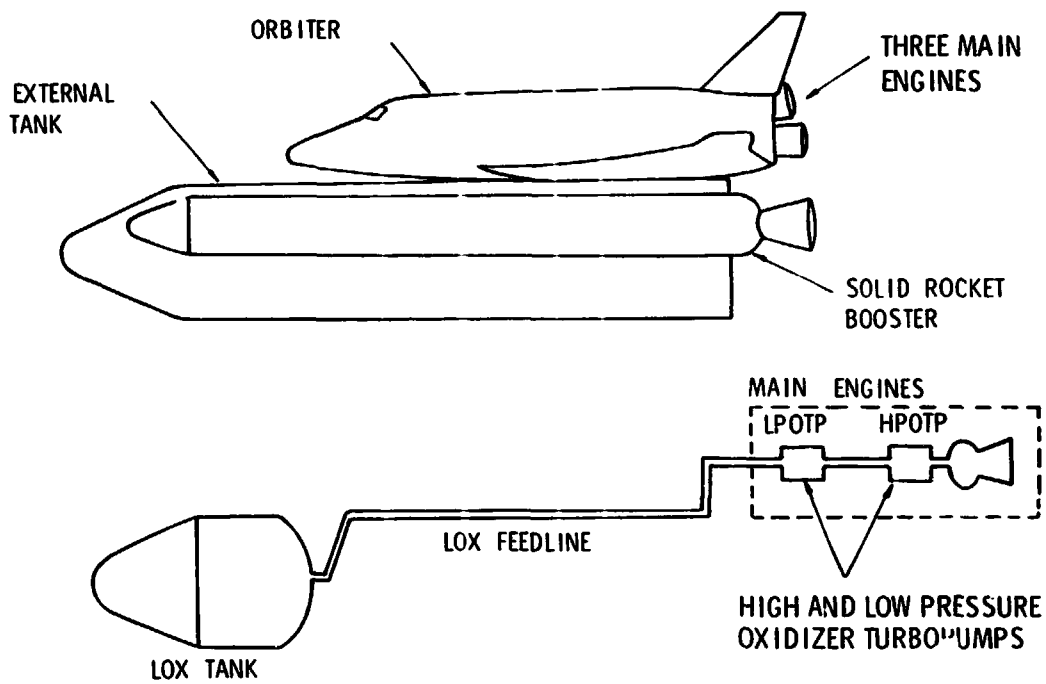
Figure 1. Schematic of Space Shuttle and Lox Circuit
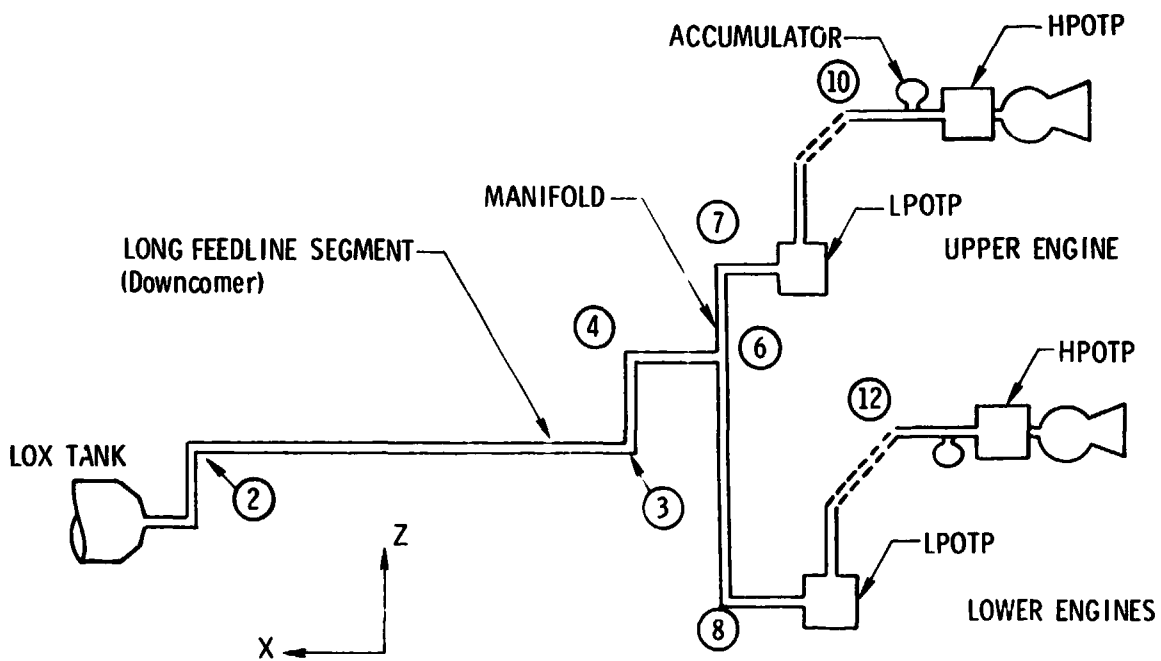
Figure 2. Schematic of Multiengine Model

was a less likely contributor to potential instability. The geometric arrangement of the model is shown in Figure 2 and the associated system equations are presented in Appendix A. Observe that only one lower engine is illustrated in the figure since the motion of both lower engines is identical for this pitch-plane model.

To assure a good description of the higher organ-pipe modes of the lox feedline, the flow in the long feedline segment that is located along the external tank (the element between points ② and ③ in Figure 2) was represented by the exact solution for one-dimensional continuous compressible flow (Ref. 1). The fluid flow in the remaining feedline segments and in the inter-pump ducts was described by a combination of incompressible flow segments and local compliances to represent liquid compressibility corrected for pipe radial elasticity. The compliances were located at feedline corners and at the inlets and outlets of the low and high pressure oxidizer turbopumps. The resulting flow description provided an adequate representation of distributed compressibility effects in these line elements for frequencies up to 30 Hz. Comparison of the lox system modal frequencies predicted in this manner with those determined from a fully compressible model showed acceptable agreement for this range.

The dynamic behavior of the LPOTP's and the HPOTP's was described by the following equations relating the downstream pressure P_d, and flow Q_d, to the upstream pressure P_u, and flow Q_u.

$$P_d = (m+1)P_u - (Ls + R)Q_d$$

$$Q_d = Q_u - sC_p P_u \tag{1}$$

where L, R, C_p and m+1 denote frequency independent inertance, resistance, compliance, and pump gain, respectively; s is the Laplace variable used to denote the complex frequency. This "elementary" pump model has been used in the pogo stability analysis of Titan, Thor, Delta, Atlas and Saturn boost

vehicles (Ref. 5). Until the tests performed on the LPOTP model impeller, by Caltech in 1976 (Ref. 6), there was no experimental basis for a more refined representation of the dynamic behavior of the cavitating turbopump.

The accumulators used for pogo suppression were represented by an inlet liquid inertance and a gas compliance. The program also includes a capability for the input of accumulator resistance; however, this capability was not employed in the present analyses. For these studies, the accumulator is located two line diameters upstream of the inlet flange of each HPOTP. This separation is significant in that it both influences the effectiveness of the accumulator and introduces a new propulsion system mode of vibration, termed the "separation" mode, that provides an additional possibility for instability (Refs. 4 and 7). This particular separation represents a worst case interpretation of the Shuttle system requirements.[*]

The computer mechanization of the analytical model of the system allowed for representation of the motion of the Shuttle vehicle by a series of up to ten pitch-plane structural modes. Tank dynamic outflow effects are included in the generalized force terms on the basis that the structural modes used in the analysis were developed with closed-bottom tanks (Ref. 1). The eigenvalues and eigenvectors of the coupled structural/propulsion system were developed from the condition that the determinant from the equations for free vibration of the coupled system vanishes. Transcendental functions appear within the determinant because of the exact distributed representation of the downcomer flow and the provision for arbitrary phase shifting of the engine thrust forces. The solutions of the characteristic equation were determined with the use of an iterative root-finding subroutine (Ref. 8) that used the input structural mode frequency and previously calculated propulsion system frequencies as initial guesses.

---

[*]The system requirements called for the accumulator to be located no more than 0.33 m (13 in.) from the pump inlet flange (approximately two line diameters); the actual location is 0.17 m (7 in.) from the inlet.

1.2   NUMERICAL INPUT DATA

The structural modal data used in the analysis consisted of frequencies and amplitudes of a selected set of pitch plane modes developed from Shuttle model 5.3A and provided by Rockwell International/Space Division. The earlier model 4.3 data were employed in the previous study (Ref. 4). The modes selected by Rockwell were based upon the magnitude of the modal amplitudes for those elements of the system that were of concern in the pogo problem (i.e., engine gimbals, feedline corners, etc.) for frequencies up to 30 Hz. Although such modal sets were provided for seven flight conditions, this analysis dealt only with the liftoff event. In the assignment of modal amplitudes, the corners immediately upstream of the LPOTP and HPOTP positions (points ⑦, ⑧, ⑩ and ⑫ in Figure 2) were assigned the same motion as the associated pump. The motion of the manifold and the longitudinal displacement of the corner immediately ahead of the manifold (points ⑥ and ④ in Figure 2) were assumed to be zero; this assumption was necessitated by the fact that the structural definition was not sufficiently adequate to define these modal motions. The assumption was not considered to be critical since the length of the feedline segment between points ④ and ⑥ was small compared to the length of the downcomer. This relative insensitivity had also been confirmed by results in Ref. 4. Examples of the structural mode shapes employed in the analysis are given in Appendix B, where the data for the second and fifty-fourth modes at liftoff are provided. These modes proved to be of particular interest from the stability analyses. To account for damping in the vehicle structure, a critical viscous damping ratio of 0.01 was assigned to each structural mode.

The cross-sectional area, length, and radial elasticity of the various lines were based upon available design data. The resistance and inertance of the lines, pumps, engine, and thrust chamber were developed from the basic data given in the SSME Engine Dynamic Model (Ref. 9). The values of these parameters are provided in Appendix B, together with the local compliance values employed in the feedline description. Values for the pump cavitation

compliances and their uncertainty ranges as a function of net positive suction head (NPSH) were based upon the empirical studies of Ref. 10 and applied to the Shuttle pumps in Ref. 1. The pump gain, m+1, was related to the compliance based upon an empirical relationship developed from unpublished Titan and Delta vehicle studies.

$$m+1 = 1 + 3000 \, \rho g \, C_p/A_i \tag{2}$$

where ρ is the liquid density, g is the gravitational constant, and A_i is the flow area at the pump inlet. The variations with flight time of the estimated nominal values of the compliance and gain parameters are illustrated in Figures 3 and 4. The source of the operating pressures versus time is the Space Shuttle Pogo Data Manual (Ref. 11). The nominal, maximum and minimum values of compliance, and the corresponding pump gains for the liftoff event are provided in Table 1.

1.3   PROPULSION SYSTEM MODES

Knowledge of the propulsion system modes not only provides initial guesses for the numerical determination of the eigenvalues of the coupled system, but also facilitates increased understanding of the coupling processes revealed by the stability analysis. Vibration modes of the propulsion system were determined with and without the baseline $0.017 \, \text{m}^3$ $(0.6 \, \text{ft}^3)$ gaseous oxygen (gox) accumulators. The calculations were undertaken using the Aerospace nominal values for the pump parameters. The frequencies calculated for the liftoff condition are shown in Figure 5, together with the frequencies of some of the structural modes of interest; the numbers of some of the structural modes are also provided in the figure. Examination of the associated mode shapes of the propulsion system indicated that certain distinct types of modes could be identified.

One such type was an "inter-engine" mode wherein the predominant modal perturbations took place within the engines and the feedline run between the engines. Two of the propulsion system modes calculated in the frequency
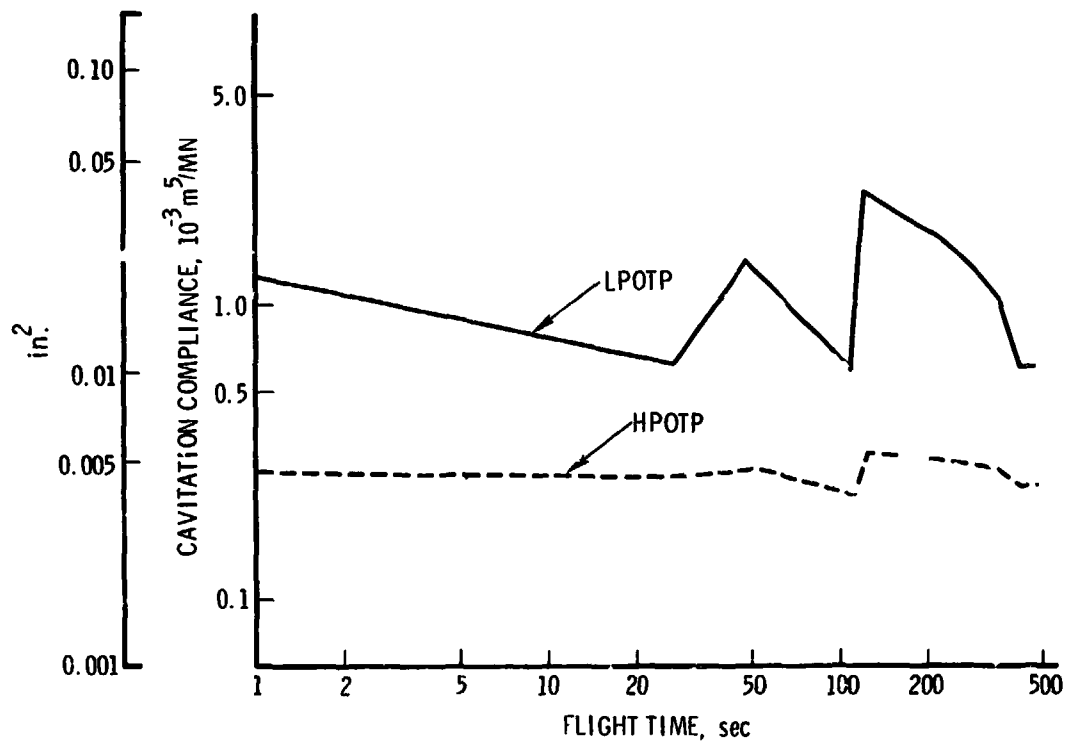
Figure 3. Variation of Nominal Pump Cavitation Compliance
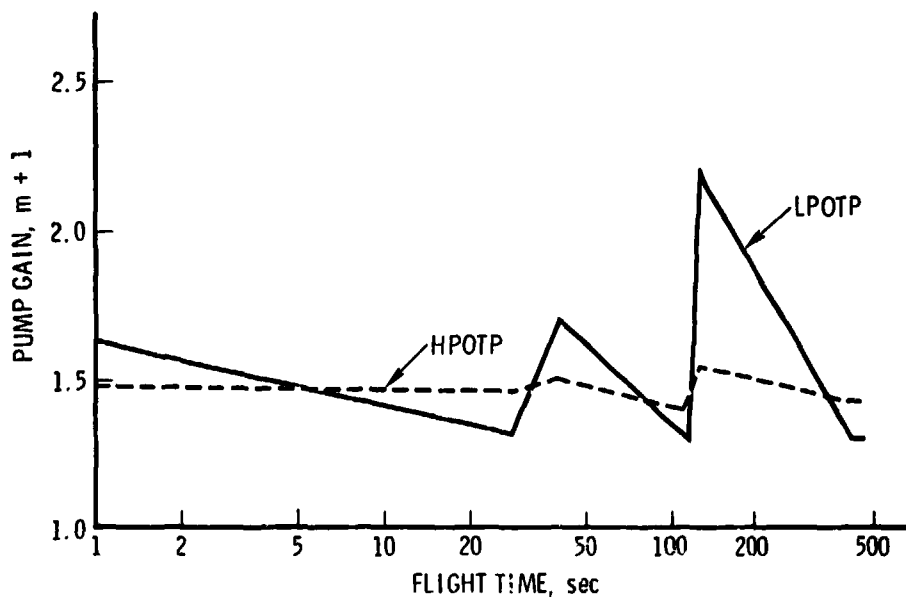
Figure 4. Variation of Nominal Pump Gain

1-7

Table 1. Values for Pump Gain and Pump Cavitation
Compliance at Liftoff

Parameter	Value
LPOTP Gain, $m_1 + 1$	$1.48/2.23/1.10^*$
HPOTP Gain, $m_2 + 1$	$1.63/3.64/1.24$
LPOTP Compliance, C_{p1}	
$10^{-3} m^3/(MN/m^2)^{**}$	$1.0/2.4/0.18$
$(10^{-2} in.^2)$	$(1.6/4.0/0.3)$
HPOTP Compliance, C_{p2}	
$10^{-3} m^3/(MN/m^2)$	$0.36/1.5/0.14$
$(10^{-2} in.^2)$	$(0.60/2.5/0.23)$

*Nominal/maximum/minimum values provided for all
entries
**Compliance in SI units is a volume change per unit
pressure change; in English units, it is the weight of
liquid displaced per unit pressure change.

range of interest had been identified as being of this type and the frequencies
are designated with an I/E notation in Figure 5; the distribution of fluid
amplitudes associated with the first of these modes is illustrated in Figure 6.
As noted in the figure, the fluid flow is identical in the two lower branches
(the figure only shows one of the lower branches). In the case of a system
without accumulators it will be noted from the results presented in Figure 5
that the addition of the baseline accumulator has a dramatic effect on the
frequency of the first inter-engine mode, the frequency being reduced from
about 14 Hz to around 3.5 Hz by the addition of the accumulator. The fre-
quency of the second inter-engine mode is only slightly affected by the ac-
cumulator.

Another mode was identified as an "inter-pump" mode and the asso-
ciated frequency is designated I/P in Figure 5. This particular mode involves
a considerable amount of fluid motion between the compliances provided by
the LPOTP and HPOTP cavitation. Although the overall mode shape did not
exhibit a pure inter-pump character, the mode was identified in this manner
since the frequency was estimated reasonably well by the following formula
for pure interpump action:

$$f_i = \frac{1}{2\pi} \left(\frac{1/C_{p1} + 1/C_{p2}}{L_i + L_{p1}} \right)^{1/2} \tag{3}$$

where L_i, L_{p1} denote the inertance of the inter-pump line and of the LPOTP,
respectively; and where C_{p1}, C_{p2} denote the cavitation compliance values at
the inlet to the LPOTP and HPOTP, respectively. The incorporation of the
baseline accumulator reduced the frequency of this mode from about 19 Hz
to around 11 Hz. The remaining propulsion system modes shown in Figure 5
have shapes associated with acoustic modes of the feedline from the tank.
The frequencies of these acoustic modes lie within the frequency bands de-
fined by the open-open and open-closed modes of the feedline, and there is
relatively little participation within the engines. This character is illustrated
in Figure 7, where the frequencies and associated damping ratios for the
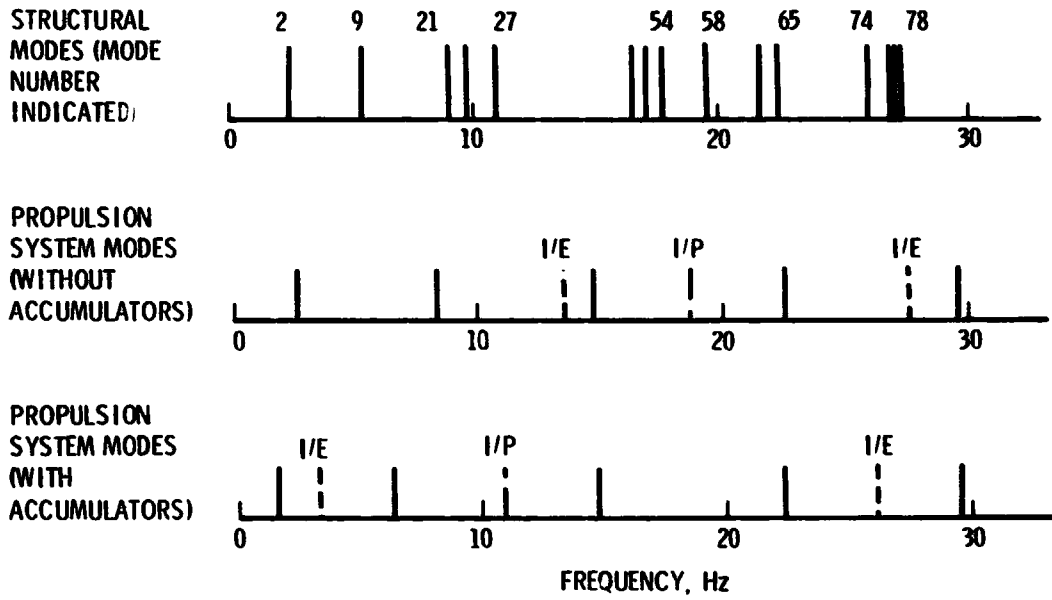
Figure 5. Structural and Propulsion System Modal Frequency
Spectra at Liftoff
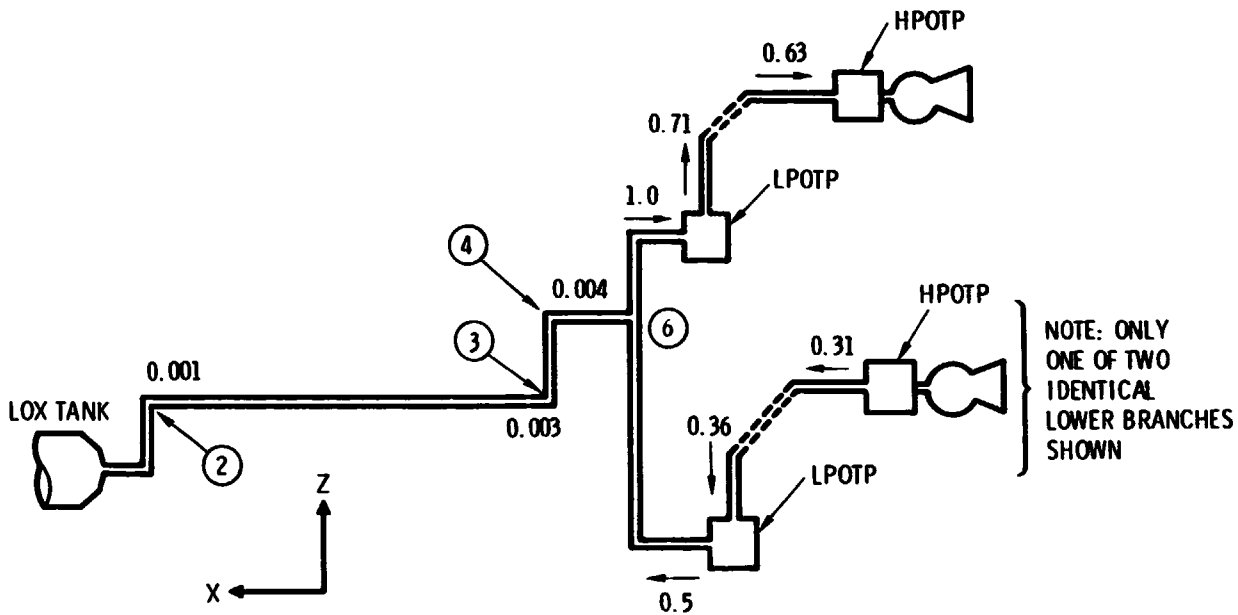
Figure 6. Amplitudes in the First Inter-Engine Fluid Mode
at Liftoff

propulsion system modes are given for the cases of a system without accumulators and a system with the baseline accumulators. The figure shows that the higher feedline modes are lightly damped and that the inter-pump and inter-engine modes are relatively highly damped. Figure 7 shows that the frequency reductions in the feedline-type modes, due to the presence of the baseline accumulators, becomes insignificant above the lowest two modes. This behavior occurs since the presence of the LPOTP compliance is serving to provide a nearly open boundary condition for the higher feedline-type modes.

Finally, it should be noted that the frequency of the separation mode (i.e., the propulsion system mode associated with the fluid between the accumulator and the HPOTP inlet cavitation bubble) lies above the frequency range of interest for the Aerospace nominal values of the pump parameters (namely, 38 Hz). The effect of this mode on the system stability was not investigated in the present study. However, it should be remarked that previous investigations (Refs. 4 and 7) have shown that this fluid mode represents another potential source of instability. These studies indicated that accumulator resistance is highly effective in eliminating such instabilities.

1.4   STABILITY ANALYSIS RESULTS

The stability analyses focused upon the liftoff event. A total of thirteen structural modes was analyzed to determine the stability situation at this flight condition. The analyses were conducted with one structural mode present at a time, and the input structural mode frequency was dispersed ± 15 percent about its nominal values to account for uncertainties in the structural modeling. This variation was judged to be a reasonable estimate to cover the worst case conditions in terms of the proximity of the structural and propulsion system resonances (see Ref. 4). The damping ratio used for all structural modes was 0.01. The analyses were generally conducted using the Aerospace nominal values for the parameters appearing in the elementary pump models for the LPOTP and HPOTP; the exceptional case was the use of
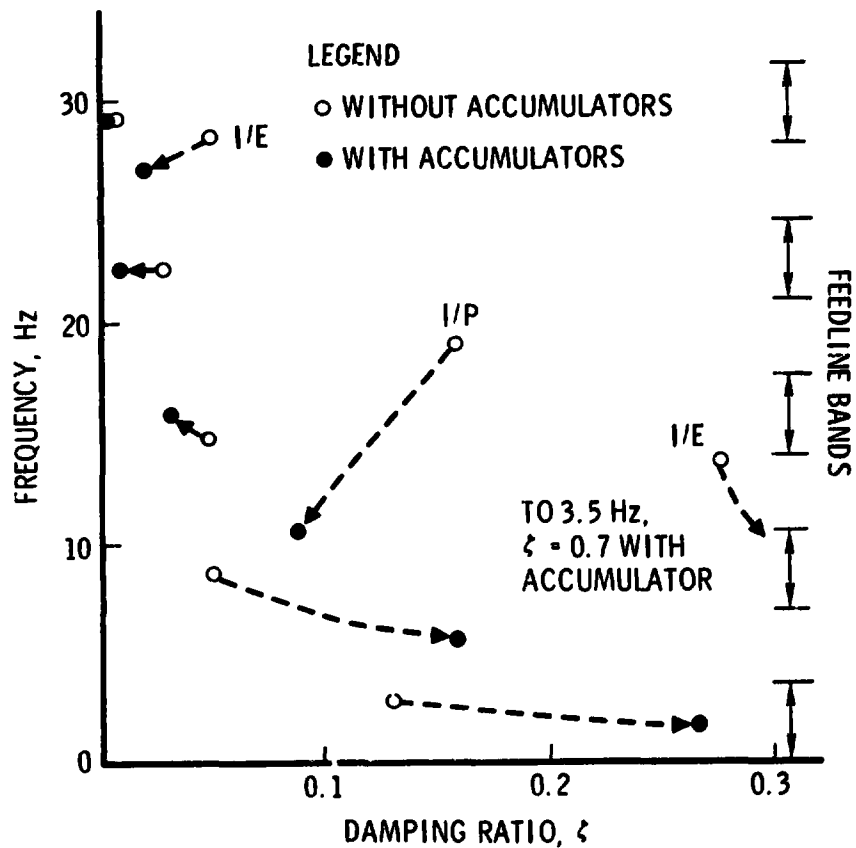
Figure 7. Frequencies and Damping Ratios of
Propulsion System Modes at Liftoff
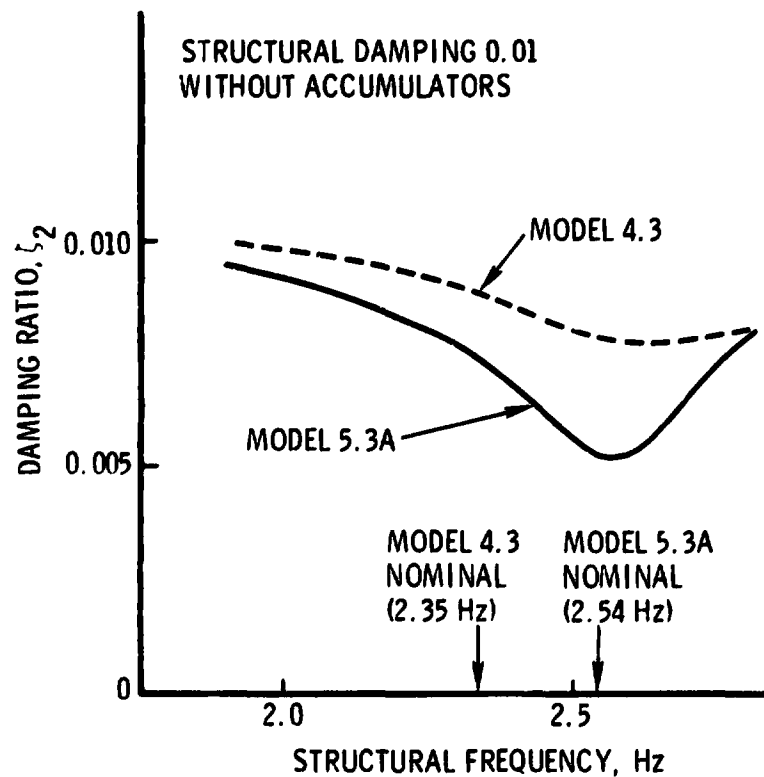
Figure 8. Effect of Modal Data on System
Damping

the Rockwell nominal values for the pump cavitation compliance in ' .·o)f
the sensitivity studies that were conducted with a "shifted" structural mode
frequency (see Section 1.4.6). The system without suppression and the
system with the baseline 0.017 m^3 (0.6 ft^3) gaseous oxygen (gox) accumu.. ɔ
were first treated. These nominal case analyses were then followed by a
series of sensitivity studies in which the effects of downcomer motion,
pump gain, accumulator volume, LPOTP resistance, structural mode fre-
quency shift, and accumulator failure were examined.

1.4.1   Nominal System: No Suppression

In the study of Ref. 4 the liftoff stability analys.:s undertaken with
the multi-engine model and the model 4.3 modal data indicated that the
nominal system was free of pogo instability. The present analysis, under-
taken with the model 5.3A set of modal data, indicated that the stability of
the system had been degraded relative to the previous results. Specifically,
it was found that

a.   The L2 mode at 2.54 Hz gave rise to a minimum damping
ratio of 0.0053, whereas the previous minimum damping
ratio was 0.0087.

b.   An instability was now predicted in a new local upper SSME
structural mode at 17.8 Hz (L54 mode).

The stability behavior in the L2 mode is illustrated in Figure 8
where the results obtained for both the 4.3 and 5.3A modal sets are pre-
sented. The destabi: .zing influence in this mode results from coupling be-
tween the structural mode and the fundamental mode of the propulsion system
(see Figure 5). The source of the degradation in system stability is the
change in structural mode shape. Specifically, the axial modal amplitude of
the downcomer is larger in the later modal data. Increase in modal ampli-
tude at this location was previously shown to reduce the stability of the L2
mode (Ref. 4).

The L54 modal amplitude distribution is illustrated in Figure 9.
The sensitivity of stability in this mode to structural mode frequency is
shown in Figure 10, where it is seen that a minimum damping ratio of -0.002
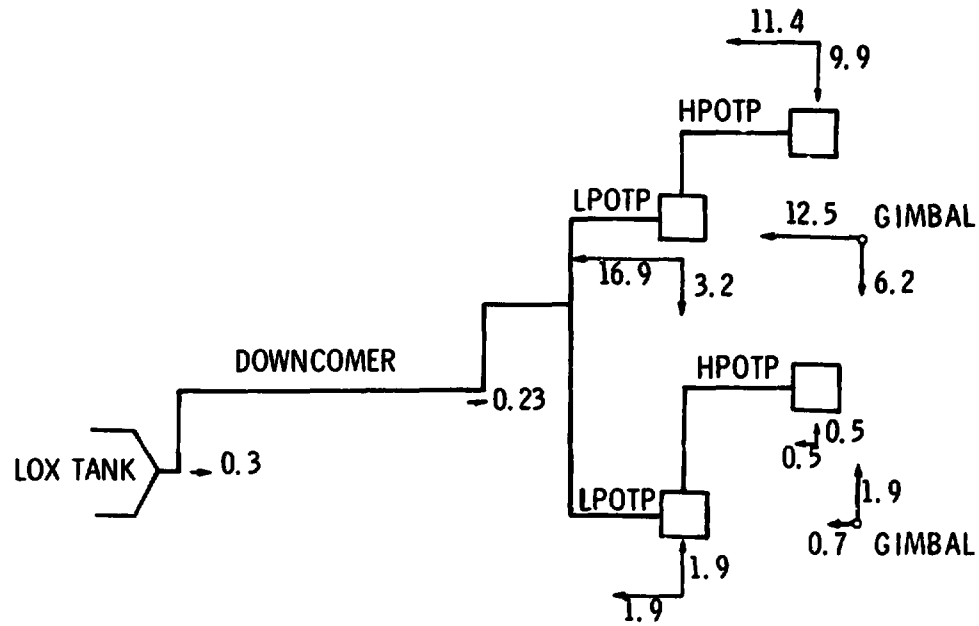
Note: Upper engine motion predominates.
Arrows not to scale.

Figure 9. Modal Amplitudes in L54 Mode
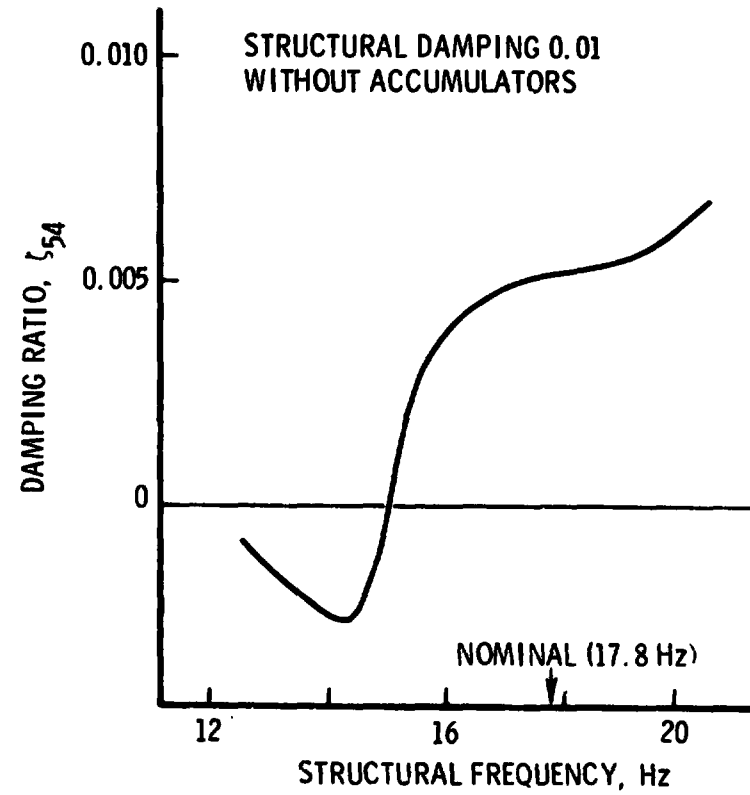
Figure 10. System Damping without
Accumulators: L54 Mode

is predicted at a structural frequency of about 14 Hz. Examination of the
eigensolution for this case reveals that the instability results from coupling
of the structural mode with the first inter-engine mode of the propulsion
system (Figure 5). Significant coupling takes place because of the similar
shape of the involved structural and propulsion system modes (compare
Figures 6 and 9).

1.4.2 Nominal System: Baseline Accumulator

The effect of the baseline 0.017 m^3 (0.6 ft^3) gox accumulator on the
frequencies of the propulsion system modes was discussed in Section 1.3. In
particular, it was seen from the spectra presented in Figure 5 that the fre-
quencies of the fundamental mode and of the first inter-engine mode were
decreased by some 40 and 75 percent, respectively. ˙ is not surprising then
that the stability in the L2 mode is enhanced (see Figure 11) and the instability
in the L54 mode eliminated (see Figure 12) by the presence of the accumula-
tor. One question which does arise, however, is whether the inter-engine
mode, which is now the second mode of the propulsion system (see Figure 5),
significantly couples with the lower structural modes. This question was
examined for the L2 mode and it was found that no significant destabilizing
coupling took place. The reason for the weak coupling is that the inter-
engine mode has fluid motion in the upper engine which is out of phase with
that in the lower engines, whereas the structural motion of the engines are
all in phase - consequently, a cancelling effect takes place. Examination of
the modal character of other low frequency structural modes indicated that
significant coupling with the inter-engine mode would be unlikely.

1.4.3 Downcomer Motion/Pump Gain Study

The stability of the L2 mode had previously been shown to be sensi-
tive to both the modal amplitude of the downcomer and pump gain (Ref. 4).
This sensitivity was checked with the present modal data with and without
accumulators. Analyses were run with a range of downcomer modal ampli-
tudes for unit pump gain, the Aerospace nominal, and the Aerospace maxi-
mum pump gains. The resulting minimum damping ratios, calculated over
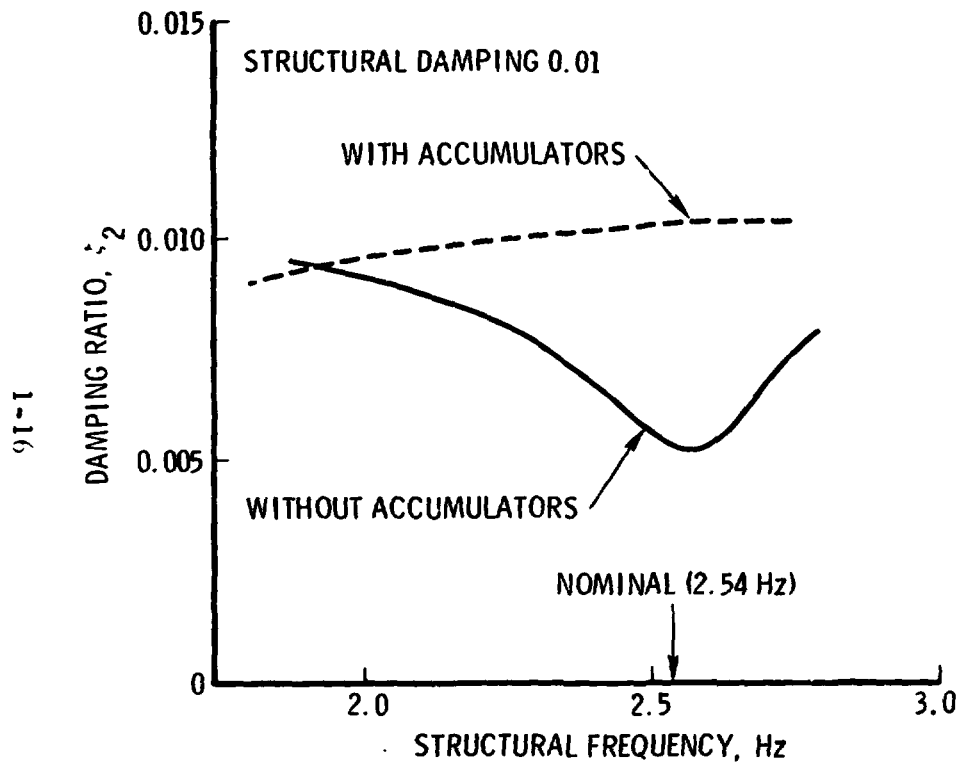
Figure 11. Effect of Accumulators on System Damping: L2 Mode
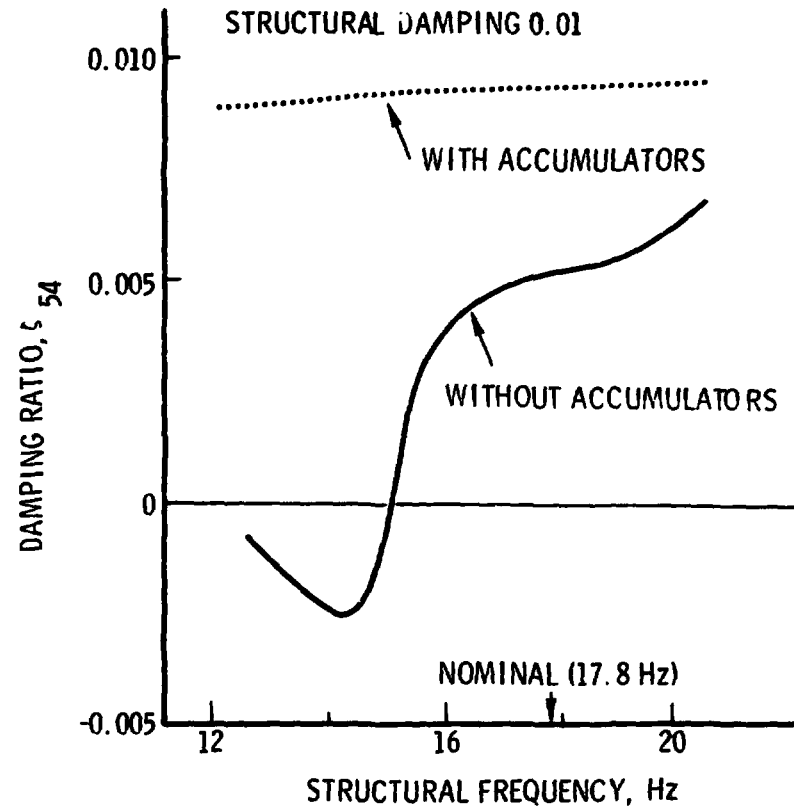
Figure 12. Effect of Accumulators on System Damping: L54 Mode

the specified frequency range (2.54 Hz ±15 percent), are shown in Figure 13 for the case of no accumulators. The damping levels are shown as a function of the ratio of the downcomer modal displacement $\varphi_x(3)$ to the average axial modal displacement of the SSME gimbals $\phi_{xa}(g)$. The results indicate that pump gain increase remains as a significant destabilizing influence, the effect tending to be more pronounced at the higher levels of downcomer motion. The character of the curves in Figure 13 reflects a balance between the destabilizing effect of engine thrust [increases with pump gains and with $\phi_x(3)/\phi_{xa}(g)$] and the stabilizing effect of the axial pressure-area force at the aft corner of the downcomer [increases with $\phi_x^2(3)/\phi_{xa}^2(g)$]. As $\phi_x(3)/\phi_{xa}(g)$ increases, the stabilizing effect eventually dominates. The result is the appearance of a minimum, as seen in the curves for unit and nominal pump gains. Such a minimum would also occur in the curve for maximum pump gains if the plot extended to large enough values of $\phi_x(3)/\phi_{xa}(g)$.

The sensitivity of the L2 mode stability to pump gains is further illustrated by the results shown in Figure 14. There the minimum damping ratios, for an arbitrarily selected worst case value of downcomer modal amplitude ratio of 0.75, are presented as a function of the pump gain product $(m_1+1)(m_2+1)$. Results are given for the system with and without accumulators. The extreme sensitivity of the damping level to pump gain in the absence of suppression is clearly shown; it is seen that a 50 percent increase of the pump gain product from unity to a value of 1.5 produces a 40 percent drop in the predicted damping level. The sensitivity is considerably reduced by the presence of the baseline accumulators. In this instance the damping ratio has only dropped to a value of about 0.007 for the maximum value of pump gain product (8.1) that was treated; in the corresponding case with no accumulators, the system has become unstable with a damping ratio of about -0.006.

1.4.4   Accumulator Volume

The sensitivity of the system stability to accumulator volume was also examined to establish a minimum required accumulator precharge at liftoff. This information was n support of studies of alternative charging

STRUCTURAL DAMPING 0 01
WITHOUT ACCUMULATORS

UNIT PUMP GAINS

MINIMUM DAMPING RATIO, ζ_2

0.010

NOMINAL PUMP GAINS

0

MAXIMUM PUMP GAINS

-0.010

NOMINAL (0.26)

0   0.5   1.0

$$\frac{\text{DOWNCOMER AXIAL AMPLITUDE}}{\text{AVERAGE AXIAL GIMBAL AMPLITUDE}} , \frac{\phi_x(3)}{\phi_{xa}(g)}$$
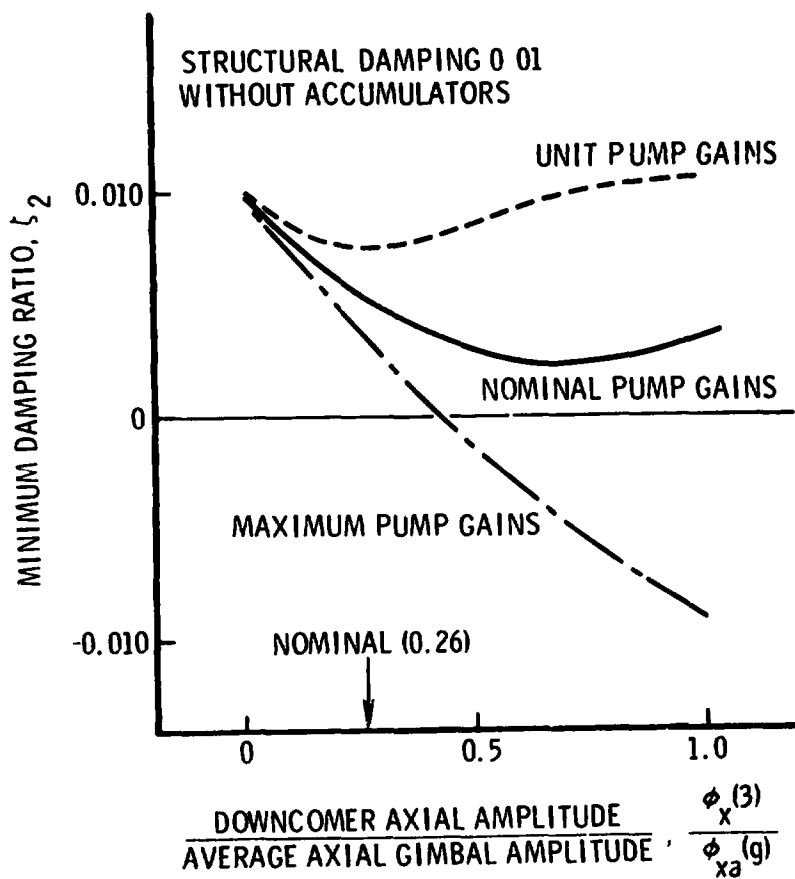
Figure 13. Minimum System Damping versus
Downcomer Motion for Different
Pump Gains: L2 Mode

STRUCTURAL DAMPING 0. 01
$\phi_x(3)/\phi_{xa}(g) = 0.75$

0.010

WITH ACCUMULATORS

MINIMUM DAMPING RATIO, ζ_2

0

WITHOUT ACCUMULATORS

-0.010

NOMINAL (2.4)   MAXIMUM (8.1)

1   5   10

PUMP GAIN PRODUCT $(m_1 + 1)(m_2 + 1)$
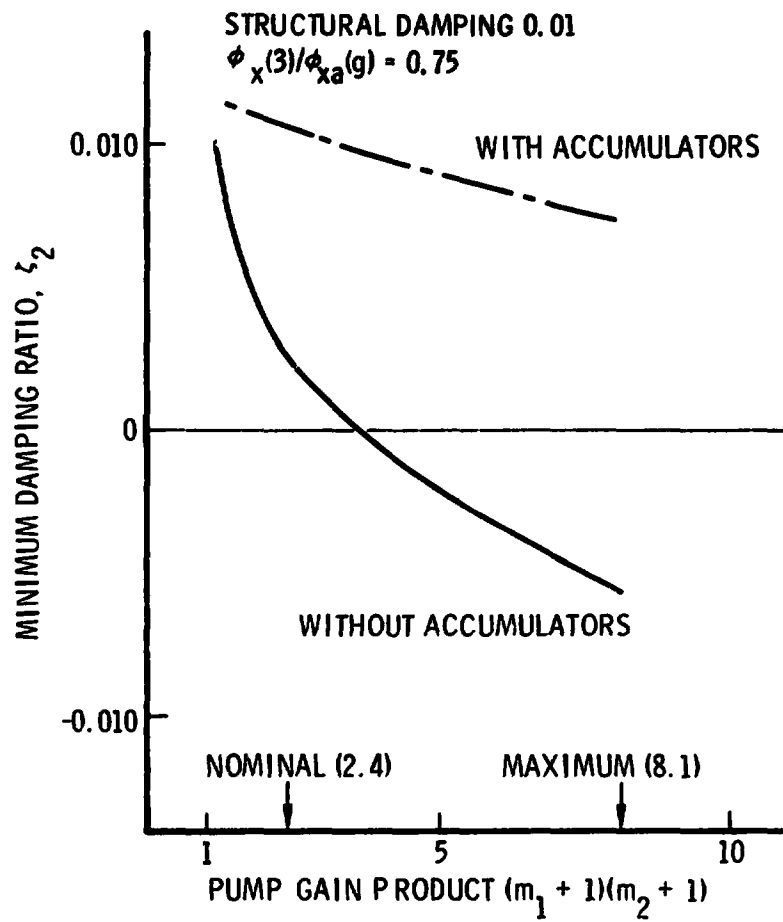
Figure 14. Minimum System Damping versus
Pump Gain Product: L2 Mode

procedures for the accumulators. The study was directed to the L2 mode since previous analyses had indicated that volume sensitivity was more pronounced in the lower frequency modes (Ref. 4). The results of a series of analyses for a downcomer amplitude ratio of 0.75 are presented in Figure 15; the minimum damping ratio is plotted against accumulator volume for unit and nominal pump gains. The latter case shows a much greater sensitivity to accumulator volume and is therefore used as a basis for the recommended minimum accumulator volume at liftoff. It is seen that stability is strongly enhanced as the accumulator volume is increased to about 0.014 m^3 (0.5 ft^3); a much lower rate of stability enhancement occurs for further increases in accumulator volume.

To establish a minimum accumulator compliance that should be available prior to liftoff, it was assumed that the accumulator was required to limit system stability loss to less than half of the structural damping. This was based upon the 6 dB damping gain margin recommended for nominal system parameters in Ref. 5. Thus, a system damping ratio of greater than 0.005 is required for an assumed structural damping ratio of 0.01. The results in Figure 15 (for nominal pump gains) show that an accumulator compliance equivalent to that provided by a gox volume of 0.007 m^3 (0.25 ft^3) is the minimum required prior to liftoff.

1.4.5 LPOTP Resistance

A study was directed at the sensitivity of the L54 mode stability to variation of the resistance of the LPOTP. Previous analysis had indicated that the L2 mode stability was insensitive to such variation. The incentives for this particular study were twofold. First, on a physical basis it was anticipated that the damping in the inter-engine mode of the propulsion system would be sensitive to LPOTP resistance. Second, the experimental results developed by Caltech for the LPOTP impeller (discussed in Section 2.1.1) suggested that the resistive impedance decreased dramatically at high frequencies of oscillation. The results of an analysis undertaken for the case of zero LPOTP resistance revealed that loss of this resistance significantly degraded the stability of the system. Results are shown in Figure 16

STRUCTURAL DAMPING 0.01

$\phi_x(3)/\phi_{xa}(g) = 0.75$

MINIMUM DAMPING RATIO, ζ_2

0.010

UNIT PUMP GAINS

NOMINAL PUMP GAINS

0.005

0

0   0.5   1.0   1.5   2.0

FT^3

0   0.02   0.04

ACCUMULATOR VOLUME, m^3
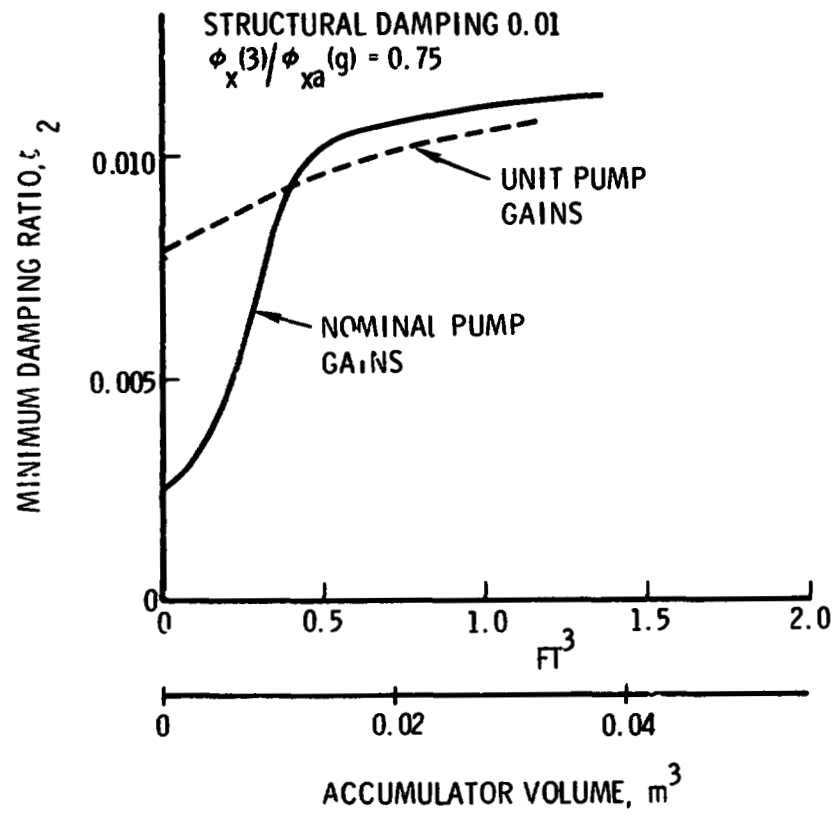
Figure 15.   Effect of Accumulator Volume on Minimum System Damping: L2 Mode

0.02

STRUCTURAL DAMPING 0.01

WITH ACCUMULATORS (ZERO RESISTANCE)

DAMPING RATIO, ζ_{54}

0.01

WITHOUT ACCUMULATORS

0

NOMINAL RESISTANCE

ZERO RESISTANCE

NOMINAL (17.8 Hz)

-0.01

12   16   20

STRUCTURAL FREQUENCY, Hz
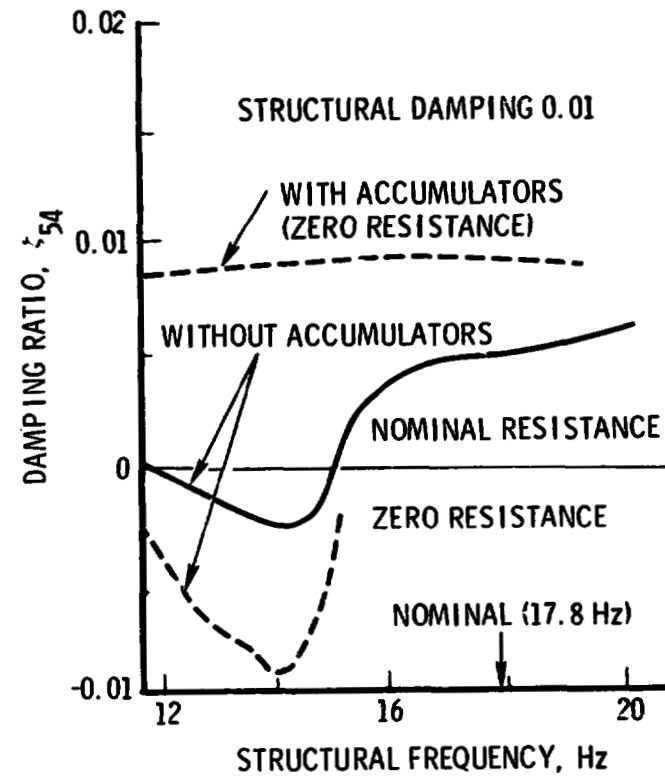
Figure 16.   Effect of LPOTP Resistance on System Damping: L54 Mode

for the system without accumulators for zero LPOTP resistance and for the nominal resistance of 8.8 MNs/m^5 (0.53 sec/in.^{2}). It is seen that the lowest predicted damping level has dropped from -0.0025 to -0.0095. Fortunately, the frequency shift effect provided by the baseline accumulator is sufficient to desensitize the stability to LPOTP resistance. This is illustrated in Figure 16 where the results obtained with the baseline accumulator and zero pump resistance are also presented. These results are quite close to those obtained for the nominal LPOTP resistance.

1.4.6 L54 Mode Frequency Shift

Subsequent to the performance of the stability analyses with the model 5.3A modal data, some preliminary results from the horizontal ground vibration test (HGVT) that had been performed on Orbiter Vehicle 101 became available (Ref. 12). These results indicated that a local upper-engine mode occurred at about 30 Hz, rather than at 18 Hz as predicted in the modal analysis. Lacking mode shape data for this 30-Hz mode, it was decided to examine the effect of the new frequency by simply shifting the frequency of the L54 mode (a local upper-engine mode) to the 25-32 Hz range. From the frequency spectra shown in Figure 5, it is seen that such a shift could bring this structural mode into proximity with the second inter-engine mode of the propulsion system with or without the accumulators present. For conservatism, the LPOTP resistance was set to zero. The results of analyses undertaken for the system both without accumulators and with the baseline accumulators are shown in Figure 17. In the absence of accumulators it is seen that there are no strong destabilizing tendencies. In fact, the opposite is true in the 27-29 Hz range where the system damping is significantly enhanced from the prescribed 0.01 structural damping ratio. Examination of the generalized force components indicates that this enhancement is primarily due to the engine thrust forces. When the accumulators are introduced the thrust forces, and hence their stabilizing influence, are reduced. This effect is seen in the relationship of the stability curves for the case with and without accumulators in Figure 17. A similar effect was observed in previous studies (Ref. 4, Section 2.3.2.2, Figure 27).
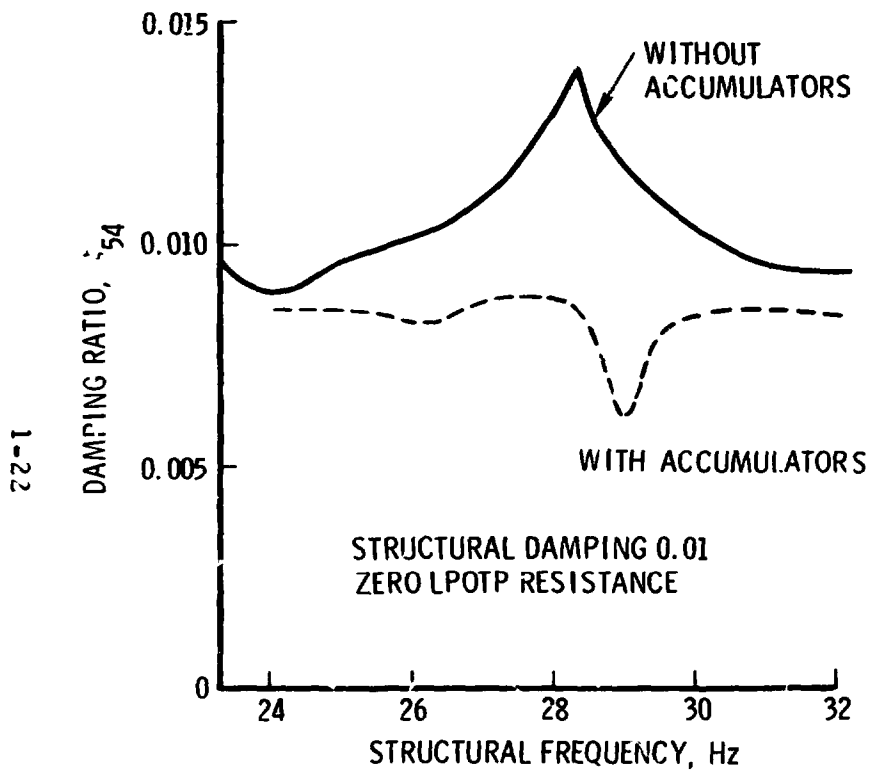
Figure 17. Stability of L54 Mode Shifted to Higher Frequency
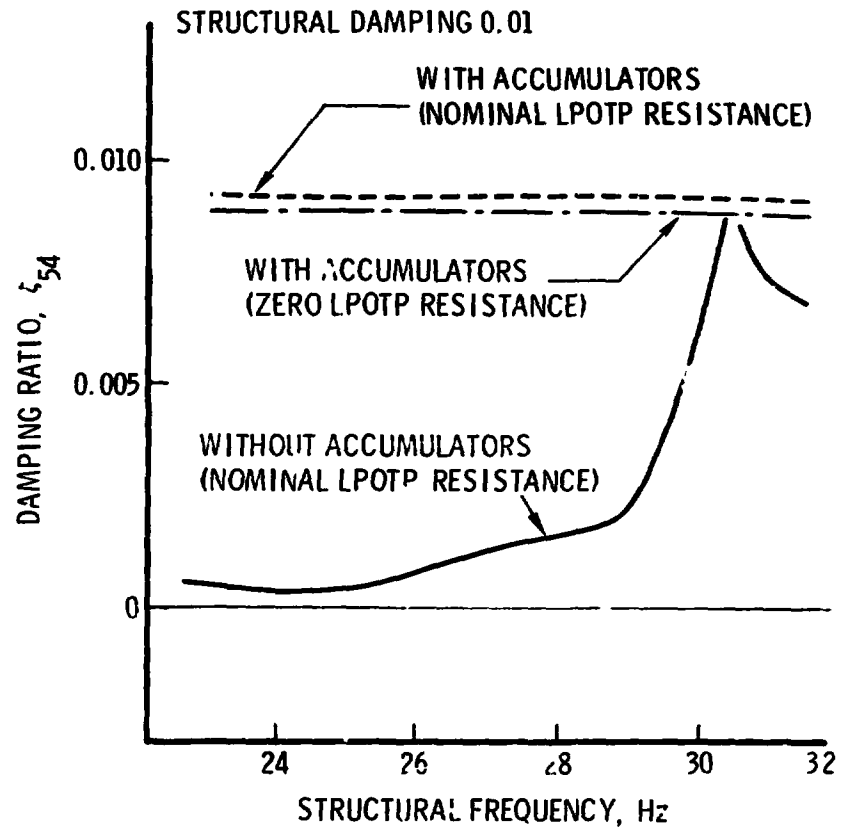
Figure 18. Stability of L54 Mode Shifted to Higher Frequency: Rockwell Nominal Pump Compliances

It was also of interest to see what happened if the first inter-engine mode frequency was shifted to this higher range. Such a shift could be achieved by replacing the Aerospace nominal pump cavitation compliance values of 0.0012 m^5/MN (0.02 in.^{2}) for the LPOTP and 0.00027 m^5/MN (0.0045 in.^{2}) for the HPOTP with the corresponding Rockwell nominal values of 0.39×10^{-3} m^5/MN (0.0067 in.^{2}) for the LPOTP and 0.59×10^{-4} m^5/MN (0.001 in.^{2}) for the HPOTP. The pump gains were not changed. Stability analyses undertaken for these conditions and no accumulators revealed that significant destabilizing coupling occurred between the L54 mode and the first inter-engine mode at these higher frequencies. These results are shown in Figure 18 where it is seen that the system is only marginally stable. It was this same type of interaction which had induced instability with the unshifted L54 mode and the Aerospace pump compliances (see Figure 10). The results obtained when the baseline accumulators are added to the system are also shown in Figure 18 for the cases of nominal and zero LPOTP resistance. It is seen that the addition of the accumulators restores the system stability and is insensitive to reduced LPOTP resistance.

1.4.7   Accumulator Failure

A limited study was undertaken to examine the sensitivity of the system stability to isolated accumulator failures. The objective of the study was to obtain an indication of the criticality of such failures. With the available pitch-plane model it was possible to analyze the following two failure conditions:

a.   Failure of both accumulators on the two lower engines
b.   Failure of the accumulator on the upper engine

Both of these cases were treated. The analyses were carried out with the L2 and the shifted L54 modes; stability calculations were limited to nominal pump gains and downcomer structural mode amplitudes. In the case of the L2 mode it was found that loss of the accumulator on the upper engine had negligible effect on the system stability, and loss of the accumulators on the two lower engines resulted in a reasonably small loss in the stability level. These effects are illustrated in Figure 19 where the system damping for the
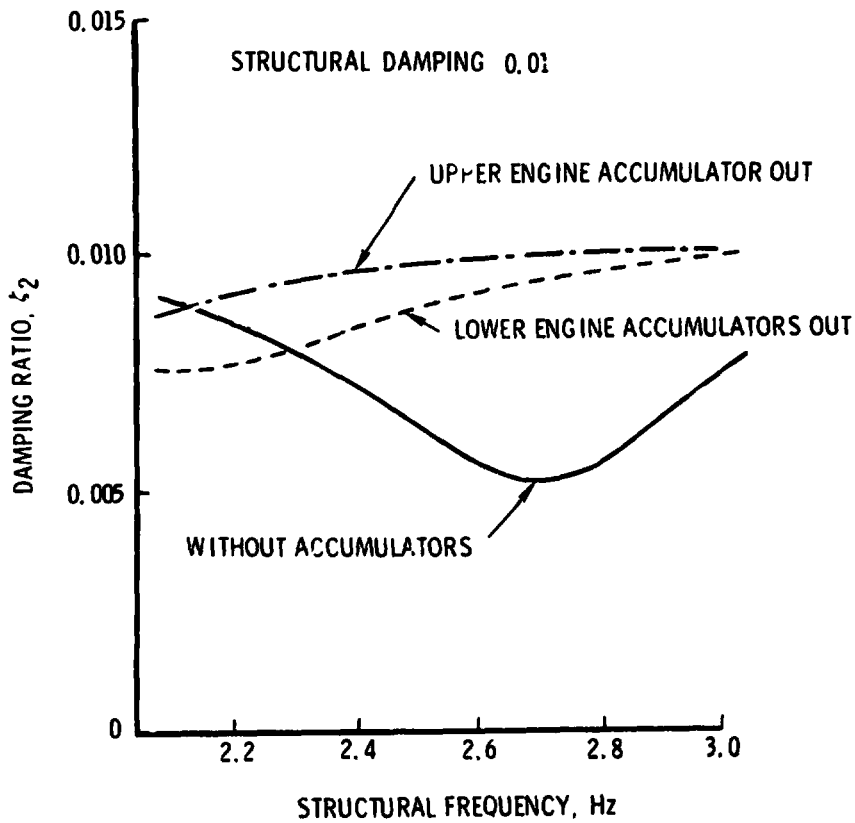
Figure 19. Stability of L2 Mode for Various Accumulator Conditions
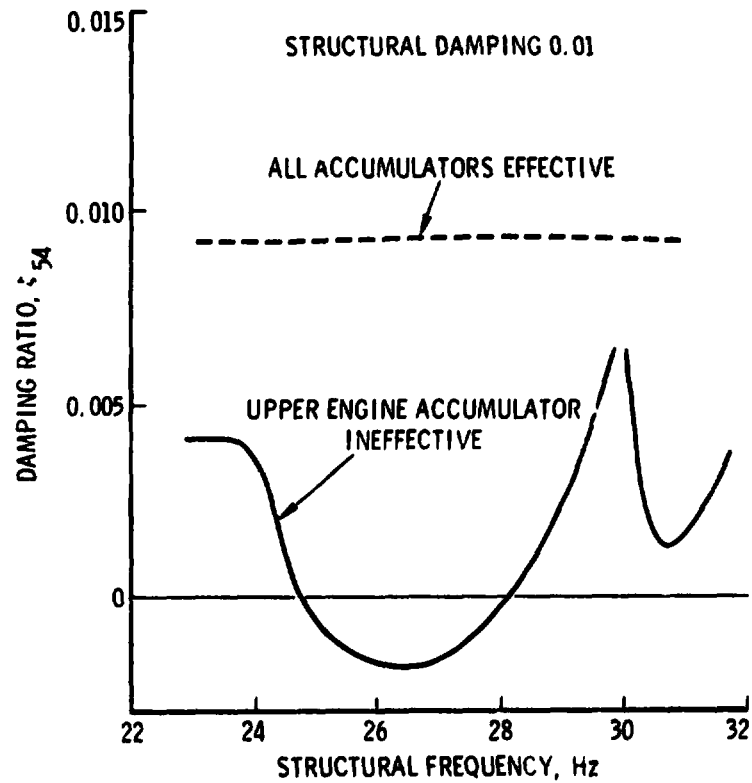
Figure 20. Stability of L54 Mode Shifted to Higher Frequency with Upper Engine Accumulator Ineffective: Rockwell Nominal Pump Compliances

two failure conditions are presented together with the results for all the accumulators effective.

In view of the results of the ground vibration test on Orbiter Vehicle 101 (see discussion in Section 1.4.6), the analyses for the L54 mode were undertaken at the higher structural mode frequencies (25 ~ 32 Hz). To construct a critical stability case the Rockwell nominal pump compliances were employed to bring the first inter-engine mode of the propulsion system (without accumulators) into this frequency range. Since the upper engine has the predominant motion in the L54 structural mode it was not surprising to find that loss of the accumulators on the two lower engines did not produce any significant degradation of the system stability, whereas loss of the upper engine accumulator precipitated an instability (see Figure 20). The propulsion system mode involved in this instability had a strong inter-engine mode character.

The above results should not be construed to imply that the accumulators on the two lower engines are unnecessary. Clearly, the absence of these accumulators can be expected to yield a much greater stability loss in the L2 mode for conditions of larger downcomer motion and higher pump gains (see Figures 13 and 14). In addition, the role of these accumulators may be significant in maintaining stability for coupling between inter-engine propulsion modes in the yaw plane and local engine structural modes involving one or both lower engines. Study of this latter possibility will be undertaken when a three-dimensional model of the MPS and vehicle structure is available.

1.5   SUMMARY

The stability analyses undertaken for the liftoff event with the model 5.3A structural modal data set revealed the following for the system without accumulators:

a.   Degradation of the L2 structural mode (2.54 Hz) stability relative to the previous predictions made with the Shuttle model 4.3 modal data (see Figure 8)

b. The presence of an instability in the L54 local upper-engine structural mode (17.8 Hz) due to coupling with the first inter-engine mode of the propulsion system (see Figure 10)

c. Sensitivity of the L2 mode stability to variations in pump gains and in downcomer amplitude (see Figures 13 and 14)

d. Aggravation of the instability in the L54 mode with decreased resistance of the LPOTP (see Figure 16)

With the addition of the baseline 0.017 m^3 (0.6 ft^3) gox accumulators, it was found that satisfactory stability existed in all situations investigated. Specifically

a. The stability of the L2 mode was restored to a satisfactory level (see Figure 11).

b. The instability of the L54 mode was eliminated and the damping in this mode restored to a satisfactory level (see Figure 12).

c. Th ~ sitivity of the L2 mode stability to variations in r in and in downcomer amplitude was greatly reduced (ure 14).

d. Th ɔ ility of the L54 mode was insensitive to decreased resista ce of the LPOTP (see Figure 16).

Based upon the location of a 30-Hz local upper-engine structural mode in the orbiter ground vibration tests, sensitivity studies were undertaken with the L54 mode shifted to about 30 Hz. The results indicated marginal stability conditions for the system without accumulators if the first inter-engine mode frequency was also in this frequency range. However, addition of the baseline accumulators again restored the stability to a satisfactory level even in the absence of LPOTP resistance.

In support of accumulator charging studies by NASA and Rockwell, an analysis was conducted of the variation of L2 mode stability with accumulator volume. It was found that an accumulator compliance equivalent to a gox volume in excess of 0.007 m^3 (0.25 ft^3) was required at liftoff to avoid a 50 percent loss in system damping for the assumed structural damping ratio of 0.01.

The effect of failure of the accumulator on the upper engine or both accumulators on the lower engines was examined for the L2 and L54 modes. It was found that such failures had relatively little impact on the stability of the L2 mode for nominal pump gains and downcomer amplitude. Any accumulator failure, however, is expected to lead to significant L2 mode stability loss for higher pump gains and downcomer motion (see Figure 19). Failure of the upper-engine accumulator precipitated an instability in the L54 mode (see Figure 20) with the Rockwell nominal pump compliance values.

Finally, it should be noted that the present analyses did not involve the separation mode of the propulsion system (see Section 1.3). Previous investigations (Refs. 4 and 7) have demonstrated the benefit of accumulator resistance in the elimination of an instability associated with this particular fluid mode. The matter of accumulator resistance will again be addressed in the next phase of our pogo studies.

2. APPLICATION OF QUARTER-SCALE LPOTP TRANSFER FUNCTIONS

Pump dynamics play a very important role in pogo stability analysis. The pump model employed in previous studies (Refs. 1 through 4) does represent the existing state of the art (Ref. 5). However, the validity of this model is questionable because it was not based upon detailed pump experimental data. A beginning of the process for refining the pump model is described in this section using the pump dynamic transfer functions determined experimentally at the California Institute of Technology (Caltech) for a quarter-scale model of the LPOTP impeller (Ref. 6).

2.1   CALTECH EXPERIMENTAL PROGRAM

An experimental program for the dynamic response of cavitating turbomachines has been under way at Caltech, under contract from the NASA Marshall Space Flight Center (Ref. 6). In this study, elements of the linearized four-terminal transfer matrix of a quarter-scale LPOTP impeller have been measured at a number of operating conditions using water as the working fluid. Tabulated results were made available to us by Caltech, including some results not published in Ref. 6. The study reported here employs four sets of transfer matrix results, each corresponding to a particular value of the pump cavitation number σ_p (specifically, σ_p = 0.513, 0.114, 0.046, 0.024), all for a flow coefficient of 0.07 at 9000 rpm.

A schematic drawing of the Caltech pump test facility is shown in Figure 21. The pump, driven by an electric motor, is located at the lower left. An upstream smoothing section, containing the upstream pressure transducer, precedes the upstream flow measurement by a laser doppler velocimeter. Likewise, a downstream smoothing section, containing the downstream pressure transducer, precedes the downstream flow measurement. Also, an accelerometer is employed to measure the pipe motion in the direction of flow for each flow measurement. This enables the absolute flow measurement by the laser to be converted to relative flow for the transfer
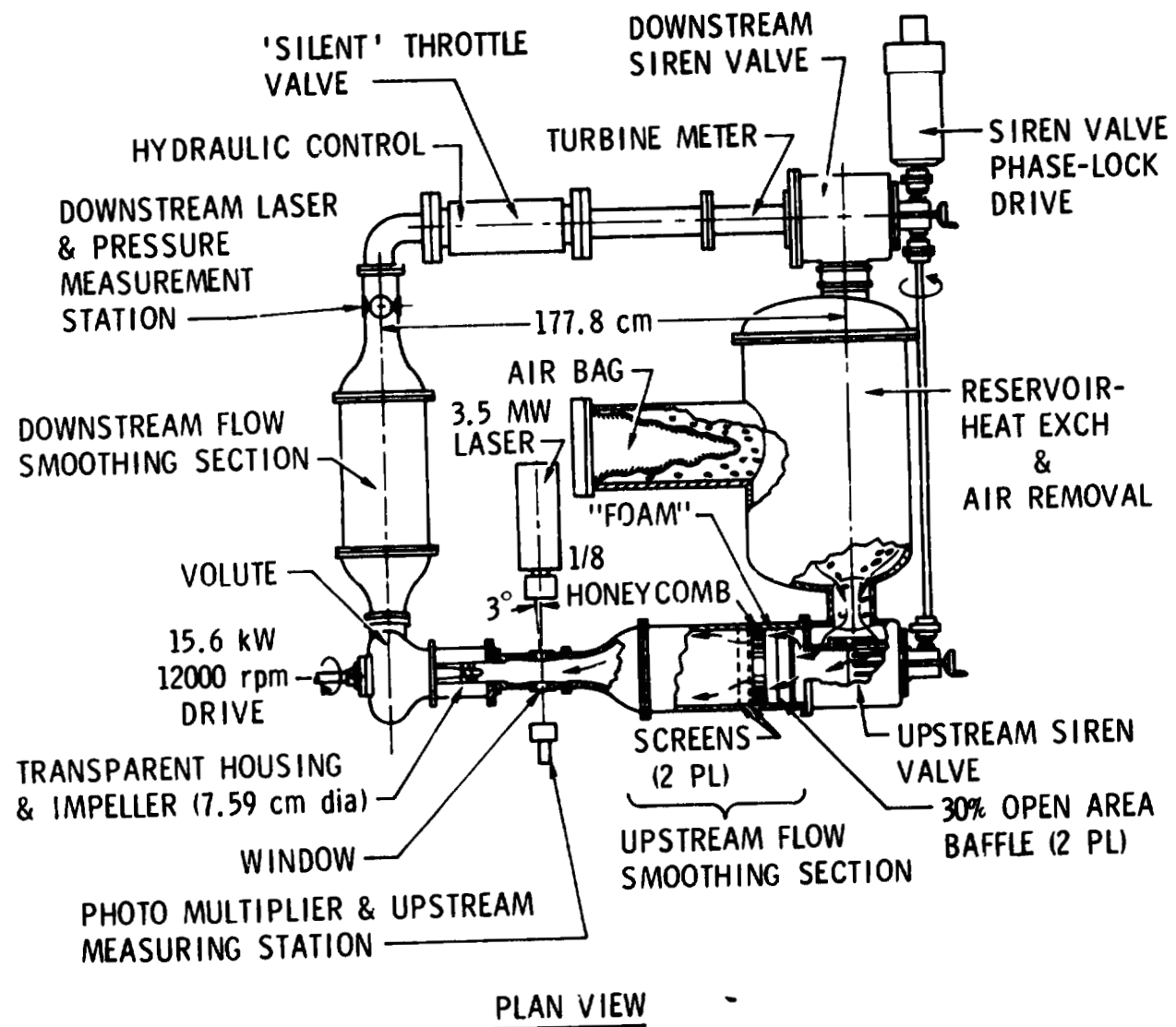
Figure 21. Schematic Drawing of Dynamic Pump Test Facility (from Reference 6)

matrix determination. Upstream and downstream, siren-type valves are employed to create periodic flow disturbances, with their individual amplitude and their relative phase adjustable to achieve various independent states of excitation. Other details of the setup are described in Ref. 6.

For each steady operating condition of the pump (rotating speed, flow coefficient, cavitation number), and for each of seven discrete frequencies of excitation, data is collected at three or more independent states of excitation for the transfer matrix determinations at those frequencies. The data consist of pressure, absolute flow, and line acceleration at upstream and downstream positions relative to the pump. By a least-square fit procedure described in Appendix D of Ref. 6, the real and imaginary parts of the four elements of the following transfer matrix are determined:

$$
\left\{
\begin{array}{c}
\underline{P}_d(\underline{\omega}) \\
\\
\underline{\dot{m}}_d(\underline{\omega})
\end{array}
\right\}
=
\left[
\begin{array}{cc}
1+\underline{Z}_{11}(\underline{\omega}) & \underline{Z}_{12}(\underline{\omega}) \\
\\
\underline{Z}_{21}(\underline{\omega}) & 1+\underline{Z}_{22}(\underline{\omega})
\end{array}
\right]
\left\{
\begin{array}{c}
\underline{P}_u(\underline{\omega}) \\
\\
\underline{\dot{m}}_u(\underline{\omega})
\end{array}
\right\}
\tag{4}
$$

where

$\underline{P}$ = a dimensionless sinusoidal pressure

$\underline{\dot{m}}$ = a dimensionless sinusoidal relative mass flow

u = upstream

d = downstream

$\underline{\omega}$ = the dimensionless frequency

The dimensionless quantities are defined by

$$
\underline{P} = P\Big/\frac{1}{2}\rho U_{tip}^2
$$

$$
\underline{\dot{m}} = Q\Big/A_i U_{tip} \tag{5}
$$

$$
\underline{\omega} = \omega H\Big/U_{tip}
$$

2-7

where

P = physical pressure

Q = volumetric flow

ρ = fluid density

U_{tip} = tip speed of the pump inducer

A_i = inlet flow area

ω = physical frequency

H = tip spacing of the inducer

Studies were initiated for two possible methods of using the experimental results to describe the LPOTP for stability analysis. The first method consists of obtaining fitted polynomials (in the complex frequency, s) to the measured transfer functions. The second method consists of obtaining a lumped parameter, physically based model which reflects the experimental results. In both cases the data are employed in dimensionless form. Conversion of the dimensionless parameters to dimensional ones is defined in Table 2.

2.2 CURVE FITTED TRANSFER FUNCTIONS

This section describes the first attempt to employ the quarter-scale LPOTP results for stability analysis. The approach consisted of obtaining analytical fits of the measured transfer functions and using the resulting expressions to describe the LPOTP in the stability analysis equations. Two fitting approaches were tried: (1) global polynomial fits valid for the entire frequency range and (2) piecewise linear fits valid over a limited frequency range. These direct analytical fitting approaches had the advantage of enabling a relatively rapid incorporation of the experimental data into the analysis. It was, however, somewhat crude and, when implemented, was judged to be of questionable validity. Nevertheless, the approach is outlined and the concerns are identified as background for possible future studies.

Table 2. Conversion Factors to Obtain Dimensional
Quantities for Pump Modeling

Dimensionless Quantity	Multiply by Factor Below to Obtain Dimensional Quantity[*]	
	SI Units	Engineering Units
Frequency, $\underline{\omega}$	$U_{tip}/2\pi H = 96.15$ Hz	(same)
Resistance, $\underline{R}$	$\rho U_{tip}/2A_i = 4.33$ MN s/m^5	$U_{tip}/2gA_i = 0.285$ sec/in.^{2}
Inertance, $\underline{L}$	$\rho H/2A_i = 7.16\times10^{-3}$ MN s^{2}m^5	$H/2gA_i = 4.73\times10^{-4}$ sec^2/in.^{2}
Compliance, $\underline{C}$	$2HA_i/\rho U_{tip}^2 = 0.0924$ m^5/MN	$2gHA_i/U_{tip}^2 = 5.80\times10^{-3}$ in.^{2}

[*]Conversions based upon

U_{tip} = 35.9 m/s (117.8 ft/sec)

A_i = 41.4 cm^2 (6.41 in.^{2})

H = 5.94 cm (2.34 in.)

ρ = 998 kg/m^3 (ρg = 0.0361 lb/in.^{3}) for water at 21°C (70°F)

g = 9.81 m/s^2 (386 in./sec^2)

2.2.1 Experimental Transfer Functions and Global Polynomial Fits

The experimental transfer functions defined by Eq. (4) were adjusted by Caltech to remove the contribution of the facility portions between the measuring stations and the pump itself. To distinguish these transfer functions from the nonadjusted ones, we use the subscript p on the Z's to denote pump:

$$
\begin{Bmatrix} \underline{P}_d(\underline{\omega}) \\ \\ \underline{\dot{m}}_d(\underline{\omega}) \end{Bmatrix} = \begin{bmatrix} 1+\underline{Z}_{p11}(\underline{\omega}) & \underline{Z}_{p12}(\underline{\omega}) \\ \\ \underline{Z}_{p21}(\underline{\omega}) & 1+\underline{Z}_{p22}(\underline{\omega}) \end{bmatrix} \begin{Bmatrix} \underline{P}_u(\underline{\omega}) \\ \\ \underline{\dot{m}}_u(\underline{\omega}) \end{Bmatrix}
\tag{6}
$$

For our purposes the form was altered to obtain a correspondence with the form of the elementary model described by Eq. (1). Namely

$$
P_d = \left[1 + \underline{Z}_{p11} - \frac{\underline{Z}_{p21}\underline{Z}_{p12}}{(1+\underline{Z}_{p22})} \right] P_u - \frac{1}{\epsilon} \left[\frac{-\underline{Z}_{p12}}{1+\underline{Z}_{p22}} \right] Q_d
\tag{7}
$$

$$
Q_d = (1+\underline{Z}_{p22}) Q_u + \epsilon \underline{Z}_{p21} P_u
$$

where

$$
\bullet = 2A_1 / \rho U_{tip}
$$

Note that the pressures and flows are now in dimensional form.

The variations with frequency of the transfer function combinations appearing in Eq. (7) are shown in Figures 22 through 28 for the case of a cavitation number σ_p equal to 0.114 (a representative value for flight conditions). The figures show the experimental data points, a global polynomial fit of the data points, and, where applicable, the corresponding variation

from the elementary pump model used in past analyses. The global polynomial fits are for $s = i\omega$ and have the form

$$\text{Real part} = \sum_{j=0}^{n} c_j\, s^j \qquad (j\ \text{even})$$

$$\text{Imaginary part} = \sum_{j=1}^{n} c_j\, s^j \qquad (j\ \text{odd})$$

(8)

The value of n employed is stated in each case to define the level of the least squares fit.

Figures 22 and 23 show the real and imaginary parts of the transfer function Z_{p22}; the dashed line in the figure represents the data fit to the order of n given on each figure. This transfer function has been referred to as a "mass flow gain factor" (Ref. 13), and there is no equivalent term in the elementary pump model (i.e., $Z_{p22} \to 0$). Figures 24 and 25 show the real and imaginary parts of the function Z_{p21}; the dashed line in Figure 24 represents an n = 2 fit of the real part data, the dashed line in Figure 25 represents an n = 1 fit of the imaginary part data. Figure 25 also contains the variation of the corresponding term in the elementary model ($\epsilon \angle_{p21} \to sC_{p1}$) for the previously employed value of compliance for this cavitation number. The figure shows that the elementary model exhibits the same general trend as the experimental data. However, comparison shows that the value of cavitation compliance employed for the elementary model was considerably greater than that exhibited by the experimental data. This comparison could be influenced by several unknown factors so no conclusion is drawn. First, it has been shown theoretically that what has been called cavitation compliance for the elementary model includes a contribution of the mass flow gain factor (Ref. 13). On this basis the qualitative relationship seen in Figure 25 is to be expected. Other unknowns are the effect of lox versus water for the working fluid and the effect of dimensional scaling.
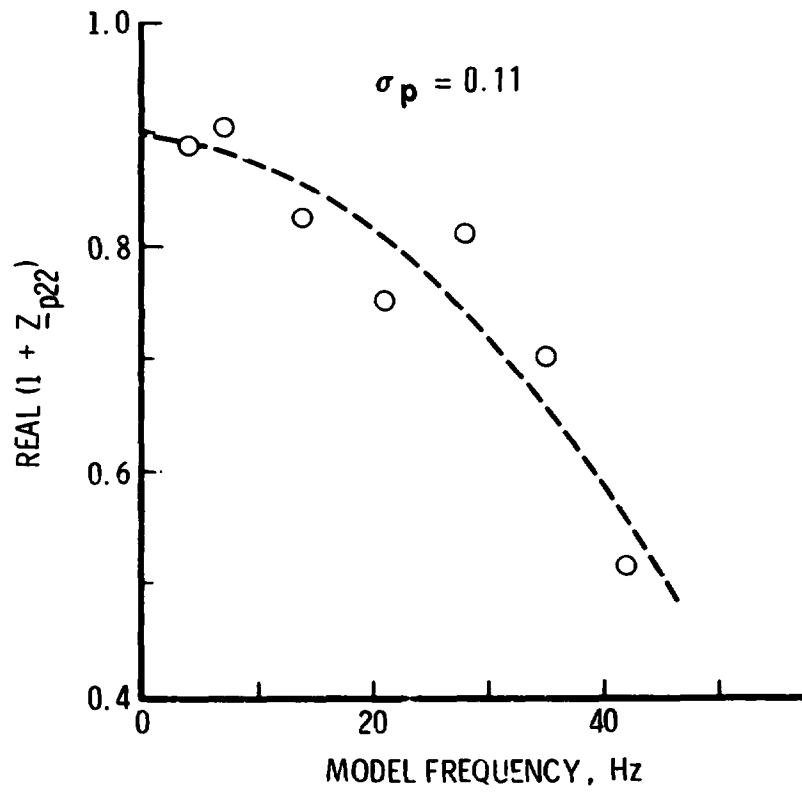
Figure 22. Polynomial Fit (n = 2) of Real $(1 + \underline{Z}_{p22})$
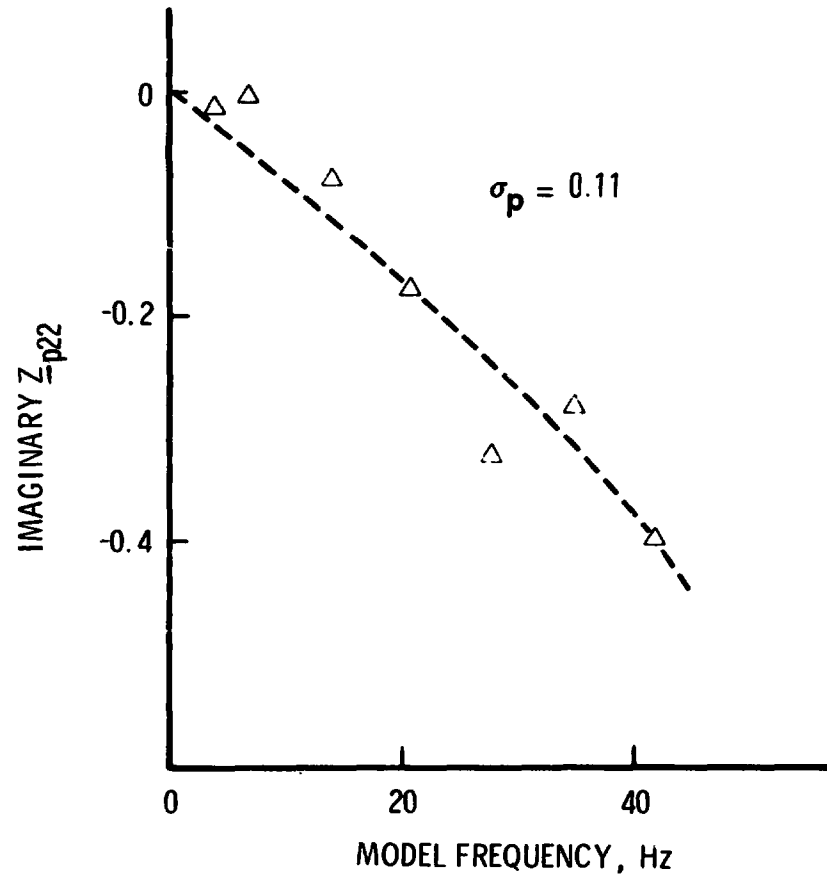
Figure 23. Polynomial Fit (n = 3) of Imaginary $\underline{Z}_{p22}$

$\sigma_p = 0.11$

$\sigma_p = 0.11$

ELEMENTARY MODEL

REAL $\underline{Z}_{p21}$

IMAGINARY $\underline{Z}_{p21}$

MODEL FREQUENCY, Hz

MODEL FREQUENCY, Hz
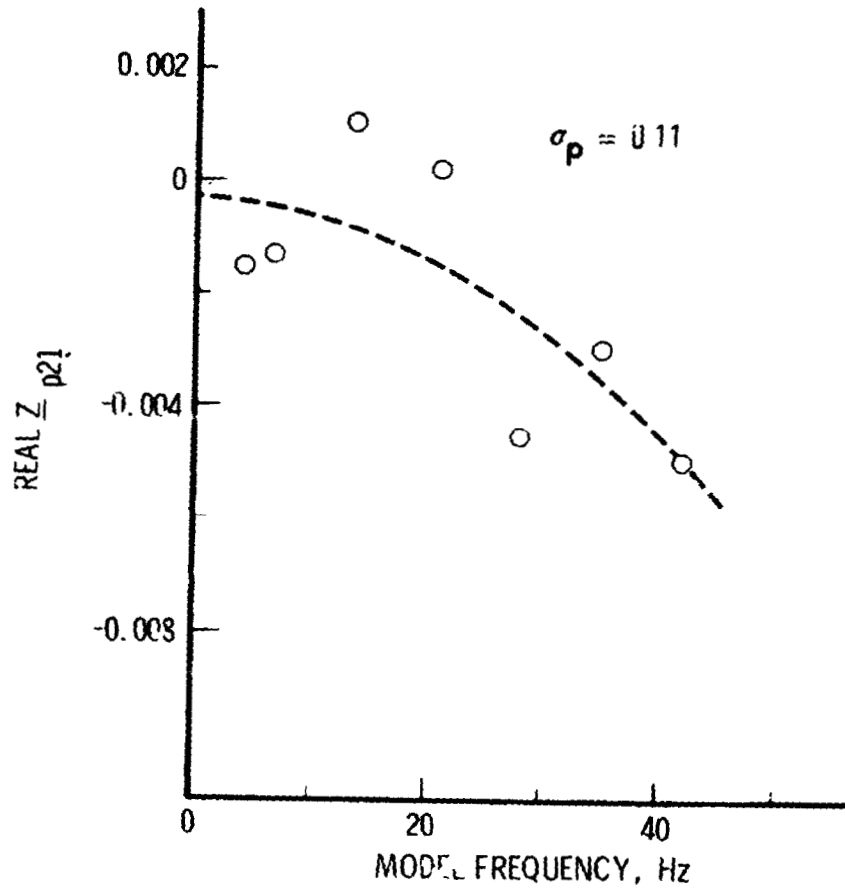
Figure 24. Polynomial Fit (n = 2) of Real $\underline{Z}_{p21}$
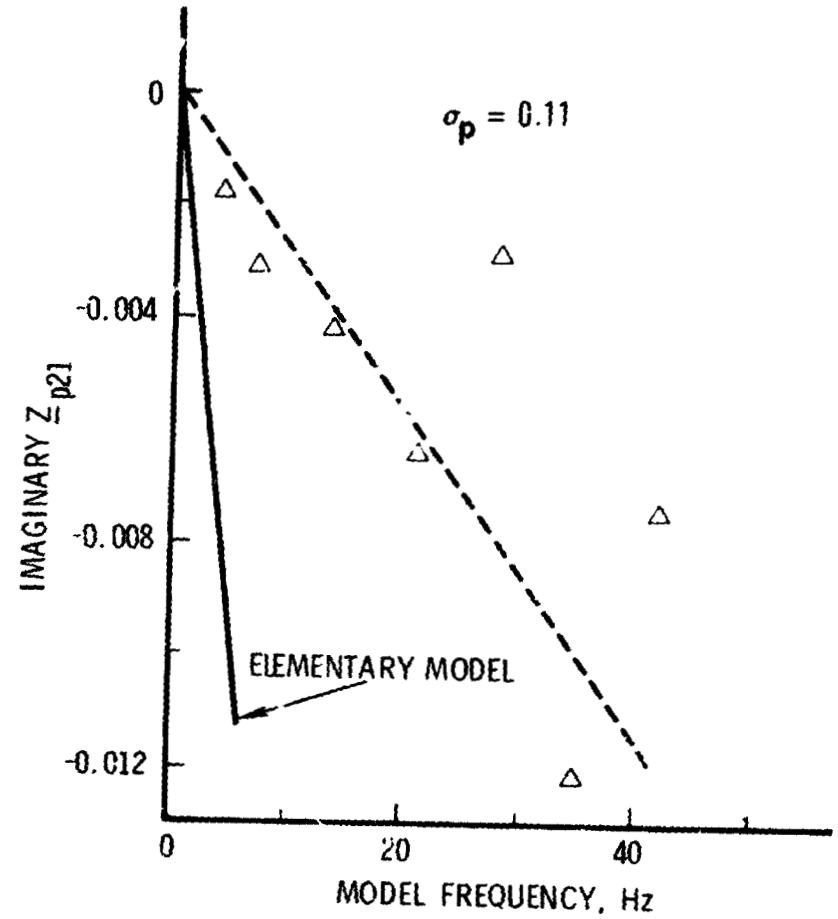
Figure 25. Linear Fit (n = 1) of Imaginary $\underline{Z}_{p21}$

Figures 26 and 27 show the real and imaginary parts of $Z_{p12}/(1+Z_{p22})$; an n = 6 fit of the real part data is shown in Figure 26; an n = 1 fit of the imaginary part data is shown in Figure 27. The variation of the corresponding terms employed for the elementary model is also shown. In the case of the real part, the elementary model term is simply the negative of the pump resistance; and in the case of the imaginary part, the term is the negative of the product of frequency and the pump inertance. On Figure 26 it is seen that the constant pump resistance employed for the elementary model does not reflect the frequency dependence apparent in the experimental data. The most dramatic aspect of this dependence is the rapid decrease of the real part at the higher frequencies. As was noted earlier (Section 1.4.5), this behavior led to the performance of some stability analyses (for a high-frequency structural mode) with an assumed LPOTP resistance of zero. The indication from Figure 27 is that the inertance associated with the experimental data is considerably larger than the value employed for the elementary model.

Finally, Figure 28 illustrates both the real and imaginary parts of the function $1 + Z_{p11} - Z_{p21}Z_{p12}/(1+Z_{p22})$. The equivalent elementary pump model term is the gain pump $m + 1$, which should be compared to the real part data. For this particular test condition, the data indicates a pump gain of about 0.9. Data obtained at lower values of the cavitation number have exhibited values as large as 2.8.

2.2.2 Piecewise Linear Fits

In addition to the polynomial type of global fit, piecewise linear fits were obtained over a limited frequency range for $s = i\omega$. The form employed was

$$\text{Real part} = c_1 + c_4 |s|$$

$$\text{Imaginary part} = c_2 + c_3 s/i \tag{9}$$

where the coefficients c_j are real quantities. There is no point in showing these fits since they are essentially coincident with the data in the limited frequency range of applicability.

$\sigma_p = 0.11$

ELEMENTARY MODEL (RESISTANCE)

REAL $[\underline{Z}_{p12}/(1 + \underline{Z}_{p22})]$

MODEL FREQUENCY, Hz
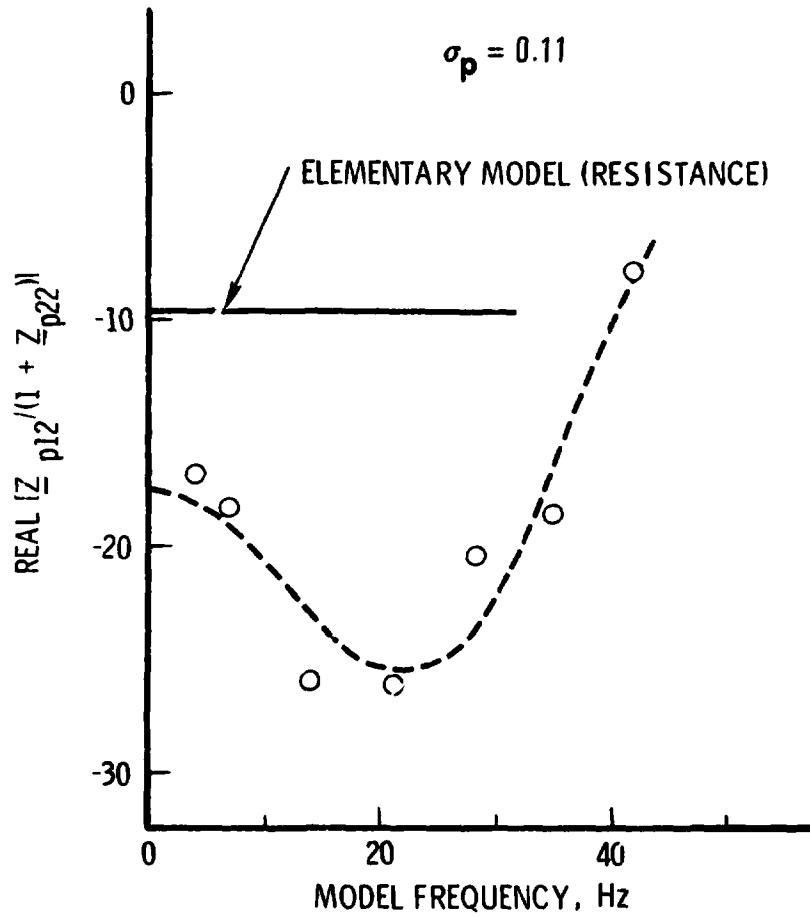
Figure 26. Polynomial Fit (n = 6) of Real
$[\underline{Z}_{p12}/(1+\underline{Z}_{p22})]$

ELEMENTARY MODEL
(INERTANCE X FREQUENCY)

$\sigma_p = 0.11$

IMAGINARY $[\underline{Z}_{p12}/(1 + \underline{Z}_{p22})]$

MODEL FREQUENCY, Hz
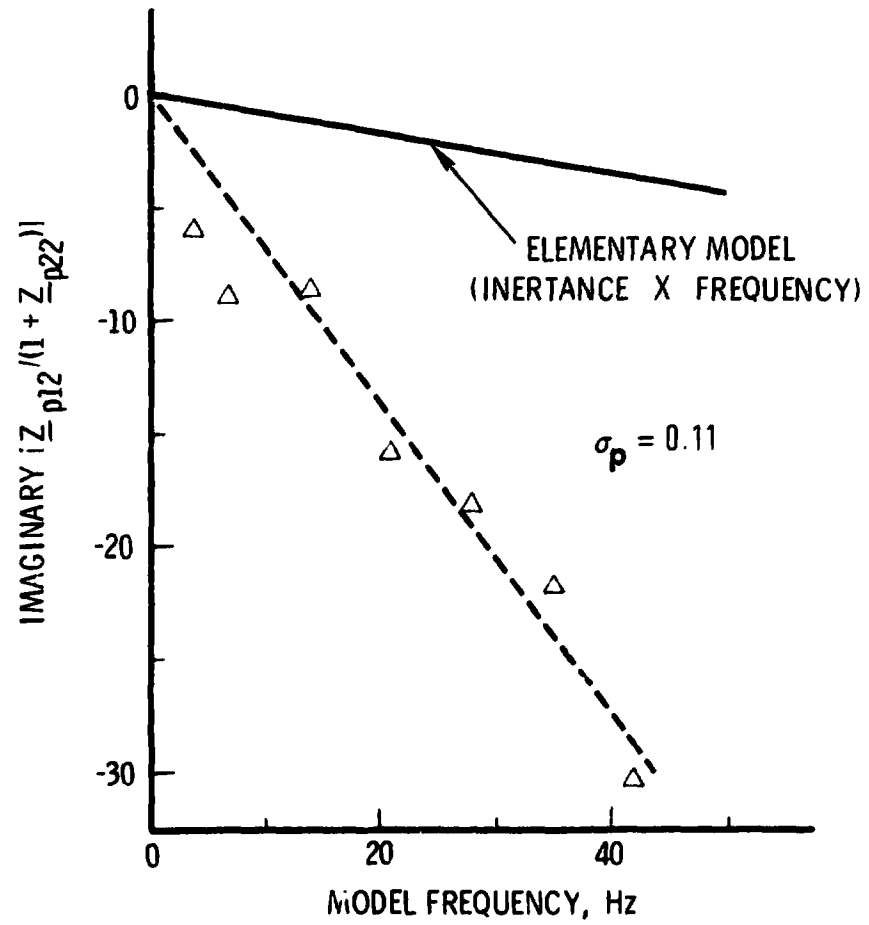
Figure 27. Linear Fit (n = 1) of Imaginary
$[\underline{Z}_{p12}/(1+\underline{Z}_{p22})]$
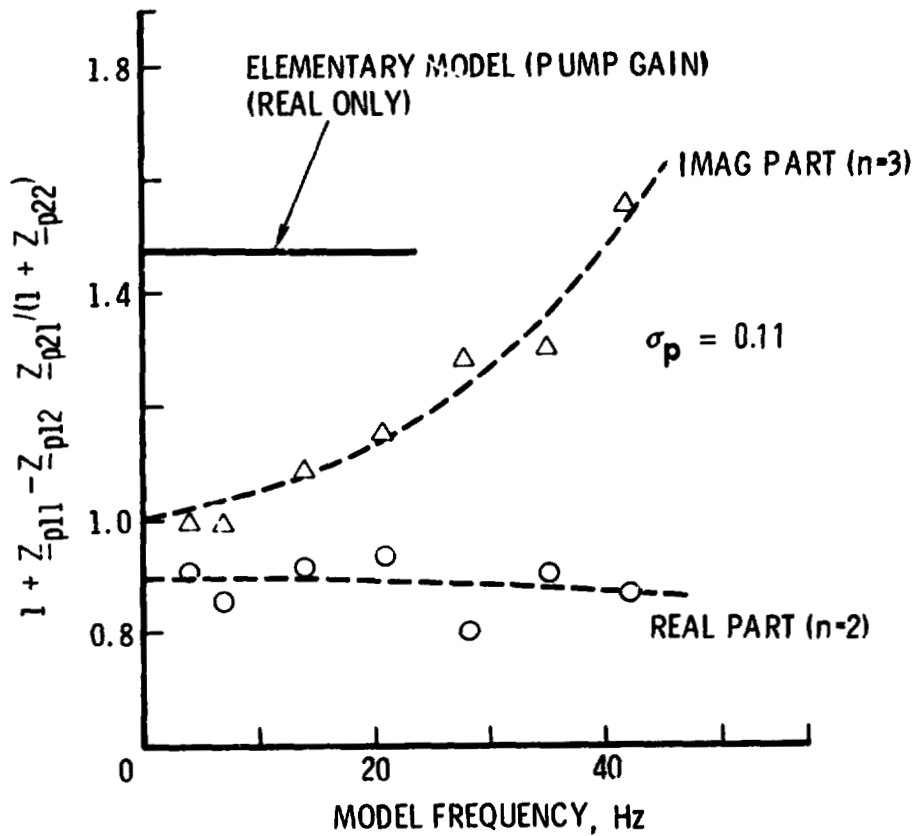
Figure 28. Polynomial Fit of $[1 + \underline{Z}_{p11} - \underline{Z}_{p21}\ \underline{Z}_{p12}/(1 + \underline{Z}_{p22})]$
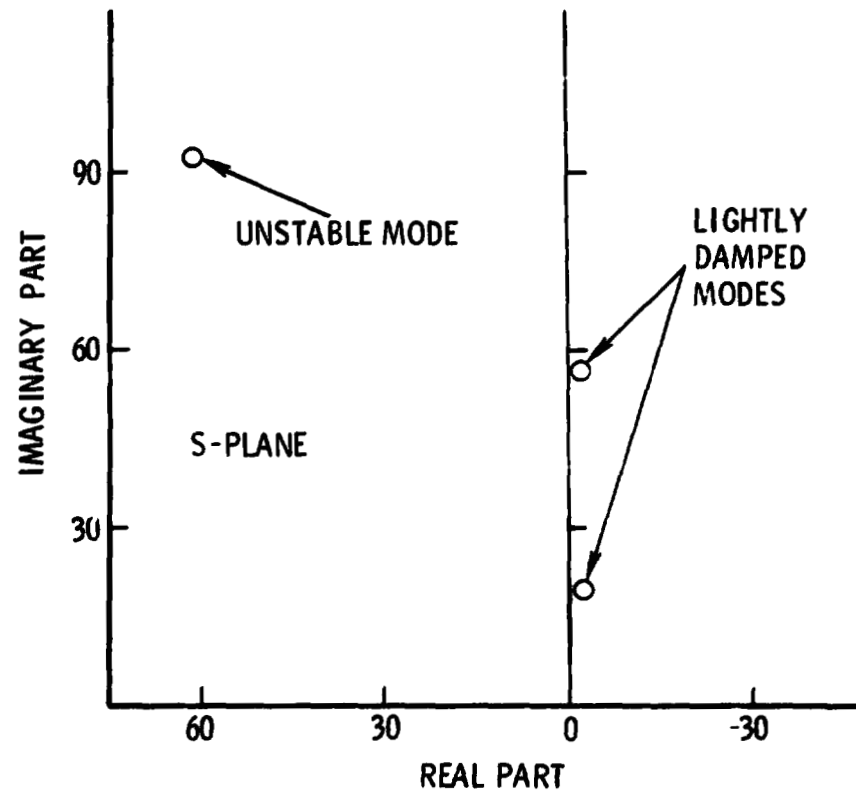
Figure 29. Propulsion System Eigenvalues Calculated with Piecewise Linear Fits of Caltech Transfer Functions

2.2.3 Propulsion System Modes

Concerns about the functional fitting approach arose when it was used to represent the LPOTP and then the modes of the propulsion system were calculated. When these modes were calculated with either the piecewise linear representation or with the global polynomial rep esentation, it was found that unstable modes were predicted for the propulsion system. Although instability is physically possible since the pumps are active elements, the results were viewed with suspicion. One prediction, utilizing a sequential piecewise linear fitting of the experimental data, is shown in Figure 29. The eigenvalues of the propulsion system are plotted in the complex s plane. The very strong instability ($\zeta \simeq -0.7$) was judged to be unreasonable.

A concern with any fitting approach stems from the usage of data derived under simple harmonic conditions ($s = i\omega$) to apply to transient conditions ($s = \sigma + i\omega$). This was emphasized further by the experience gained with the polynomial fitting approach. In this instance it was found that the use of higher-order polynomials (say, $n \geq 6$ or 7) to fit the transfer functions resulted in the prediction of propulsion system instabilities at low frequencies even though the data fits for harmonic conditions looked completely reasonable. In retrospect, the difficulty may have been due to the fact that flow continuity through the pump was not constrained to exist as the frequency went to zero [that is, $Q_d \rightarrow Q_u$ as $\omega \rightarrow 0$; see Eq. (7)]. Thus, the fits should have been constrained such that $1 + \underline{Z}_{p22} \rightarrow 1$ and $\underline{Z}_{p21} \rightarrow 0$ as $\omega \rightarrow 0$. Figures 22 and 24 show that the real parts of the fitted polynomials did not satisfy the continuity requirement. This matter will be explored further in future studies.

2.3 LUMPED PARAMETER MODEL

2.3.1 Description of Model

The lumped parameter model (in electrical analogy form) shown in Figure 30 was developed based upon an initial assessment of the test data. The model of the pump (LPOTP) differs from the usual elementary model of Eq. (1) only in that a parallel resistance-inertance circuit (resistances 2R, inertances L and aL) is employed for the pump flow impedance. The other

two pump elements are the usual cavitation compliance C_p and pump gain $m+1$. The upstream facility section (containing a flow smoothing section with its pressure transducer P_u and an inlet feedline with its flowmeter, $\dot{m}_u$) is represented by the inertance L_u and compliance C_u. It is assumed for the model that the upstream state variables P_u, $\dot{m}_u$ are physically located at the smoother/feedline flange interface (see Figure 21). The physical separation of the actual pressure and flow sensors is believed to be of second-order importance as was assumed in Ref. 6. The inclusion of the compliance C_u represents to first order the small compliance of the smoother transition section and the feedline; this compliance is to be determined from the test data. The upstream inertance $\underline{L}_u = 10.7$ is taken to be that given by the geometry between the smoother/feedline flange and the beginning of the pump blades. The downstream facility section is modeled in a corresponding fashion with inertance $\underline{L}_d = 4.1$ based on geometry and the compliance C_d to be determined from the test data. The compliance C_d is relatively large since it includes the effective compressibility of the relatively voluminous downstream smoothing section.

The Z_{ij} elements for the model of Figure 30, as defined in Eq. (8), are as follows:

$$1 + Z_{11} = (m+1)B - \omega^2(C_p + C_u B)(L_p + L_d) + i\omega R_p(C_p + C_u B) \qquad (10)$$

$$Z_{12} = -R_p B - i\omega[(m+1)L_u + (L_p + L_d)B] \qquad (11)$$

$$Z_{21} = \omega^2(C_p + C_u B)C_d R_p - i\omega\left|(m+1)C_d B + (C_p + C_u B)[1 - \omega^2 C_d(L_p + L_d)]\right| \qquad (12)$$

$$1 + Z_{22} = [1 - \omega^2 C_d(L_p + L_d)]B - \omega^2(m+1)C_d L_u + i\omega C_d R_p B \qquad (13)$$

PHYSICAL DIAGRAM

UPSTREAM SMOOTHER

P_u $\dot{m}_u$

DOWNSTREAM SMOOTHER

PUMP

P_d $\dot{m}_d$

ELECTRICAL DIAGRAM

$P_u, \dot{m}_u$ L_u m+1 2R L L_d $P_d, \dot{m}_d$

C_u C_p 2R aL C_d
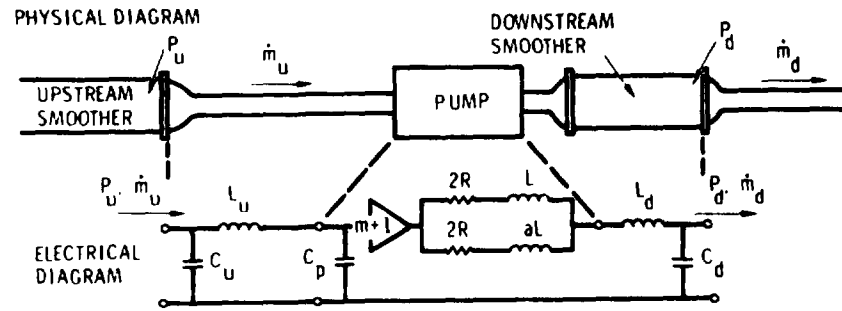
NONDIMENSIONAL PARAMETERS FOR 9000 RPM AND 0.07 FLOW COEFFICIENT

CONSTANT PARAMETERS

L_u · 10 7 C_u · 0 01

L_d · 4 1 C_d · 0 174

R · 16 6 L · 320 a · 0.04

PARAMETERS VARYING WITH CAVITATION NUMBER:

σ_p	0 513	0 114	0 046	0.024
m+1	1	1 16	1 5	5
C_p	0	0 05	0 3	0 6

Figure 30. First-cut Pump Mathematical Model

$(\sigma_p \cdot 0.513)$

—— $\mathrm{Re}Z_{p12}/R$

– – – $\mathrm{Im}Z_{p12}/R$

2R L

2R aL

NORMALIZED REAL AND IMAGINARY PARTS

$\Omega \cdot \omega L/R$
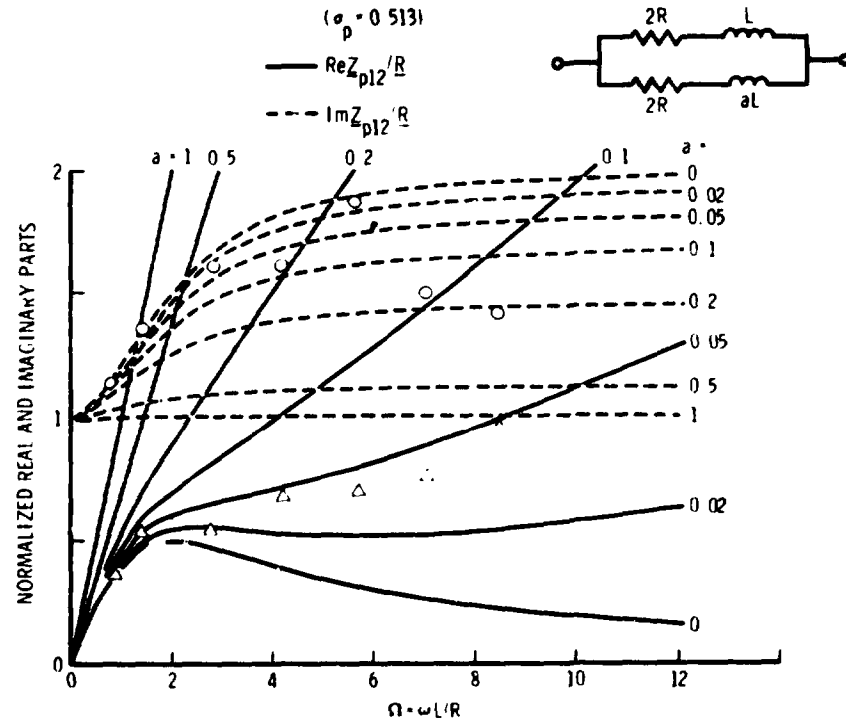
Figure 31. Normalized Pump Impedance with Test Data under Noncavitating Conditions ($\sigma_p = 0.513$)

where

$$\frac{R_p}{R} = \frac{2[2+\Omega^2(1+a^2)]}{4+\Omega^2(1+a)^2} \qquad (14)$$

$$\frac{\omega L_p}{R} = \frac{2\Omega(1+a)(1+\Omega^2 a)}{4 + \Omega^2(1+a)^2} \qquad (15)$$

$$\Omega = \omega L/R$$

$$B = 1 - \omega^2 C_p L_u$$

As previously noted, the values of L_u and L_d are found from feedline geometry. The values of the other parameters (C_u, C_p, C, R, L, a, $m+1$) are to be determined from a matching of the above Z_{ij} elements with their experimental values over the range of test excitation frequencies. It is assumed that only the pump cavitation compliance C_p and the pump gain $m+1$ vary with the pump cavitation number σ_p. As previously stated, data for four values of cavitation number σ_p are employed for this stuvy.

The basis for the parallel representation of the pump flow impedance Z_{p12} is the experimentally observed nature of the variation with frequency of its real and imaginary parts. From Eq. (11) we see that the impedance Z_{p12} is given for the fully wetted or noncavitating ($C_p = 0$, $m+1 = 1$) conditions by

$$Z_{p12} = Z_{12} - i\omega(L_u + L_d) \qquad (16)$$

Figure 31 shows normalized Z_{p12} data for the fully wetted case ($\sigma_p = 0.513$) superimposed on a family of curves for the parallel circuit shown with a as the parameter. Two normalization factors are employed. One is the steady-state pump resistance R obtained in the usual fashion from pump steady performance data as the negative of the partial derivative of the pump head with respect to pump flow; from Figure 5.2 of Ref. 6 the value $\underline{R} = 16.6$ is obtained.

The second normalization factor is $\eta = 0.8$ to account for a suspected error in the calibration of the upstream flow measurement $\dot{m}_u$. This error was rationalized on the basis that this flow was the most suspect measurement and that it is necessary for Re $Z_{22} \rightarrow 0$ as $\omega \rightarrow 0$ so that inflow equals outflow under steady flow conditions. The experimental data indicated that Re $Z_{22} \rightarrow \simeq 0.2$ instead. Let us assume that the actual flow $\dot{m}_u = \eta \dot{m}'_u$, where $\dot{m}'_u$ is the measured flow; the value $\eta = 0.8$ provides the indicated correction. Since the Z_{ij} are determined using the measured flow $\dot{m}'_u$, the corrected transfer matrix becomes

$$
\left\{ \begin{array}{c} P_d \\ \\ \dot{m}_d \end{array} \right\}
\left[\begin{array}{cc} 1+Z_{11} & Z_{12}/\eta \\ \\ Z_{21} & (1+Z_{22})/\eta \end{array} \right]
\left\{ \begin{array}{c} P_u \\ \\ \dot{m}_u \end{array} \right\}
\tag{17}
$$

As a consequence, the experimental data for Z_{12} were divided by $\eta = 0.8$ before Z_{p12} was evaluated using Eq. (16).

The value of a (between 0 and 1) determines the high frequency asymptote of the real part at a value of between one and two times the steady-state resistance R; this matches the trend of the test data shown on Figure 31 and also the trend of data obtained in another test program (for example, see Figure 9 of Ref. 14). It is informative to note that a = 1 yields the expected result $Z_{p12} = R + i\omega L/2$. The match between the data and the mathematical model shown on Figure 31 was achieved by trial and error using the value $\underline{L}$ = 320 which establishes the scaling of abscissa values. The correlation, most particularly for the imaginary part data, suggests the value a = 0.04. Note that these are the values appearing on Figure 30.

Thus far, the values of $\underline{L}_u$ and $\underline{L}_d$ were determined by feedline geometry, $\underline{R}$ from the pump performance data, $\underline{L}$ and a from the matching to the

circuit shown in Figure 31. The remaining parameters were evaluated as follows:

$$m+1 = Re(1+\underline{Z}_{11}) \text{ (low } \underline{\omega})$$ (18)

$$\underline{C}_d = \frac{Im\underline{Z}_{22}}{\omega Re\underline{Z}_{12}} \text{ (low } \underline{\omega})$$ (19)

$$\underline{C}_u + \underline{C}_p = \frac{Re\underline{Z}_{21}}{\underline{\omega Im}\underline{Z}_{22}} = - \frac{Im\underline{Z}_{21}}{\underline{\omega Re}\underline{Z}_{12}} \text{ (low } \underline{\omega})$$ (20)

For the fully wetted case ($\underline{C}_p = 0$, $m+1 = 1$), Eq. (20) provides the basis for the value of $\underline{C}_u$. Thus, all of the model parameters are determined. The values appear on Figure 30.

2.3.2   Evaluation of Results

Figures 32 through 39 show the calculated real and imaginary parts of the $\underline{Z}_{ij}$ elements versus frequency from the mathematical model in Figure 30. The results are encou. ging in that the model does qualitatively show most of the major trends in the data, particularly for the two higher cavitation numbers.

Available information on steady engine operation in flight yields a range of cavitation numbers from about 0.1 to 0.4. Thus, the test condition cavitation number $\sigma_p = 0.114$ is the most representative of flight operating conditions. A review of Figures 32 through 39 shows that the match for this value of σ_p is relatively good. The matches for $Im\underline{Z}_{11}$ and $Re\underline{Z}_{21}$ are particularly noteable. The matches for $Re\underline{Z}_{12}$, $Im\underline{Z}_{12}$, $Re\underline{Z}_{22}$, and $Im\underline{Z}_{22}$ are better than they appear at first glance when the factor 1.25 (equal to $1/\eta$) is applied to the data [Eq. (17)]. The other two cases, $Re\underline{Z}_{11}$ and $Im\underline{Z}_{21}$, show moderately good correlation; in each case a constant factor would move the experimental data points into a much improved match to the mathematical model.
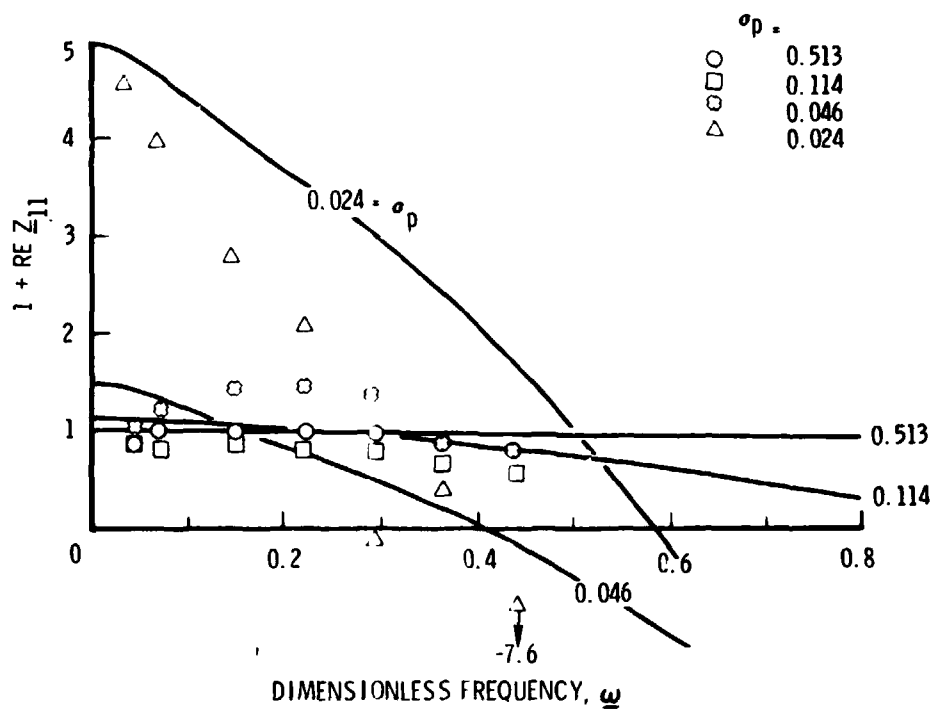
Figure 32. Real Part of $1+\underline{Z}_{11}$
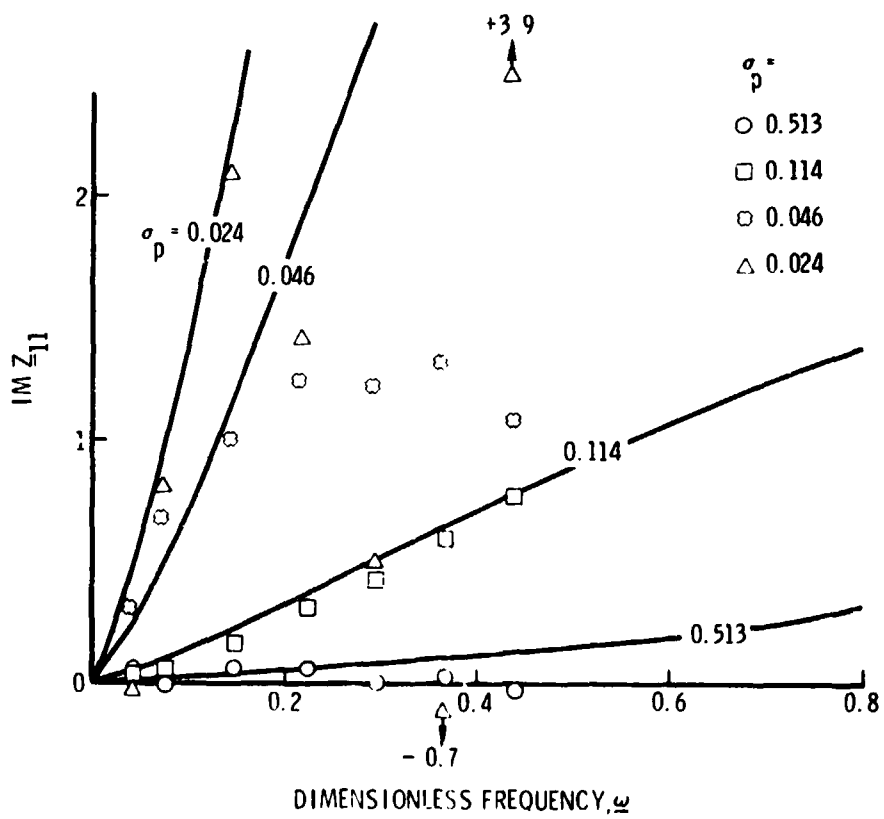
Figure 33. Imaginary Part of $\underline{Z}_{11}$
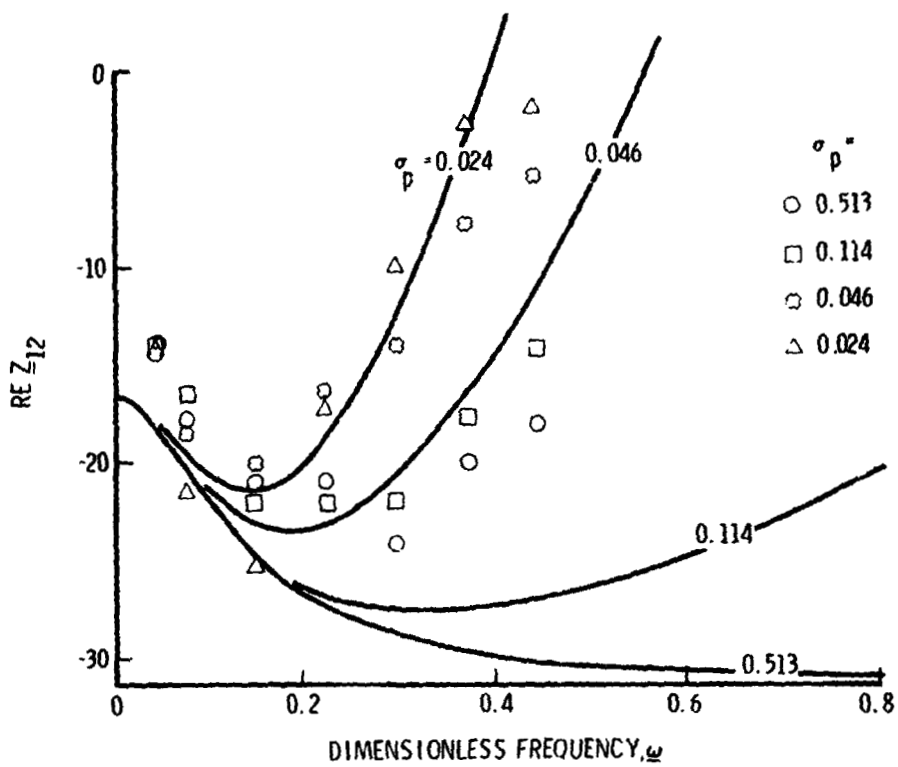
Figure 34. Real Part of $\underline{Z}_{12}$
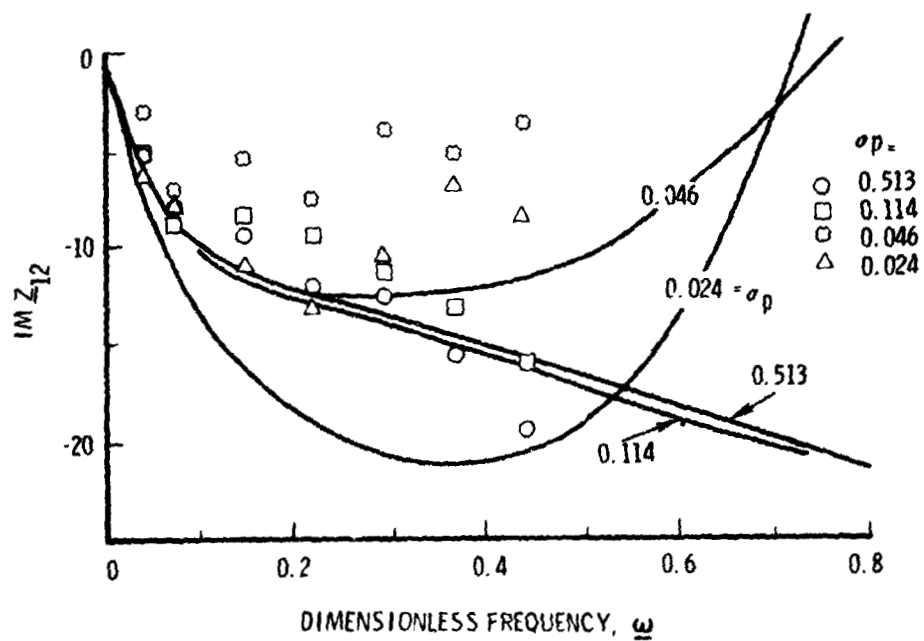
Figure 35. Imaginary Part of $\underline{Z}_{12}$
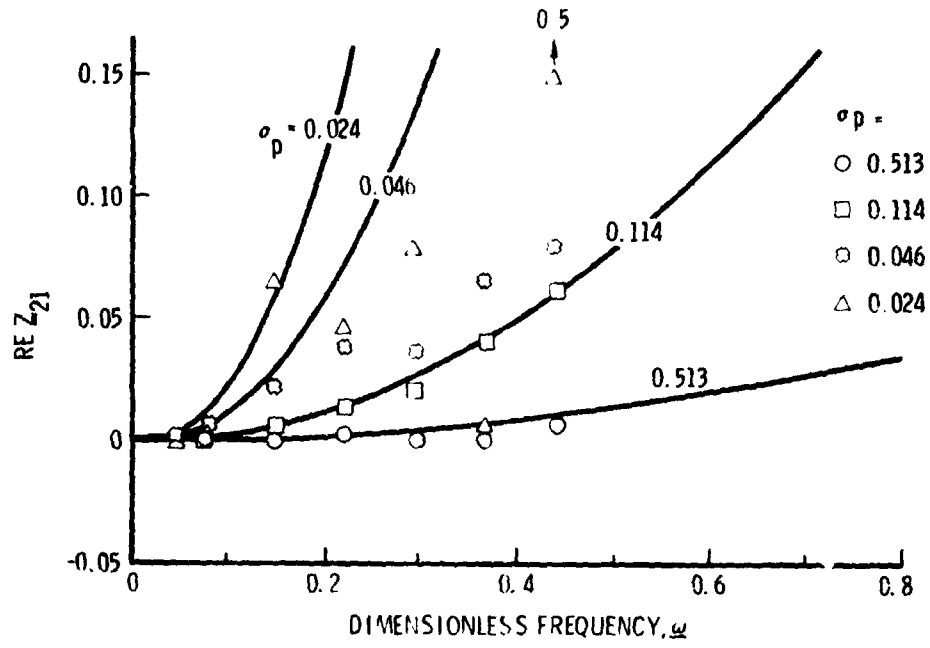
Figure 36. Real Part of $\underline{Z}_{21}$
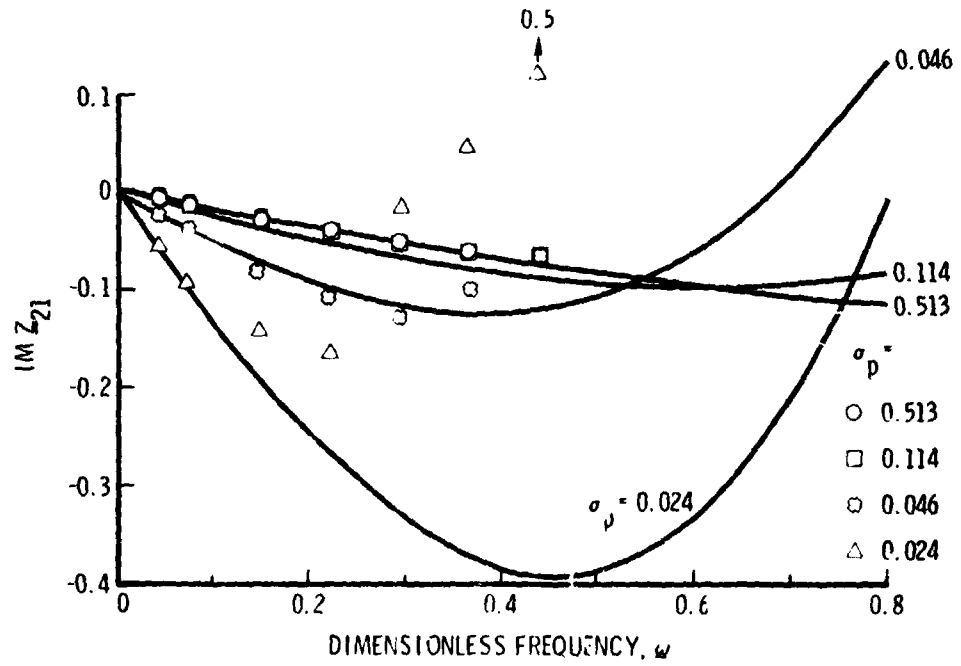
Figure 37. Imaginary Part of $\underline{Z}_{21}$

2-21
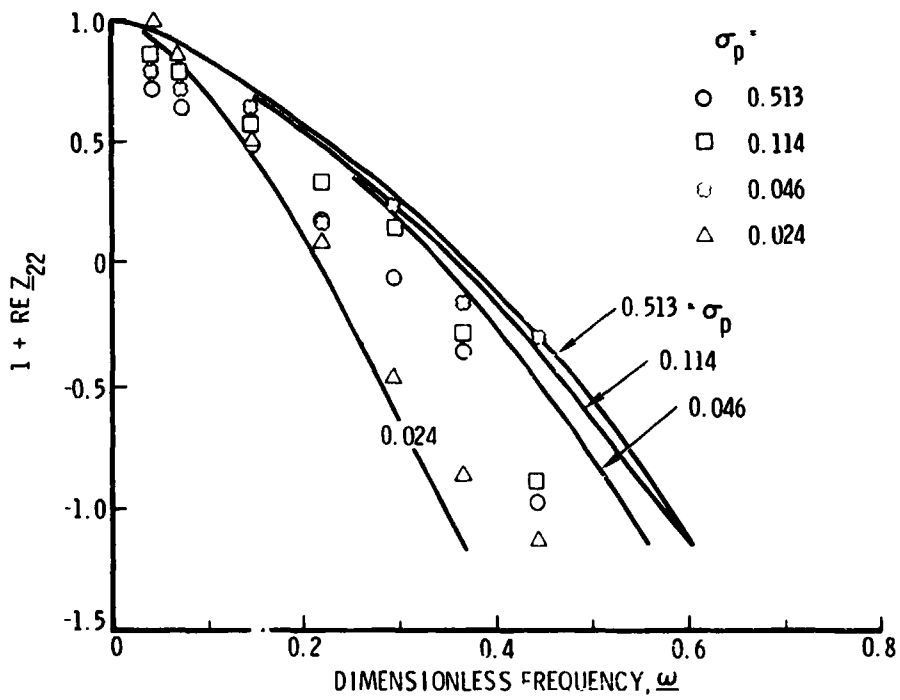
Figure 38. Real Part of $1 + \underline{Z}_{22}$
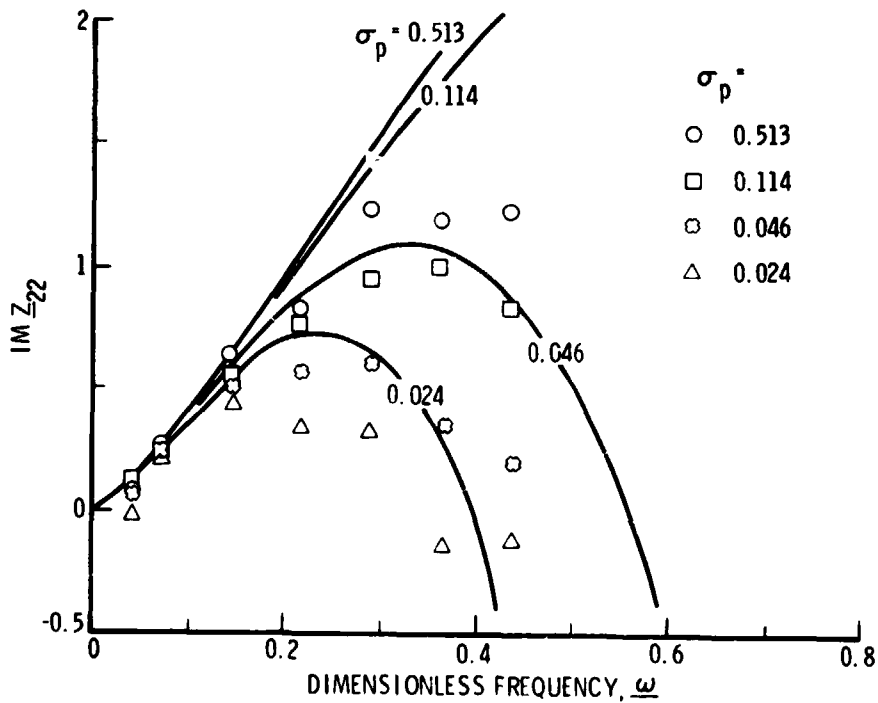
Figure 39. Imaginary Part of $\underline{Z}_{22}$

2-22

For the most part the model provides a good match at low frequencies. Special attention is called to the initial shape of $\text{Im} \dot{Z}_{21}$ which reflects the total compliance and pump gain as follows [see Eq. (12)]:

$$- \underline{Z}_{21}(\omega)/\underline{\omega} \xrightarrow[\underline{\omega} \to 0]{} (m+1) \, \underline{C}_u + \underline{C}_p + \underline{C}_u \qquad (21)$$

On the other hand, the poor quantitative high-frequency correlation at the lower cavitation numbers strongly suggests that further model development is needed for an adequate description of pump dynamics under conditions of major cavitation. For example, such conditions may occur during the after-SRB-separation transient and during a lox depletion where the lox surface moves well down the feedline prior to engine shutdown.

2.4   SUMMARY

Two preliminary studies were made for the use of the Caltech experimental results for modeling the LPOTP. Each study showed questionable results. Further efforts along both lines are planned for the future.

In the first study two forms of functional fitting, global polynomial fits and piecewise linear fits, were applied to the Caltech pump data. Concerns about the validity of the results for use in stability analyses arose because various instabilities were predicted for the main propulsion system when the fitted functions were employed for the LPOTP.

The second study was aimed at developing a lumped parameter, physically based model. The result was the model shown on Figure 30. A comparison of the results from this model with the measured data appears on Figures 31 through 39. The comparison shows an encouraging similarity in the major trends, particularly for the cavitation number most representative of steady flight operation ($\sigma_p = 0.114$) and higher. However, several matters need to be investigated and resolved before such a model can be accepted:

    a.   The need for the correction of the upstream flow data to achieve continuity for steady flow

b.   The poor quantitative correlation at high frequencies at
     low cavitation numbers

c.   The use of the model to calculate hydraulic modes of the
     Caltech test system to verify a lack of major discrepancy
     with observed self-excited system oscillations.

3. INITIAL POGO STUDY OF OMS OPERATION

An exploratory evaluation of pogo stability during operation of the orbital maneuvering subsystem (OMS) is described in this section. The concern is prompted by the fact that two other vehicles powered by generally similar pressure-fed engines (see Table 3), namely the Deita Stage II and the French Diamant B Stage I, have experienced strong pogo instability in flight (Refs. 15 and 16). The Delta Stage II, powered by a derivative lunar module descent engine (LMDE), has experienced sustained peak axial vibrations of up to 45 g at 125 Hz. The vehicle structural mode was a local one involving primarily engine axial motion with some interaction with the vehicle tanks. The Diamant B had experienced vibrations as high as 20 g at 45 Hz in the second longitudinal mode of the overall vehicle. The Delta Stage II pogo has apparently been corrected by ballasting the engine with a 19.5 kg mass (43 lb) to reduce the structural gain. The Diamant B instability was suppressed by a combination of stiffening of the junction of the thrust structure with the aft propellant tank (to reduce structural gain) and by bonding viscoelastic material around the aft half of the same tank (to increase structural damping). It is noteworthy also that both the Delta Stage II and the Diamant B Stage I underwent pogo instability during stage static firings. The overall lesson for the Shuttle is that pogo prevention should be vigorously pursued on the OMS.

The following sections deal with preliminary structural and propulsion dynamic models, studies to investigate mechanisms for potential instabilities, and an initial look at suppression for an identified potentially strong destabilizing mechanism. Details of the models are found in Appendices C and D.

3.1 OMS STRUCTURAL DYNAMICS MODEL

The OMS pod illustrated in Figure 40 is assumed to be fixed at the orbiter fuselage interface with the major portion of its mass concentrated in the OMS and RCS propellant tanks, the OMS high-pressure helium storage

Table 3. Selective Comparison of OMS with Pressure-Fed
Vehicles Experiencing Pogo Phenomena

	OMS	Delta Stage II	Diamant B Stage I
Engine Mass	113-122 kg (250-270 lbm)	104-132 kg (230-290 lbm)	(Unknown)
Thrust	27 kN (6000 lbm)	44 kN (10,000 lbm)	40 kN (9000 lbm)
Propellants	MMH, N_2O_4	UDMH, N_2O_4	UDMH, N_2O_4
I_{sp}	3070 Ns/kg (313 sec)	2960 Ns/kg (302 sec)	2880 Ns/kg (294 sec)
Frequency	45 Hz	125 Hz	45-47 Hz
Structural Mode	Local Engine	Engine with Tanks	Second Longitudinal, Large Engine Motion
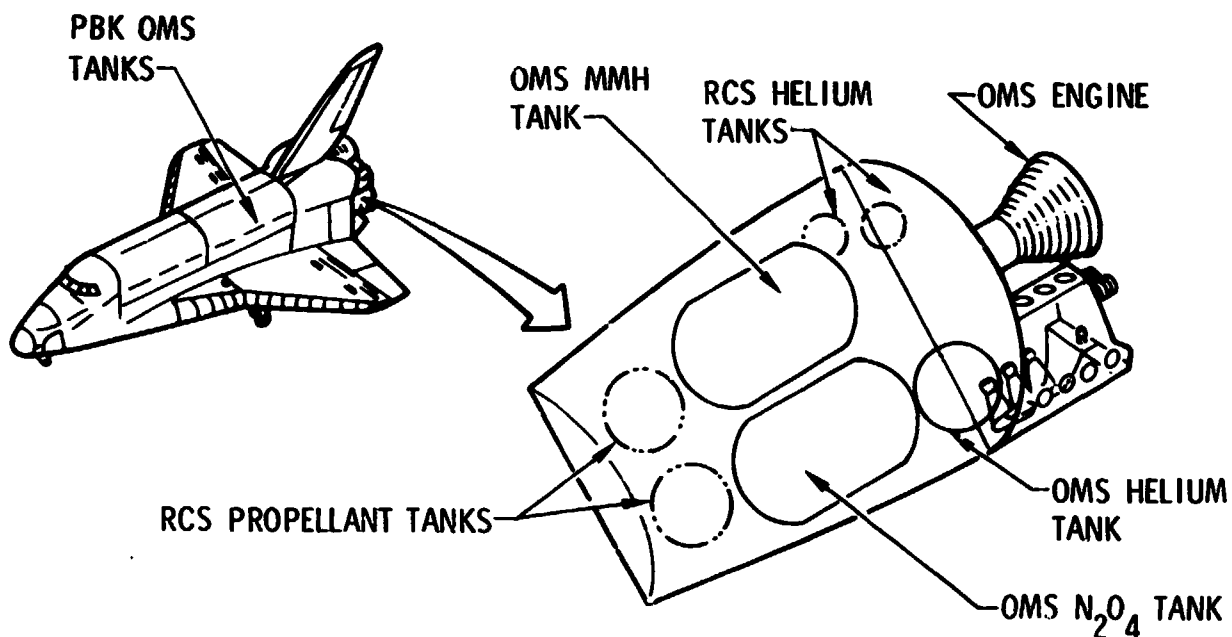
Figure 40. OMS General Arrangement

bottle, the RCS thruster arrangement and the OMS engine. The pod structure consists of aluminum and titanium truss members of skin and stringer construction, and reinforced panels. Mass and flexibility matrix data were based on a 123-DOF mathematical model supplied by the Rockwell International Space Division (RI/SD).

A set of OMS pod structural dynamic modes (corresponding to the 100 percent fill condition in all propellant tanks) was calculated by RI/SD. The tanks were assumed rigid with flexible aft bulkhead supporting structure. The lowest tank-dominated OMS longitudinal modal frequencies were at 10.0 and 12.6 Hz. In addition, a high-gain localized engine axial mode was calculated at 43.5 Hz.

3.1.1 Simplified OMS Pod Structural Modes

An independent calculation of pod structural modes was carried out since the RI/SD supplied data were limited to the 100 percent fill condition and the assignment of a single pod structural mass point at the pod center of gravity was not thought to be adequate for pogo analysis.

The RI/SD assumption of rigid propellant tanks was first examined with an elementary flexible tank model (Ref. 17) supported by a ring at the aft dome/cylinder interface which connects to a support spring. The modes of this simplified model verified that a rigid tank model is valid for all propellant fill conditions for frequencies below 100 Hz.

For the present investigation, a simplified 11-DOF longitudinal dynamic model with engine lateral dynamics wa sembled. The model with selected significant mass points is illustrated in .gure 41 and the RI/SD based mass and flexibility matrices are presented in Appendix C. In the absence of distributed structural mass data, a conservative approach was taken whereby the structural mass (lumped at its center of gravity by RI/SD) was completely ignored. The burn time dependent tank masses were taken as functions of propellant level with μ and ν denoting the OMS and RCS fractional fill levels, respectively.

ENGINE (5 DOF)

OMS FUEL TANK

RCS FUEL TANK

RCS THRUSTERS

OMS H_e TANK

OMS OX TANK

RCS OX TANK

POD FIXED AT ORBITER I/F
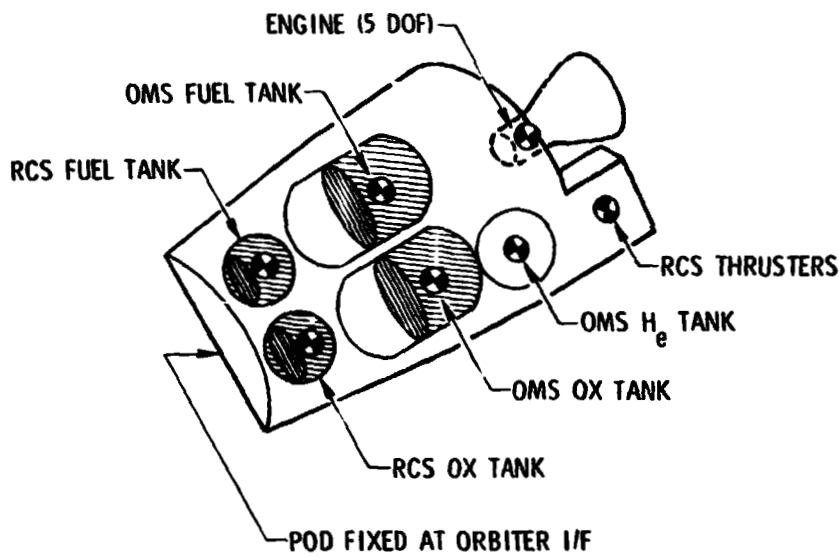
MODEL INCLUDES VARYING PROPELLANT MASS

OMS FUEL $\leq$ 2041 kg (4505 lbm)   RCS FUEL $\leq$ 371 kg (817 lbm)
OMS OX $\leq$ 3372 kg (7433 lbm)   RCS OX $\leq$ 616 kg (1357 lbm)

Figure 41. 11-DOF OMS Structural Dynamic Model
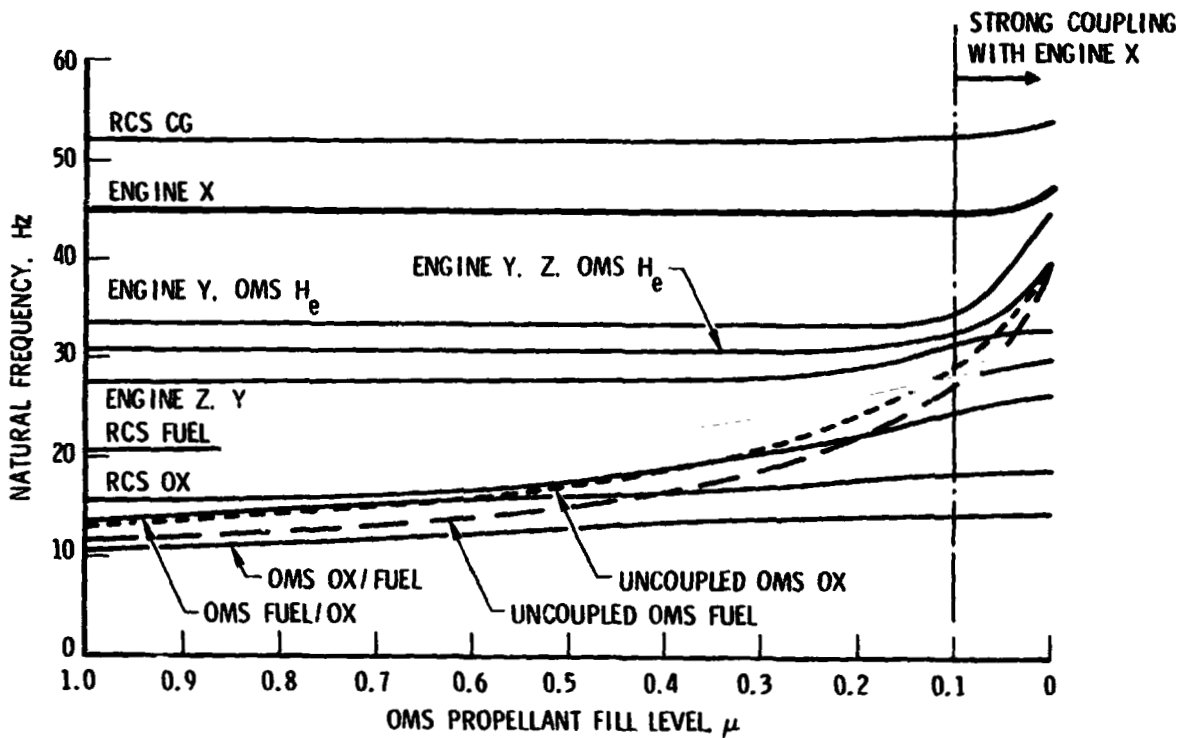
Figure 42. OMS Pod Structural Mode Frequencies vs.
OMS Propellant Level (RCS 100% Full)

3-4

Calculation of the modes as a function of OMS propellant level was carried out. The mode spectra are presented in Figures 42 through 44 for three RCS propellant fill levels of 100, 50, and 1 percent, respectively. In general, the results indicate a persistance of the localized high-gain engine axial mode at 45 Hz (versus RI/SD calculated 43.5 Hz) for nearly all propellant levels. Some splitting with OMS tank-dominated modes occurs near tank depletion. Typically the modal mass associated with the engine localized mode is about 128 kg (282 lbm) with $\phi_e = 1$ (slightly above the assumed engine mass of 113 kg (250 lbm). Tank-dominated modes, which increase in frequency with propellant consumption, potentially contribute to pogo destabilization trends. In these modes engine gimbal motion is of the same order as the tank axial motion and high tank bottom modal pressures and motions provide for strong propulsion system coupling. A summary of engine dominated (45 Hz) and significant tank dominated mode spectrum parameters are presented in Appendix C.

3.1.2   Conservative Upper Bounds on Modal Gain

In view of the preliminary nature of the current OMS structural dynamic model, a simplified description resulting in a conservative estimate of modal gain was constructed for parametric study of the pogo phenomenon. If one assumes that the contributions to modal mass (i.e., modal kinetic energy) are due only to engine axial motion and OMS propellant tank motion, the modal mass is expressed as

$$M_\phi = M_e + \phi_{tf}^2 (M_{tf_s} + \mu M_{tf_p}) + \phi_{to}^2 (M_{to_s} + \mu M_{to_p}) \qquad (22)$$

where the engine modal displacement is taken as unity ($\phi_e = 1$). The above expression represents a lower bound on modal mass for a given mode shape since typically there would be contributions due to other components (i.e., RCS tankage). The lower bound modal mass yields an upper bound in engine modal gain (ϕ_e^2/M_ϕ). With the tanks contributing to the increase in modal mass (or decrease in engine modal gain), there are associated modal tank
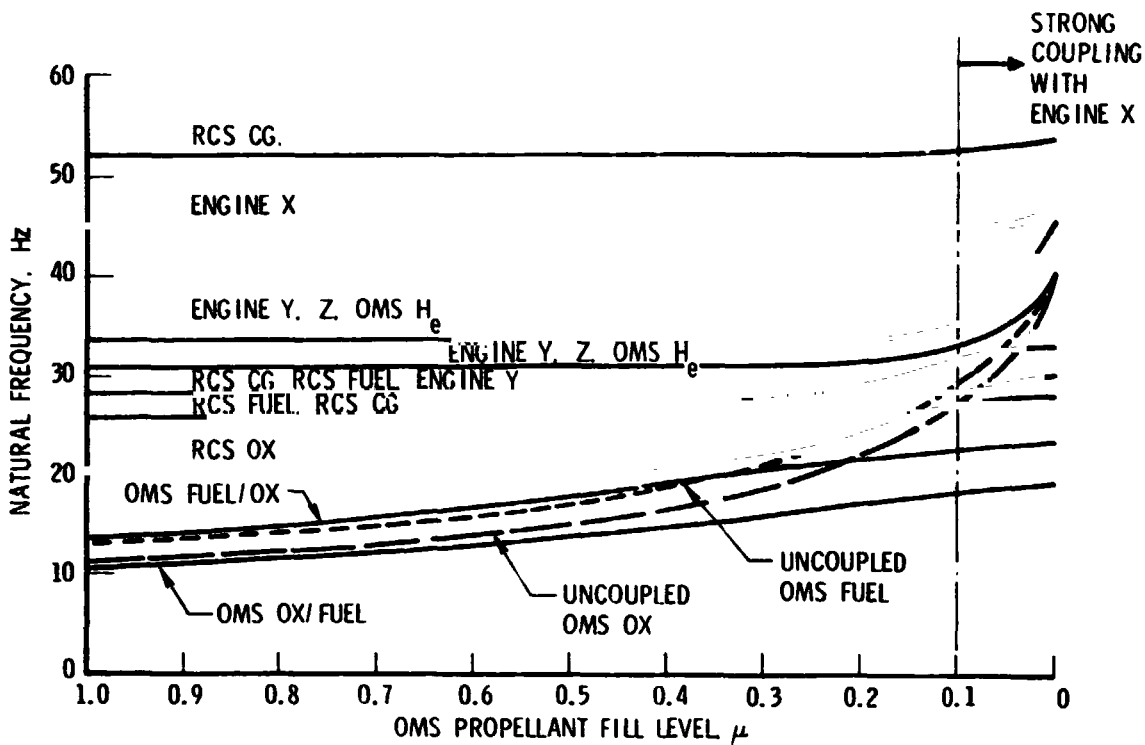
Figure 43. OMS Pod Structural Mode Frequencies vs.
OMS Propellant Level (RCS 50% Full)
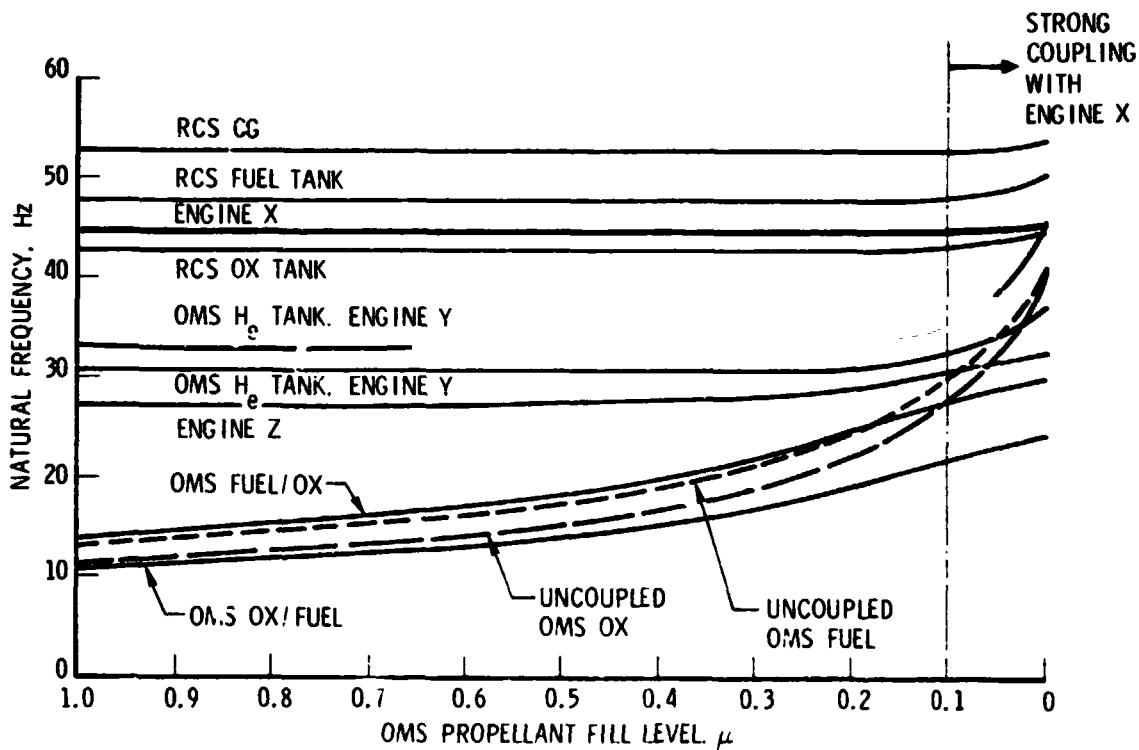
Figure 44. OMS Pod Structural Mode Frequencies vs.
OMS Propellant Level (RCS 1% Full)

bottom pressures (for closed tanks) which are expressed approximately as

$$P_{tf} = \mu \rho_f \ell_t \phi_{tf} \ddot{X}_e, \qquad P_{to} = \mu \rho_o \ell_t \phi_{to} \ddot{X}_e \tag{23}$$

for the fuel and oxidizer tanks, respectively. Note that the tank length, ℓ_t, is the same for fuel and oxidizer tanks.

For the purposes of a preliminary sensitivity study, the following modal parameters are varied: (1) tank modal displacements and (2) modal frequency in the range of 20 to 65 Hz (within which tank-dominated and engine-dominated modes occur for the 11-DOF model described in the previous section).

3.1.3   Structural Mode Representation for Pogo Analysis

The representation of modes for closed-loop pogo analysis employs adjustments for open tank/feedline fluid interfaces and the associated reactions (Ref 1). For convenience, volumetric outflow displacements $(\mathcal{S})$ relative to closed tank bottoms have been chosen as generalized flow coordinates. The resulting dynamic equations associated with a single structural mode expressed in a convenient form for organization of the stability equations are

$$
\begin{pmatrix}
M_\phi & & & & \\
& & & -\rho_f \ell_t \mu & \\
& & & & -\rho_o \ell_t \mu \\
& -\rho_f \ell_t \mu & & L_{tf} & \\
& & -\rho_o \ell_t \mu & & L_{to}
\end{pmatrix}
\begin{Bmatrix}
\ddot{X}_e \\
\ddot{X}_{tf} \\
\ddot{X}_{to} \\
\ddot{\Theta}_{tf} \\
\ddot{\Theta}_{to}
\end{Bmatrix}
$$

$$
+
\begin{pmatrix}
2\zeta_\phi \omega_\phi M_\phi & & & & \\
& & & & \\
& & & & \\
& & & R_{tf} & \\
& & & & R_{to}
\end{pmatrix}
\begin{Bmatrix}
\dot{X}_e \\
\dot{X}_{tf} \\
\dot{X}_{to} \\
\dot{\Theta}_{tf} \\
\dot{\Theta}_{to}
\end{Bmatrix}
\tag{24}
$$

$$
+
\begin{pmatrix}
\omega_\phi^2 M_\phi & & & & \\
& & & & \\
& & & & \\
& & & & \\
& & & &
\end{pmatrix}
\begin{Bmatrix}
X_e \\
X_{tf} \\
X_{to} \\
\Theta_{tf} \\
\Theta_{to}
\end{Bmatrix}
=
\begin{Bmatrix}
F_e \\
F_{tf} \\
F_{to} \\
P_{tf} \\
P_{to}
\end{Bmatrix}
$$

where $F_e' = F_e + F_{ef} + F_{eo}$. These equations are subjected to the modal constraint

$$
\begin{Bmatrix} X_e \\ X_{tf} \\ X_{to} \\ \Theta_{tf} \\ \Theta_{to} \end{Bmatrix} = \begin{pmatrix} 1 & & \\ \phi_{tf} & & \\ \phi_{to} & & \\ & 1 & \\ & & 1 \end{pmatrix} \begin{Bmatrix} X_e \\ \Theta_{tf} \\ \Theta_{to} \end{Bmatrix} \tag{25}
$$

In the present analysis the outflow inertances L_{tf} and L_{to} are neglected since they are generally irsgnificant (Ref. 1), and the outflow resistances R_{tf} and R_{to} are included in the feedsystem model and thus not included again in the structural model.

It should be noted that the tank bottom reaction terms, F_{tf} and F_{to}, the generalized interaction forces, F_{ef} and F_{eo}, and the tank bottom pressures, P_{tf} and P_{to}, ultimately do not appear explicitly in the final closed-loop stability equations. Equal and opposite interface loads are applied to the feedsystem, and oupling of the pod and feedsystem substructures results in the automatic cancellation of the explicit interface loads; they appear implicitly as mass, damping and stiffness coupling terms in general. This is the same mathematical phenomenon that occurs in modal coupling and substructure analysir; it is guaranteed as a consequence of the Lagrange equations.

3.2   PROPULSION SYSTEM MODEL

The OMS includes interpod and PBK-pod feedlines as well as intra-pod interconnections to the RCS. The present analysis is limited to the basic propellant delivery configuration. For the purpose of the current early pogo study, the geometrically complex feedlines and engine manifolding are assumed subject to axial-only structural motion excitations in a manner consistent with the pod structural model. Moreover, since feedline bracketry was not finalized when configuration data were obtained, the excitations are

limited to tank support structure axial motion and engine gimbal axial motion. A lumped parameter, finite element description of the feedlines and engine manifolding was chosen due to the geometric complexity of the system.

The remaining component of the propulsion system model is the description of combustion dynamics. The linear combustion model includes constants derived from steady performance data and the usual time lag and delay constants.

3.2.1   Feedsystem

The intrapod feedlines for fuel and oxidizer consist of all line sections between the tank interfaces and engine manifold interfaces including the side branches leading to closed crossfeed valves and line sections on the OMS engine. The three-dimensional geometry of the feedlines is approximated by a planar, longitudinal-lateral configuration with the longitudinal runs properly scaled. Such an approximation provides for proper accounting of the longitudinal hydraulic acceleration heads required for the present idealization.

The lumped parameter, finite element feedline and engine manifold models are illustrated in Figures 45 and 46 for the fuel and oxidizer circuits, respectively. Hydraulic data for the fuel and oxidizer circuit models and details of the models are presented in Appendix D. The chosen set of dynamic variables consists of (1) volumetric flow displacements Θ at fluid nodes taken relative to local line structural motion and (2) line structural displacement X_s. Assuming generally negligible longitudinal flexibility of the line structure and allowing rotation of corners due to restrained bellows (universal joints), one finds the feedline dynamic equations take the form

$$
\begin{pmatrix} L & (\rho h) \\ (\rho h)^T & M_{rig} \end{pmatrix} \begin{Bmatrix} \ddot{\Theta} \\ \ddot{X}_s \end{Bmatrix} + \begin{pmatrix} R & 0 \\ 0 & 0 \end{pmatrix} \begin{Bmatrix} \dot{\Theta} \\ \dot{X}_s \end{Bmatrix} + \begin{pmatrix} K & 0 \\ 0 & 0 \end{pmatrix} \begin{Bmatrix} \Theta \\ X_s \end{Bmatrix} = \begin{Bmatrix} \Gamma_t P_f - \Gamma_c P_c \\ -F_s \end{Bmatrix}
$$

$$(26)$$
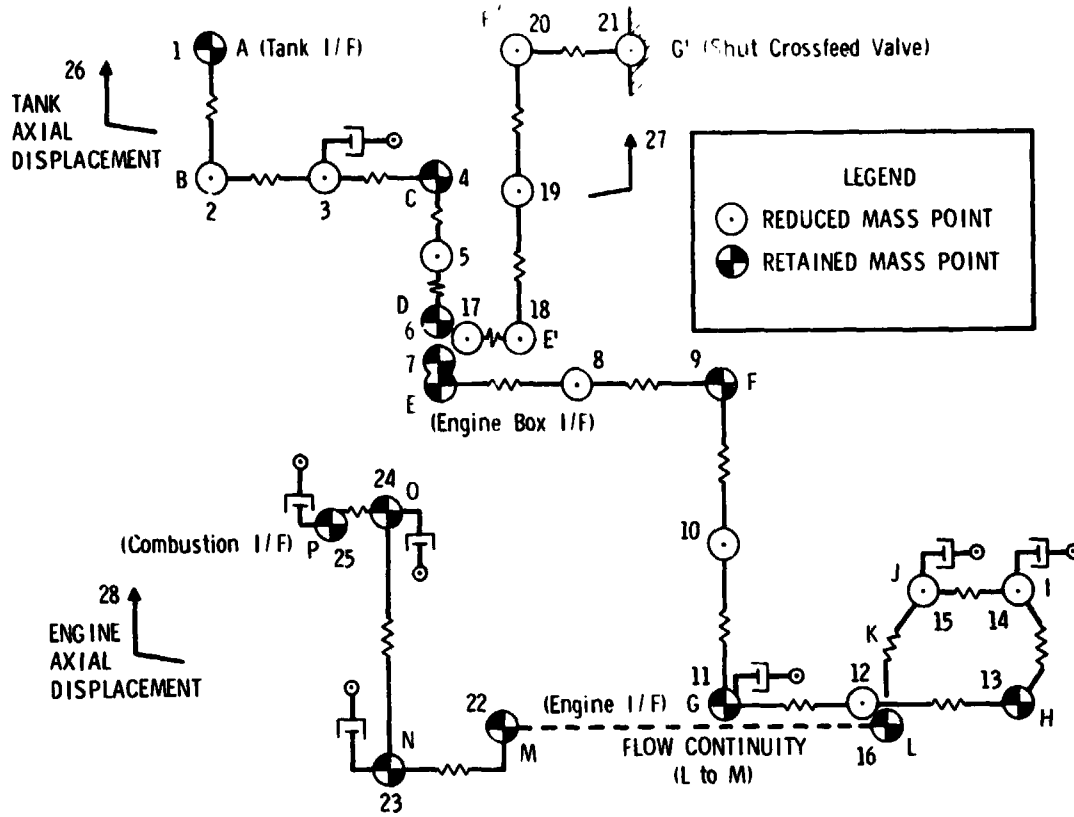
Figure 45.   OMS Fuel Circuit Model Schematic
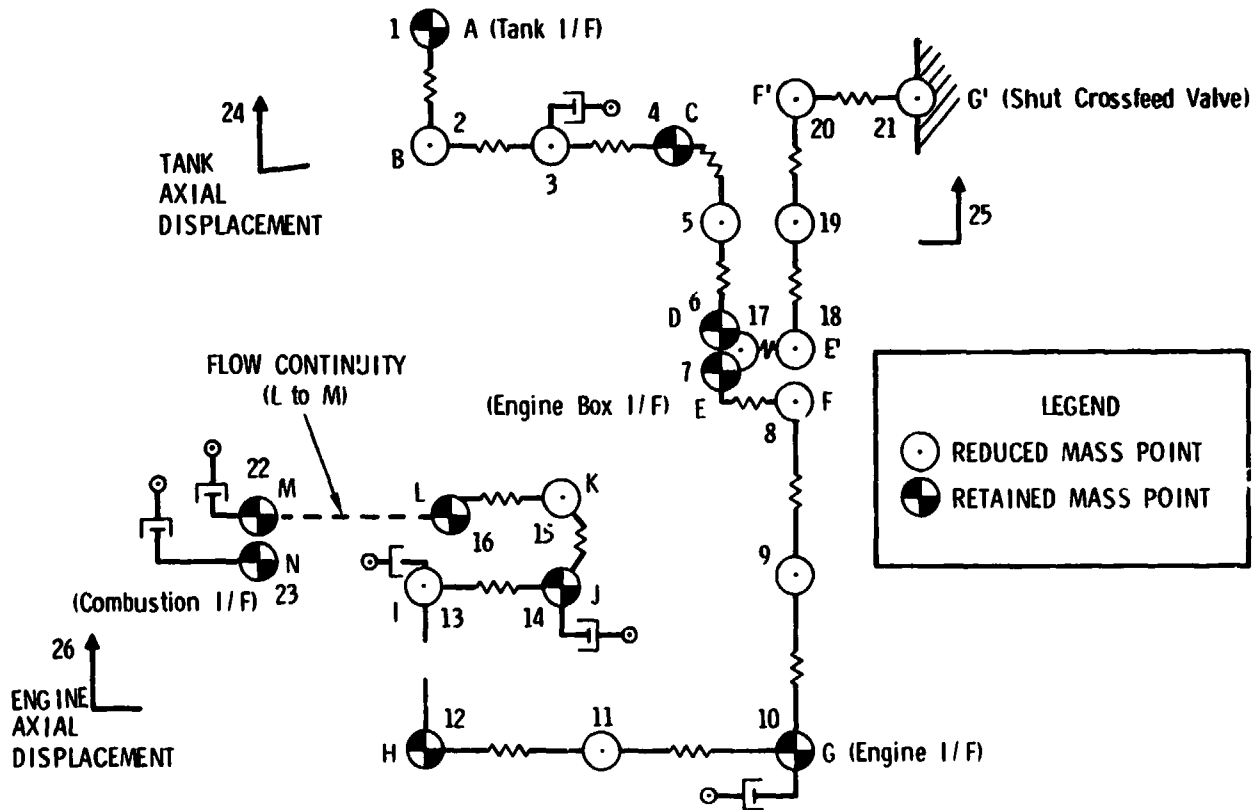
Figure 46.   OMS Oxidizer Circuit Model Schematic

The feedsystem models for fuel and oxidizer circuits are assembled by a multistep process. Utilizing the fuel circuit (Figure 45) as an example, the assembly steps consist of:

a. Formation of simple node chains, namely 1-6, 7-16, 17-21 and 22-25 with 26-28 reserved for the line structural motions

b. Application of continuity constraints and support constraints, namely

$$\Theta_{17} = \Theta_6 - \Theta_7$$

$$\Theta_{22} = \Theta_{16} \tag{27}$$

$$\Theta_{21} = 0$$

c. Incorporation of Guyan reduction (Ref. 18) retaining DOF 1, 4, 6, 7, 9, 11, 16, 23-25, 26-28, as indicated in Figure 45.

All constraint and reduction transformations are applied in a symmetric manner as for typical structural dynamic models.

In the present application, the generalized mass matrix partition M_{rig} corresponding to the dynamics of the line with frozen fluid mass is neglected implying that it is accounted for in the pod structural model. The load distribution vectors Γ_t and Γ_c consist of single unit entries at rows corresponding to the tank and chamber interfaces, respectively. The load vector F_s is comprised of the appropriate structural interface reactions, such as F_{ef} and F_{tf} for the fuel circuit.

3.2.2 Combustion Dynamics

The well-known linear characterization of the relationship between chamber pressure and injector face propellant flow perturbations is of the form

$$(1 + \tau_r s)P_c = R_{cf} e^{-\tau_{df} s} \dot{\Theta}_{if} + R_{co} e^{-\tau_{do} s} \dot{\Theta}_{io} \tag{28}$$

with s representing the Laplace variable. The chamber resistance coefficients, R_{cf} and R_{co}, are estimated on the basis of steady engine performance

data (Ref. 2), which in the present case was obtained from actual engine development tests. The chamber residence time τ_r is calculated from chamber geometry data and the combustion time delays, τ_{df} and τ_{do}, have been provided by Aerojet Liquid Rocket Company. Our studies showed that the amplification and phase lead due to the Klystron or clumping effect (Ref. 19) was negligible and it was thus ignored. The values of all combustion constants along with some basic performance data are presented in Table 4.

Since the present formulation, and the analysis approach discussed in the next section, require a set of first-order, real, constant-coefficient differential equations, an approximation of Eq. (28) has been derived   The approximation, first used by us during Delta Stage II pogo studies in 1975, employs fourth-order Padè expansions (Ref. 20) for the exponentials and a state variable transformation (Ref. 21). The resulting state equations are described in detail in Appendix D.

3.2.3   Propulsion System Modes and Frequency Response

The modal and frequency response characteristics of the propulsion system were studied prior to actual closed-loop stability calculations to obtain a basic understanding of structure/propulsion system interaction mechanisms and data for preliminary open-loop stability analysis. To this end, the assembled fuel and oxidizer circuit models with excitation at the structural interfaces, Eq. (26), were coupled with the combustion dynamics representation, Eq. (28).

$$(L) \left| \ddot{\theta} \right| + (R) \left| \dot{\theta} \right| + (K) \left| \theta \right| + (\Gamma_{se}) \left| \begin{matrix} P_c \\ X_c \end{matrix} \right| = - (\rho h) \left| \ddot{X}_s \right| \qquad (29a)$$

$$\left| \begin{matrix} \dot{P}_c \\ \dot{X}_c \end{matrix} \right| = (K_c) \left| \begin{matrix} P_c \\ X_c \end{matrix} \right| + (\Gamma_{es}) \left| \dot{\theta} \right| \qquad (29b)$$

The matrix Γ_{se} consists of Γ_c of Eq. (26) augmented by zero columns corresponding to the engine state variables X_c which are $X_1, \ldots, X_8$ of Eq. (D-13).

Table 4. Engine Dynamic Combustion Parameters

Steady State

$$\text{Thrust} = 27 \text{ kN } (6000 \text{ lb}_f)$$

$$P_c = 0.86 \text{ MPa } (125 \text{ psia})$$

$$\dot{W}_{df} = 3.28 \text{ kg/sec } (7.22 \text{ lb/sec})$$

$$\dot{W}_{do} = 5.40 \text{ kg/sec } (11.91 \text{ lb/sec})$$

$$A_t C_f = 310 \text{ cm}^2 \ (48 \text{ in.}^2)$$

$$MR = 1.65$$

$$I_{sp} = 3070 \text{ N-s/kg } (313 \text{ sec})$$

$$\frac{C^*}{A_t g} = 1.01 \text{ sec/cm}^2 \ (6.53 \text{ sec/in.}^2)$$

Perturbations

$$\frac{d I_{sp}}{d MR} = 142 \text{ N-s/kg } (14.5 \text{ sec})$$

$$\frac{C_f^*}{A_t g} = \frac{R_{cf}}{\rho_f g} = 0.8 \text{ sec/cm}^2 \ (5.21 \text{ sec/in.}^2)$$

$$\frac{C_o^*}{A_t g} = \frac{R_{co}}{\rho_o g} = 1.14 \text{ sec/cm}^2 \ (7.3 \text{ sec/in.}^2)$$

Time Constants

Residence Lag $= 0.88$ ms

Fuel Delay $\doteq 0.6$ ms

Ox Delay $\doteq 1.0$ ms

Transformation to a convenient set of first-order dynamic equations is effected by definition of the flow velocity variables

$$\left| V \right| = \left| \dot{\Theta} \right| \tag{30}$$

yielding after some manipulation

$$
\left\{\begin{array}{c} \dot{V} \\ \hline \dot{\Theta} \\ \hline \dot{P}_c \\ \dot{X}_c \end{array}\right\} + \left(\begin{array}{c|c|c} L^{-1}R & L^{-1}K & -L^{-1}\Gamma_{se} \\ \hline -I & 0 & 0 \\ \hline -\Gamma_{es} & 0 & -K_c \end{array}\right) \left\{\begin{array}{c} V \\ \hline \Theta \\ \hline P_c \\ X_c \end{array}\right\} = \left(\begin{array}{c} -L^{-1}(\rho h) \\ \hline 0 \\ \hline 0 \end{array}\right) \left| \ddot{X}_s \right| \tag{31}
$$

The complex propulsion system modes exhibit coupled dynamics of the fuel and oxidizer circ due to bipropellant combustion dynamics. For basic understanding of the dynamics of the individual propellant circuits it is necessary to first examine the system modes for fuel and oxidizer circuits, separately, in the absence of combustion (that is, $P_c = 0$ with the lowest row block partition Eq. (31) removed). The fundamental complex fuel and oxidizer modes (predominantly real) are illustrated in Figures 47 and 48 In both cases the modes indicate a major contribution of the side branches to the dynamic behavior. The lower propulsion system modes and eigenvalues with combustion dynamics included are summarized in Table 5 along with the corresponding modes without combustion. Although the fuel and oxidizer circuits are somewhat coupled in these modes, the complex eigenvalues and mode shapes are not greatly affected by combustion dynamics. This insensitivity was due to the relatively low impedance associated with the combustion parameters; in particular, the chamber resistances are significantly lower than the propellant circuit flow resistances localized near the injector. The ratios are

$$R_{cf}/R_{fuel} \cong 0.20, \qquad R_{co}/R_{ox} \cong 0.56 \tag{32}$$
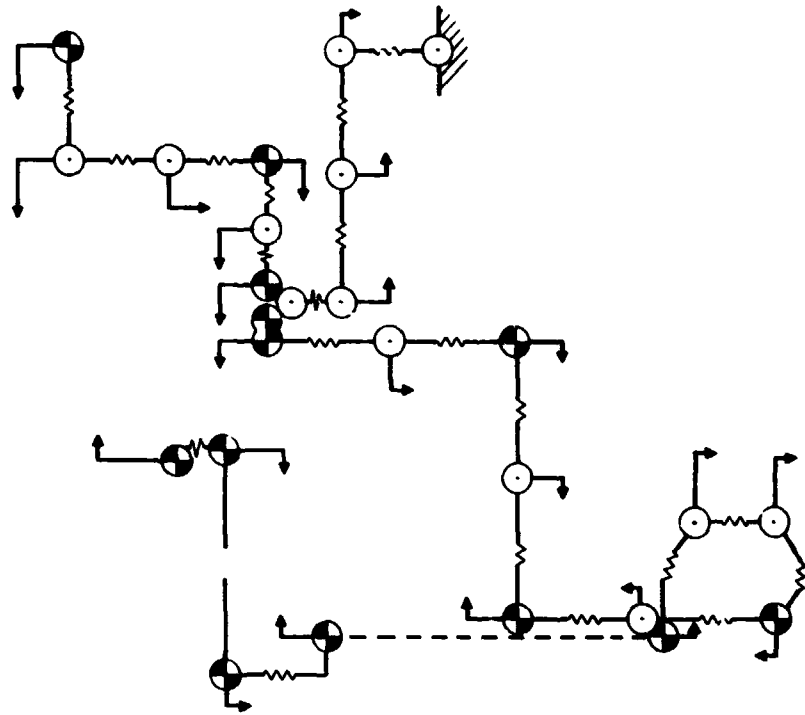
Figure 47. Fuel Circuit Fundamental Mode
Without Combustion ($\zeta = 0.098$,
$f = 78.1$ Hz)
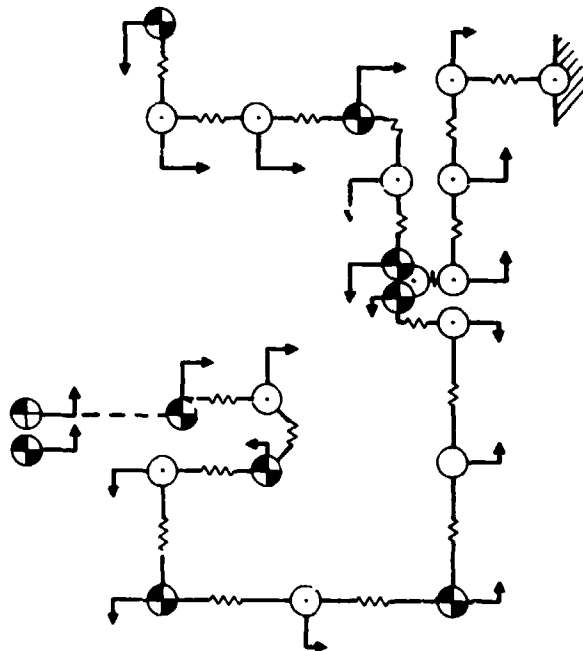
Figure 48. Oxidizer Circuit Fundamental Mode
Without Combustion ($\zeta = 0.084$,
$f = 65.2$ Hz)

Table 5. Summary of Lower Propulsion System Modes

Without Combustion (P_c = 0)		With Combustion [P_c using Eq. (28)]		
Eigenvalue	Mode	Eigenvalue	Mode	θ_{if}/θ_{io}
s = 0	Fuel rigid	s = 0	Rigid	0.99
s = 0	Ox rigid	s = 0	Rigid	-2.36
s = -78.95	Ox overdamped	s = -94.02	Overdamped	-1.47
s = -107.5	Fuel overdamped	s = -176.5	Overdamped	1.68
ζ = 0.084, f = 65.2 Hz	Ox fundamental	ζ = 0.101, f = 67.6 Hz	Ox fundamental	0.27, -130 deg
ζ = 0.009, f = 78.1 Hz	Fuel fundamental	ζ = 0.113, f = 79.6 Hz	Fuel fundamental	16.7, 19 deg
ζ = 0.114, f = 119.1 Hz	Ox second	ζ = 0.105, f = 125.9 Hz	Ox second	0.58, -132 deg
ζ = 0.077, f = 131.1 Hz	Fuel second	ζ = 0.092, f = 134.0 Hz	Fuel second	3.30, -25 deg

The frequency response of the propulsion system subjected to individual unit structural excitations, $\ddot{X}_s$, was calculated utilizing the complete set of propulsion system modes (by the method described in Appendix E). The chamber pressure response to fuel tank, oxidizer tank, and engine axial excitation are illustrated in Figures 49 through 51. All responses exhibit fairly flat gain variation below 65 Hz with phase in the range of -30 to -140 deg. The responses to tank acceleration are shown for tank propellant levels of zero and 76.2 cm (30 in.). The effect of tank bottom pressure is accounted for in the frequency response by augmenting the acceleration head terms with the appropriate tank liquid heights

$$h_{tf} = h_{to} = \mu \ell_t \tag{33}$$

noting Eq. (23). On the basis of the nearly constant difference between the responses with and without tank fluid, it is estimated that the effective upper line acceleration heads are approximately 71.1 cm (28 in.) for both the fuel and oxidizer lines ($h_{\ell f}$ and $h_{\ell o}$, respectively).

3.3   STABILITY ANALYSIS

The present stability analysis includes:

a.   An initial open-loop investigation for identification of potential destabilization mechanisms

b.   A closed-loop analysis illustrating the nominal stability associated with the engine localized 45-Hz structural mode

c.   Worst-case damping loss envelopes

All of the above employ nominal propulsion system parameters.

3.3.1   Open-Loop Stability Approximation

Approximate open-loop stability analysis provides basic understanding of the pogo feedback mechanism and the role of system parameters. In the present study, open-loop analysis is extensively used in nominal parameter and sensitivity calculations and in a preliminary worst-case investigation.
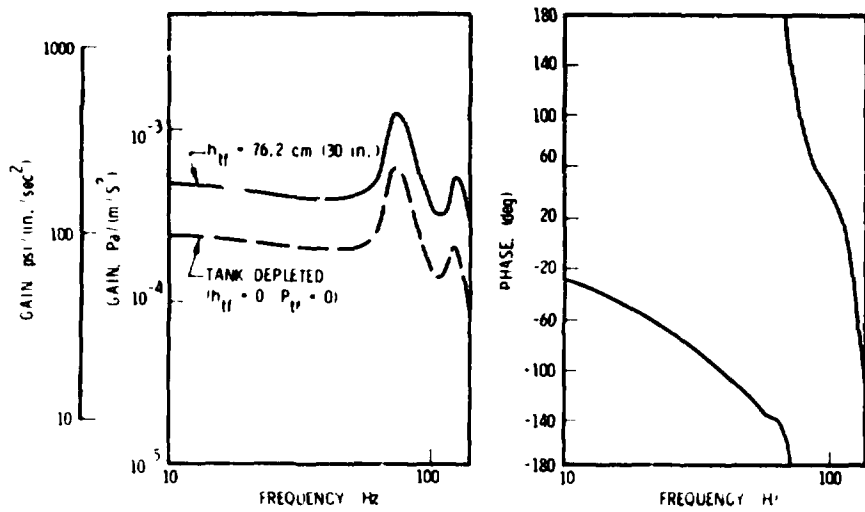
Figure 49. Chamber Pressure Response to
Fuel Tank Motion ($\partial P_c / \partial \ddot{X}_{tf}$)
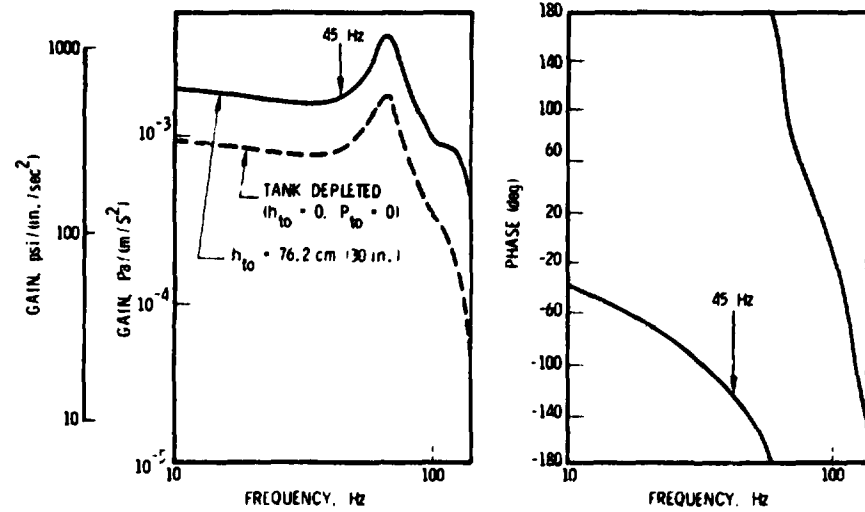
Figure 50. Chamber Pressure Response to Oxidizer
Tank Motion ($\partial P_c / \partial \ddot{X}_{to}$)
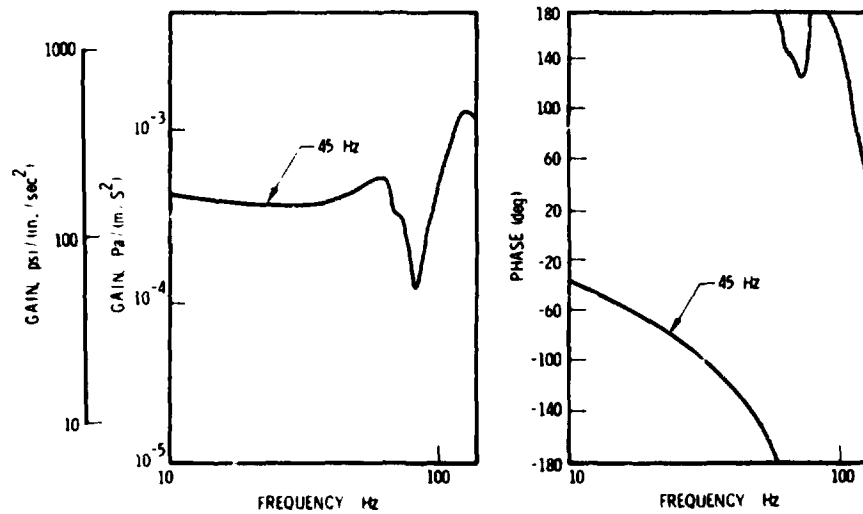
Figure 51. Chamber Pressure Response to Engine
Gimbal Motion ($\partial P_c / \partial \ddot{X}_e$)

The approximate equation for response of a single structural mode, if one ignores all interaction forces other than thrust perturbation, is

$$\ddot{X}_e + 2\zeta_o\omega_o\dot{X}_e + \omega_o^2 X_e = \frac{A_e}{M_\phi} P_c \tag{34}$$

with engine axial motion as the generalized displacement (mode normalized at X_e) and A_e representing the thrust coefficient given in Table 4. The total chamber pressure response due to structural mode excitation is

$$P_c = \left[\frac{\partial P_c}{\partial \ddot{X}_e} + \phi_{tf}\left(1 + \frac{\mu \ell_t}{h_{\ell f}}\right)\frac{\partial P_c}{\partial \ddot{X}_{tf}} + \phi_{to}\left(1 + \frac{\mu \ell_t}{h_{\ell o}}\right)\frac{\partial P_c}{\partial \ddot{X}_{to}}\right]\ddot{X}_e \tag{35}$$

for which the component response functions are presented in Figures 49 through 51 (for $h_{tf} = h_{to} = 0$). If Eq. (35) is substituted into Eq. (34) at the structural resonance $\omega = \omega_o$, a simplified estimate of closed-loop damping is obtained

$$\zeta_c = \zeta_o - \Delta\zeta \tag{36}$$

based on the open-loop damping loss

$$\Delta\zeta = \frac{A_e}{2M_\phi}\left[\left(\frac{\partial P_c}{\partial \ddot{X}_e}\right)^* + \left(1 + \frac{\mu \ell_t}{h_{\ell f}}\right)\left(\frac{\partial P_c}{\partial \ddot{X}_{tf}}\right)^* + \left(1 + \frac{\mu \ell_t}{h_{\ell o}}\right)\left(\frac{\partial P_c}{\partial \ddot{X}_{to}}\right)^*\right]$$

$$\tag{37}$$

with the asterisk (*) denoting the response component at -90 deg phase. As mentioned earlier, it should be noted that the above open-loop stability approximation accounts for the thrust feedback interaction loads applied to the structure alone. Reaction forces associated with open tank bottoms and feedsystem pressures at bends are ignored. A consistent account of all interactions inherent in the component models is realized in the closed-loop procedure outlined below and discussed in Appendix D.

3.3.2 Closed-Loop Formulation

The closed-loop stability equations are constructed in a manner similar to the response equations of Section 3.2.3. The procedure consists of (1) assembly of the combined OMS pod/feedsystem hydroelastic equations and (2) assembly of the first-order coupled hydroelastic/combustion dynamic equations.

Assembly of the OMS pod/feedsystem hydroelastic equations is accomplished by enforcement of modal and boundary constraints on the OMS pod structure, Eq. (24), and on the feedsystem, Eq. (26). Details of the constraint matrix as formed in the computer calculations are presented in Appendix D. Upon application of the constraints to Eqs. (24) and (26) in a symmetric manner, the following consistent set of hydroelastic equations is obtained:

$$
\begin{pmatrix} L & (\rho h)'\psi \\ \psi^T (\rho h)'^T & M_\phi \end{pmatrix} \begin{Bmatrix} \ddot{\theta} \\ \ddot{X}_e \end{Bmatrix} + \begin{pmatrix} R & \\ & 2\zeta_0 \omega_0 M_\phi \end{pmatrix} \begin{Bmatrix} \dot{\theta} \\ \dot{X}_e \end{Bmatrix}
$$
$$
+ \begin{pmatrix} K & \\ & \omega_0^2 M_\phi \end{pmatrix} \begin{Bmatrix} \theta \\ X_e \end{Bmatrix} = \begin{pmatrix} \Gamma'_{se} \end{pmatrix} \begin{Bmatrix} P_c \\ X_c \end{Bmatrix} \tag{38}
$$

The mass coupling partition $(\rho h)'\psi$ represents the generalized acceleration head contributions due to feedsystem and tank heads combined, and the generalized thrust chamber loading matrix Γ'_{se} consists of non-zero entries

Γ'_{se} (11, 1) = -1. (chamber pressure to fuel circuit)

Γ'_{se} (20, 1) = -1. (chamber pressure to oxidizer circuit) (39)

Γ'_{se} (21, 1) = A_e (thrust)

Due to the consistency of constraints, all other explicit interface reaction terms do not appear in Eq. (38) (i.e., equal and opposite interactions

The closed-loop stability equations consisting of Eqs. (38) and (29b) (with Γ_{es} slightly modified due to one additional variable) are finally constructed by introduction of the generalized velocity vector

$$\left|v\right| = \left|\dot{q}\right| = \left\{\begin{array}{c} \dot{\Theta} \\ \dot{X}_e \end{array}\right\} \tag{40}$$

and some matrix manipulation resulting in

$$\left\{\begin{array}{c} \dot{v} \\ \hline \dot{q} \\ \hline \dot{P}_c \\ \hline \dot{X}_c \end{array}\right\} = \left(\begin{array}{c|c|c} -M_q^{-1}R_q & -M_q^{-1}K_q & M_q^{-1}\Gamma'_{se} \\ \hline I & 0 & 0 \\ \hline & & \\ \Gamma'_{es} & 0 & K_c \end{array}\right) \left\{\begin{array}{c} v \\ \hline q \\ \hline P_c \\ \hline X_c \end{array}\right\} \tag{41}$$

with M_q, R_q and K_q representing the generalized mass, damping and stiffness matrices defined in Eq. (38). The closed-loop matrix equation set, Eq. (41), is in the form of a standard algebraic eigenvalue problem and the solution yields the complete set of complex eigenvalues and eigenvectors.

3.3.3 Nominal Stability Analysis Results

Open-loop stability estimates were first calculated for the primary OMS pod axial mode (with RCS 1 percent full) and the engine axial gimbal mode (with RCS 50 percent full) versus OMS tank fill condition. The basic data for these calculations consists of modal data presented in Table C-3 (along with a fraction of critical viscous damping $\zeta_o = 0.01$) and the propulsion system response data presented in Figures 49 through 51. The resulting nominal stability versus OMS tank fill level, illustrated in Figure 52, indicates a nearly invariant engine gimbal mode instability due to the localized nature of the 45 Hz mode and a destabilizing trend in the primary axial mode with a minimum 8.9 dB margin near the 10 percent OMS fill level. The dB margin is called the damping gain margin and defined in Eq. (3) of Ref. 5.

$$dB \text{ margin} = 20 \log_{10} \frac{\zeta_o}{\zeta_o - \zeta_c} \qquad (\zeta_c < \zeta_o) \tag{42}$$
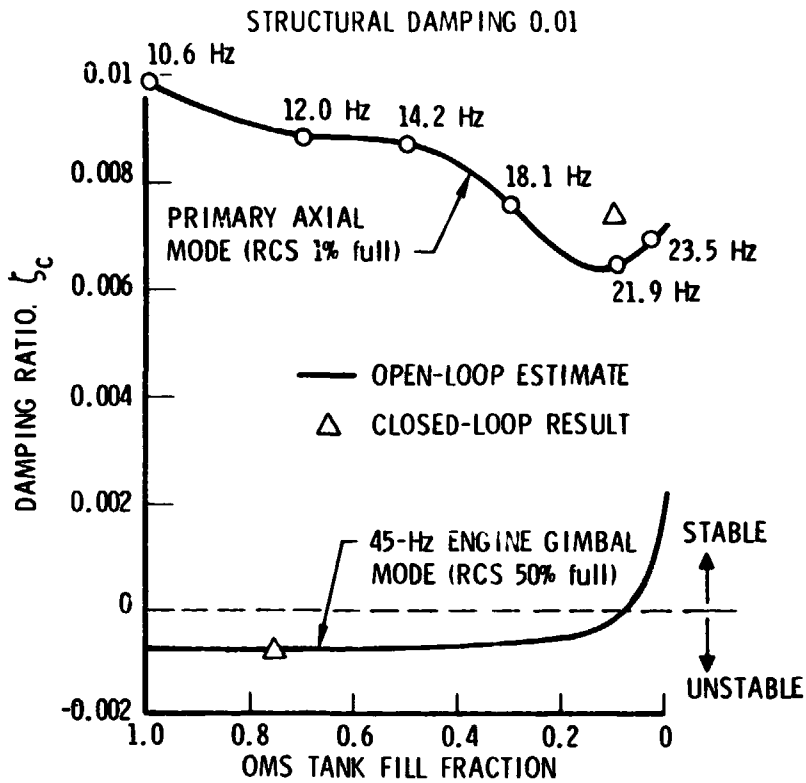
Figure 52. Nominal Stability vs. OMS Tank Fill Level
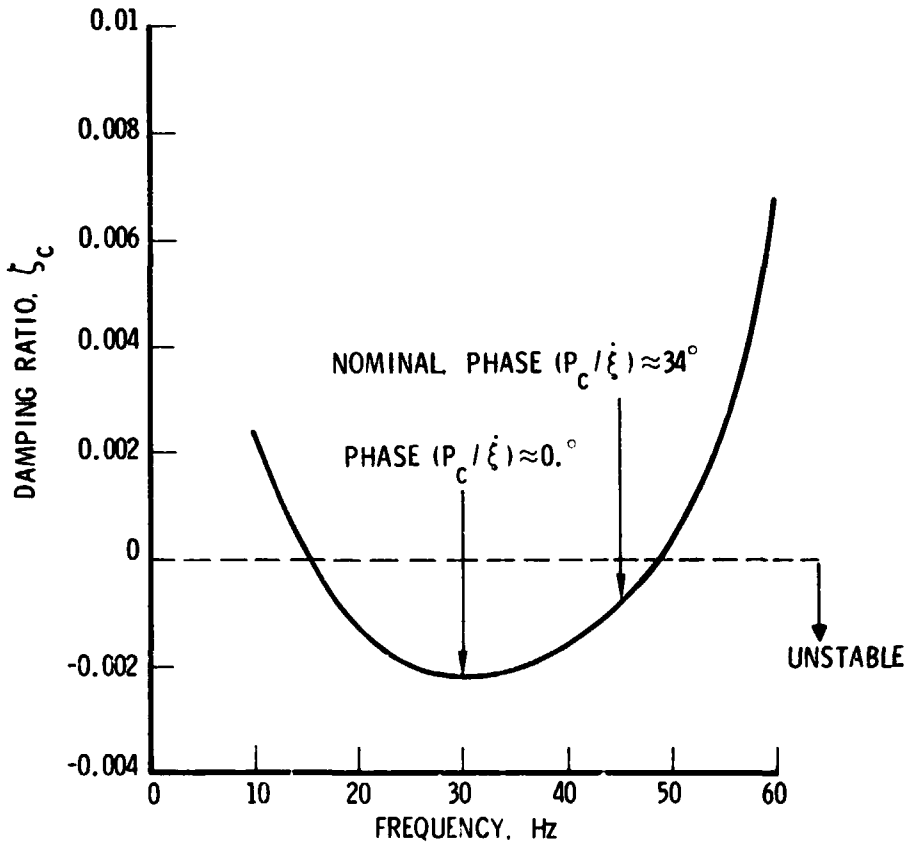
Figure 53. Stability Sensitivity of Engine Gimbal Mode to Frequency Variation

In the engine gimbal mode, the thrust feedback primarily due to $\partial P_c / \partial \ddot{X}_e$, has a nominal phase of 214 deg lagging the stabilizing structural mode damping force, $2\zeta_o M_\phi \Phi_e$. The stability of the primary axial mode is degraded by major components of all three chamber pressure response functions which produce a net feedback opposing the structural mode damping force. An instability is not realized due to the low structural gain associated with this mode.

Limited closed-loop stability calculations were performed for the primary axial and engine gimbal modes, each at particular tank fill levels. The closed-loop damping associated with the engine gimbal mode (Figure 52) is extremely close to the open-loop estimate since interaction forces neglected in the open-loop approximation are insignificant. On the other hand, in the primary axial mode, the open- and closed-loop damping estimates differ somewhat due to neglected interaction forces.

A detailed look at the closed-loop eigenvector (and similarly the propulsion system frequency response) indicates that the 45-Hz instability and the degraded stability of the primary axial mode are bipropellant phenomena. In particular, for the 45-Hz mode, the fuel to oxidizer injector flow ratio $(\Theta_{If} / \Theta_{Io})$ is about 0.9. For the primary axial mode (10 percent OMS fill, 1 percent RCS fill), the flow ratio is about 0.8. This observation suggests the necessity of accumulators for both fuel and oxidizer circuits for adequate suppression.

3.3.4   Variation of Engine Gimbal Mode Frequency

The sensitivity of the engine gimbal mode to modal frequency variation was examined on the basis of the open-loop estimate. Modal parameters associated with the OMS tank 75 percent fill level and RCS 50 percent fill level were used. The results presented in Figure 53 illustrate that instability may occur over a wide range of gimbal frequency (15-50 Hz). Moreover, for the present nominal set of propulsion system parameters, the system becomes phase stable as engine gimbal frequency approaches the fundamental oxidizer mode at 67.6 Hz. It should be emphasized that this higher frequency

trend does not necessarily suggest stiffening of the gimbal structure for pogo alleviation. Variation of combustion time delays and/or propellant bulk moduli off the current preliminary values can effect unfavorable phase shifts.

3.3.5 Damping Loss Envelopes

In view of the preliminary nature of the OMS pogo model, conservative worst-case damping loss envelopes are useful for definition of suppressor requirements. On the basis of the conservative upper bounds on modal gain, Eq. (22), and the representative upper-bound (phase varied) propulsion system response functions, an open-loop based damping loss envelope is defined as

$$\Delta \zeta(\phi_{tf}, \phi_{to}, \mu) \leq$$

$$\frac{\dfrac{A_e}{2} \left\{ \left| \dfrac{\partial P_c}{\partial \ddot{X}_e} \right|_{max} + |\phi_{tf}| \left(1 + \dfrac{\mu \ell_t}{h_{\ell f}}\right) \left| \dfrac{\partial P_c}{\partial \ddot{X}_{tf}} \right|_{max} + |\phi_{to}| \left(1 + \dfrac{\mu \ell_t}{h_{\ell o}}\right) \left| \dfrac{\partial P_c}{\partial \ddot{X}_{to}} \right|_{max} \right\}}{M_e + \phi_{tf}^2 \left(M_{tf_s} + \mu M_{tf_p}\right) + \phi_{to}^2 \left(M_{to_s} + \mu M_{to_p}\right)} \tag{43}$$

The chosen upper-bound propulsion system response values, valid in the 15-60 Hz frequency range, are

$$\left| \frac{\partial P_c}{\partial \ddot{X}_e} \right|_{max} = 110 \text{ Pa/(m/s}^2) \text{ or } 4 \times 10^{-4} \text{ psi/(in./sec}^2)$$

$$\left| \frac{\partial P_c}{\partial \ddot{X}_{tf}} \right|_{max} = 54 \text{ Pa/(m/s}^2) \text{ or } 2 \times 10^{-4} \text{ psi/(in./sec}^2) \tag{44}$$

$$\left| \frac{\partial P_c}{\partial \ddot{X}_{to}} \right|_{max} = 220 \text{ Pa/(m/s}^2) \text{ or } 8 \times 10^{-4} \text{ psi/(in./sec}^2)$$

Further simplification of the damping loss envelope expression is accomplished by separation into somewhat more conservative individual components due to engine motion, fuel tank motion and oxidizer tank motion, respectively, i.e.

$$\Delta\zeta_e \leq \left(\frac{A_e}{2}\right) \frac{\left|\dfrac{\partial P_c}{\partial\ddot{X}_e}\right|_{max}}{M_e + \phi_{tf}^2\left(M_{tf_s} + \mu M_{tf_p}\right)} \tag{45a}$$

$$\Delta\zeta_{tf} \leq \left(\frac{A_e}{2}\right) \frac{\left|\phi_{tf}\right|\left(1 + \dfrac{\mu\ell_t}{h_{\ell f}}\right)\left|\dfrac{\partial P_c}{\partial\ddot{X}_{tf}}\right|_{max}}{M_e + \phi_{tf}^2\left(M_{tf_s} + \mu M_{tf_p}\right)} \tag{45b}$$

$$\Delta\zeta_{to} \leq \left(\frac{A_e}{2}\right) \frac{\left|\phi_{to}\right|\left(1 + \dfrac{\mu\ell_t}{h_{\ell o}}\right)\left|\dfrac{\partial P_c}{\partial\ddot{X}_{to}}\right|_{max}}{M_e + \phi_{to}^2\left(M_{to_s} + \mu M_{to_p}\right)} \tag{45c}$$

In the case of damping loss due to engine motion, a reasonable lower-bound modal mass was chosen to include fuel tank inertia only; it should be noted that the fuel tank is always lighter than the oxidizer tank.

Envelopes of the individual damping loss components are presented in Figures 54 through 56 as functions of modal tank motion with OMS tank fill condition as a parameter. The damping loss due to engine motion, $\Delta\zeta_e$, decreases with increasing tank motion and fill level as expected. The damping ratio losses due to tank motion, $\Delta\zeta_{tf}$ and $\Delta\zeta_{to}$, increase proportional to ϕ_t (tank modal amplitude) for low values of ϕ_t and asymptotically decrease inversely proportional to ϕ_t for large values of ϕ_t. The magnitude of $\Delta\zeta_{to}$ is
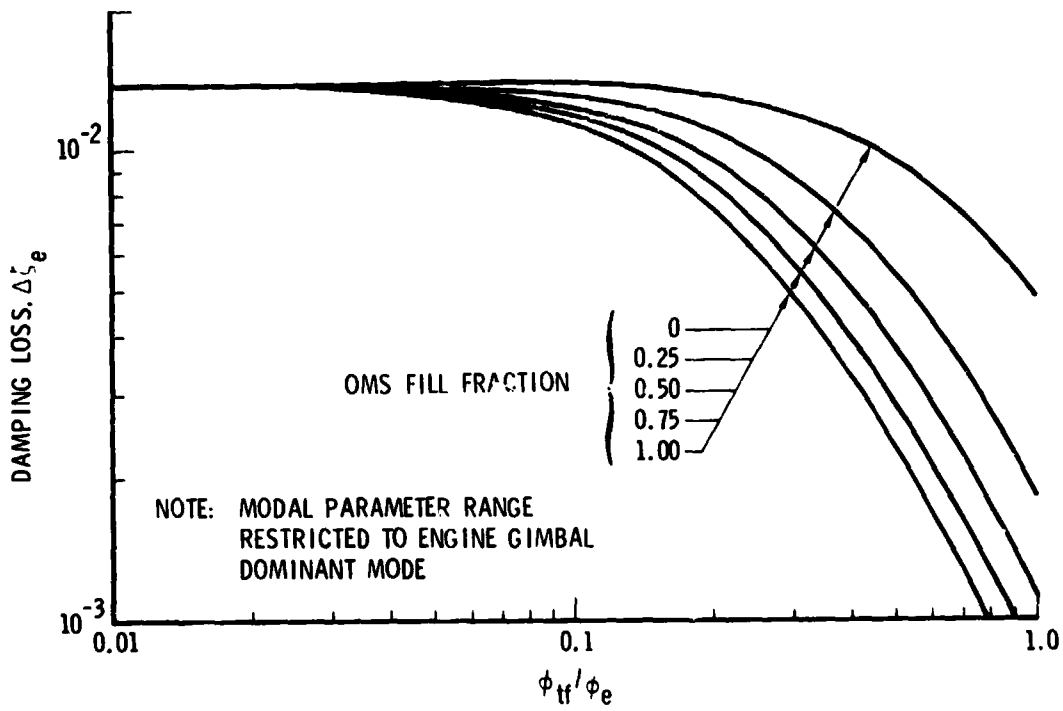
Figure 54. Envelope of Damping Loss due to Engine Gimbal
Motion vs. Tank Modal Amplitude
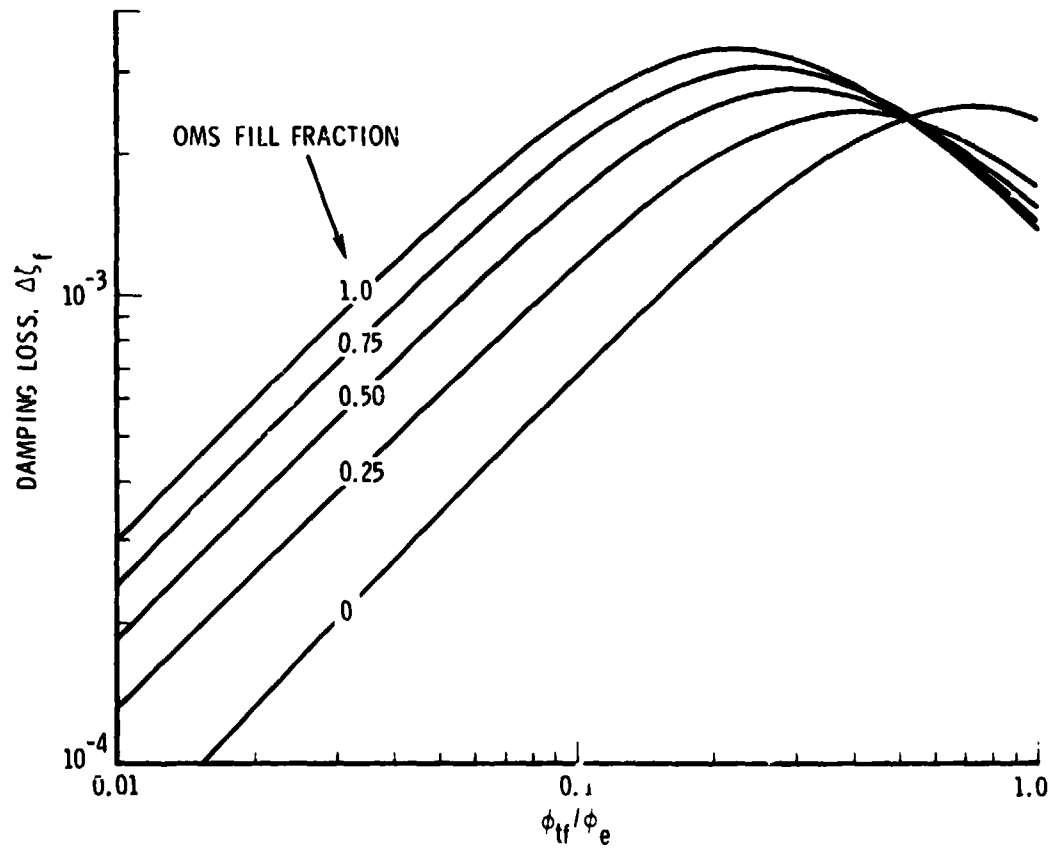
Figure 55. Envelope of Damping Loss due to Fuel Tank
Motion vs. Tank Modal Amplitude

greater than $\Delta\zeta_{tf}$ primarily due to the higher density of the oxidizer which manifests itself in propulsion system response [note Eq. (44)]. The damping loss envelope components generally indicate that the major contributors to potential instabilities are associated with engine gimbal motion and oxidizer tank motion.

Envelopes of total damping loss consisting of the sum of the components $\Delta\zeta_e$, $\Delta\zeta_{tf}$ and $\Delta\zeta_{to}$ are presented in Figure 57 for various OMS fill fractions, indicating the potential for serious pogo destabilization over a wide range of model parameters. The initiation of roll off in damping loss with increasing tank modal amplitude depends on the OMS tank fill level. Near tank depletion, serious destabilization is possible in tank dominated OMS pod modes $(\phi_{to}/\phi_e > 1)$. The envelopes suggest that pogo suppression may be required for pod modes other than the localized engine gimbal mode.

3.4   PRELIMINARY SUPPRESSOR STUDY

The nominal and dispersed parameter stability results suggest that modification of both propellant circuits may be necessary due to the bipropellant nature of the destabilizing system action (Section 3.3.3). Due to the potential for strong destabilization over large variation of pod structural mode shapes (Section 3.3.5), a structural modification does not now appear to be as potentially effective as an accumulator modification in view of the large uncertainties present in the structural modes.

A suppressor configuration consisting of 82 cm^3 (5 in.^{3}) compliant accumulators (i.e., negligible inertance) at the fuel and oxidizer engine interfaces [corresponding to the contractual interface between Aerojet Liquid Rocket Company (ALRC) and McDonnell Douglas Astronautics Company (MDAC)] was chosen for preliminary evaluation. Fuel and oxidizer circuit fundamental modes reduced to 22.9 and 19.4 Hz, respectively, when suppressors were incorporated in the math model while the higher mode frequencies remained above 90 Hz. The calculated effect on the propulsion system dynamics was favorable above 20 Hz. Chamber pressure response functions, altered by incorporation of accumulators, are illustrated in Figures 58 and 59 along with the corresponding response functions without accumulators.

3-27
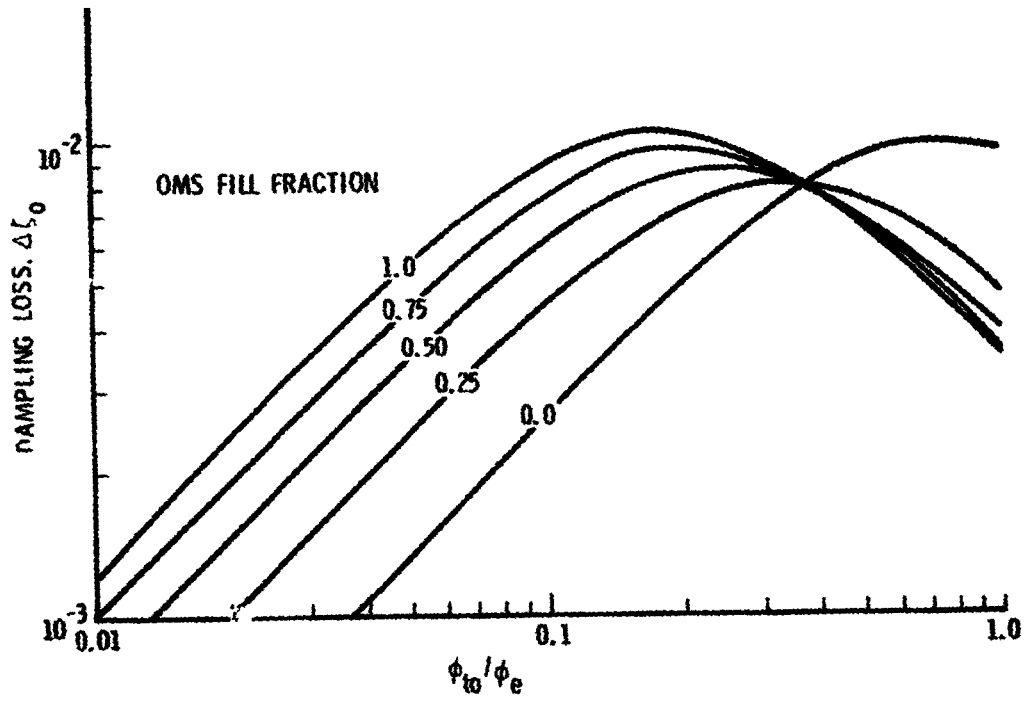
Figure 56. Envelope of Damping Loss due to Oxidizer Tank
Motion vs. Tank Modal Amplitude
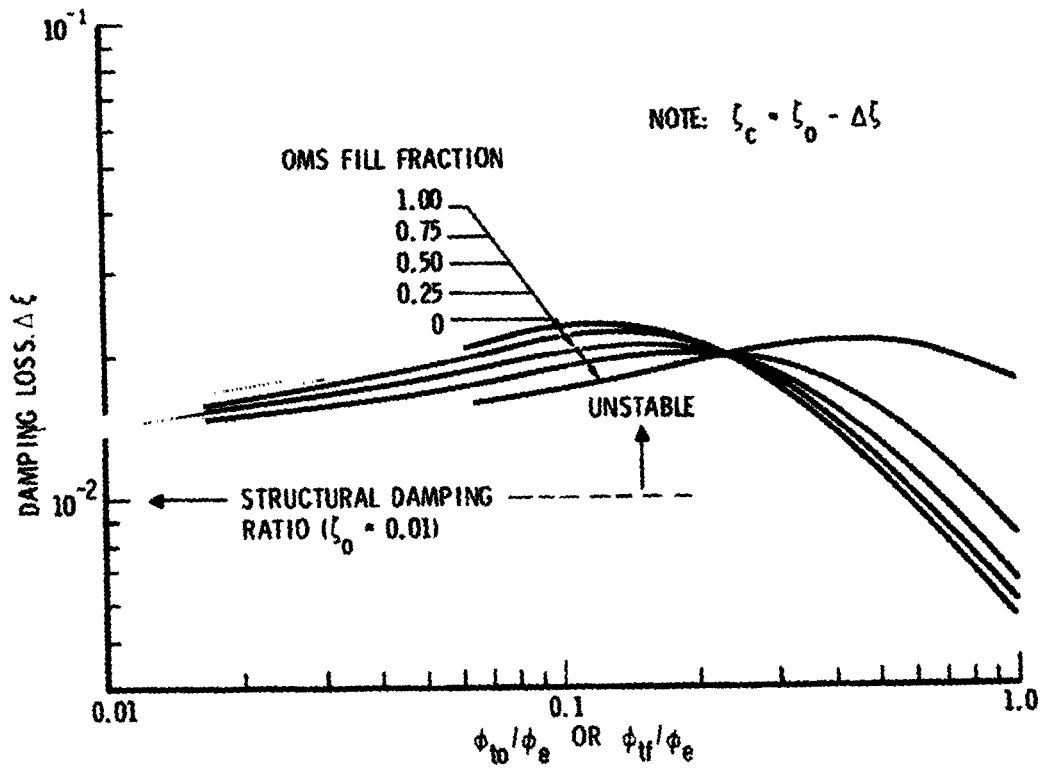
Figure 57. Envelope of Total Damping Loss vs. Tank
Modal Amplitude
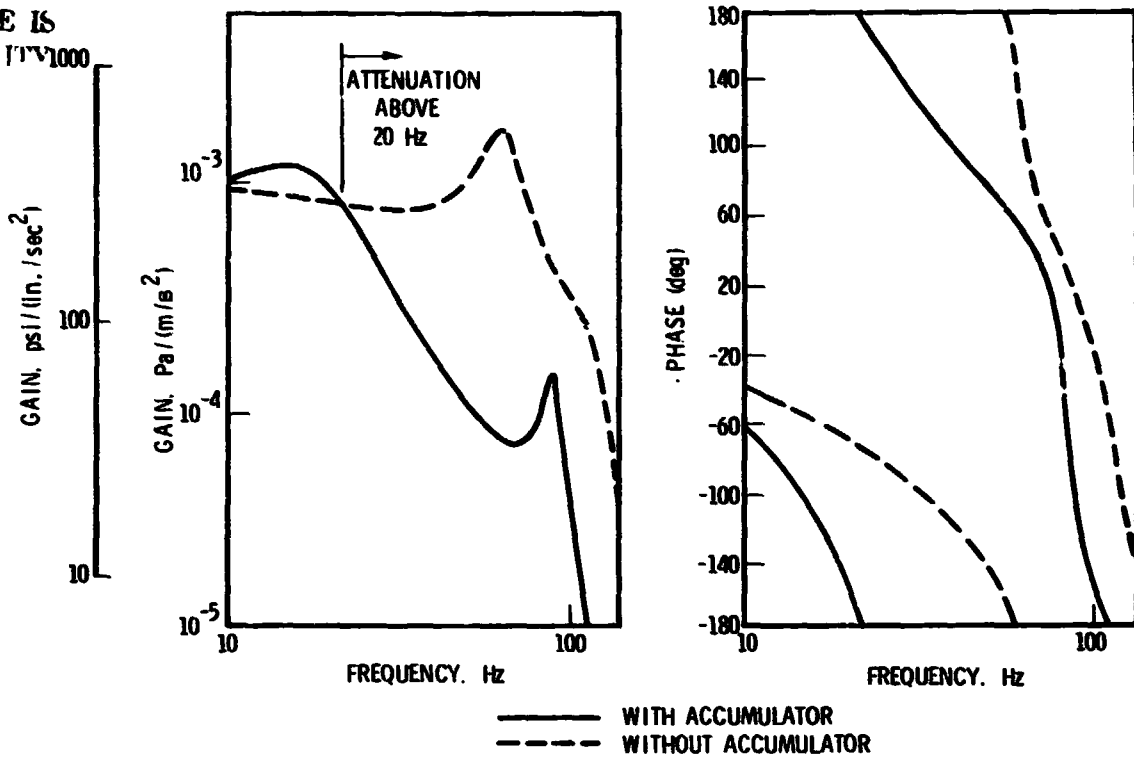
Figure 58. Effect of 82 cm^3 (5 in.^{3}) Accumulator on $\partial P_c/\partial \ddot{X}_{to}$ ($h_{to} = 0$)
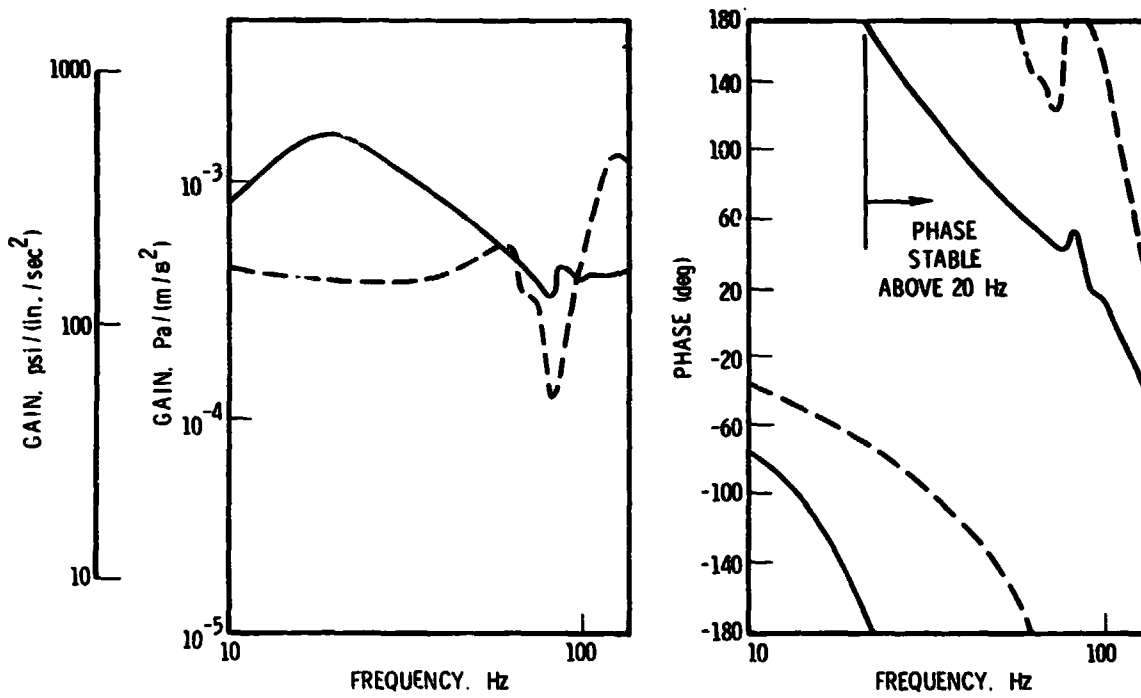
Figure 59. Effect of 82 cm^3 (5 in.^{3}) Accumulator on $\partial P_c/\partial \ddot{X}_e$

3-29

Basically, the engine-excited response is phase stable above 20 Hz in spite of a general increase in magnitude, and the oxidizer tank-excited response is well attenuated above 20 Hz. The stability of the nominal primary axial mode is slightly degraded below 20 Hz (minimum 8.9 dB stability margin) and enhanced above 20 Hz, and the engine gimbal mode at 45 Hz is phase-stabilized due to the suppressors.

Damping loss envelopes have not been calculated for the OMS with accumulators. It is possible that significant destabilization may occur below 20 Hz. Evaluation of larger compliant accumulators, resistive accumulators, and tuned accumulators should be pursued in further studies. It is currently estimated that 330 cm^3 (20 $in.^3$) compliant accumulators will reduce the fundamental propulsion system modes to about 10 Hz and enhance stability in the 10-20 Hz range.

3.5   SUMMARY

A preliminary mathematical model describing OMS intra-pod structural/propulsion system dynamics has been developed and analyzed for evaluation of pogo destabilization tendencies. A strong destabilization occurred in the localized 45-Hz axial engine gimbal mode that persisted at most OMS tank fill levels and under wide variation of the gimbal mode frequency. For nominal parameters in the preliminary model, an instability occurred in this mode. Other potential destabilization tendencies were identified upon variation of pod structural mode shapes. Worst-case damping loss envelopes reveal the potential for serious destabilization in tank coupled modes over a wide range of tank interaction.

An initial investigation of small 82 cm^3 (5 $in.^3$) compliant accumulators located at the engine interface (i.e., the MDAC/ALRC interface) shows their benefit in suppressing the engine gimbal mode instability in the preliminary model. Degradation of stability at low frequencies (f < 20 Hz) is possible with such small accumulators and it may be necessary to increase their volume to about 330 cm^3 (20 $in.^3$).

The present work represents the first OMS pogo stabilit*r* investigation. Future studies should include evaluation of (1) other feedsystem configurations (pod crossfeed, PBK supply, RCS supply), (2) lateral structure/propulsion dynamics, (3) more extensive parameter sensitivity analysis, and (4) resistive and tuned accumulators. In addition, pertinent OMS structure and propulsion system testing should be defined for identification of system dynamic parameters.

4. ERRORS IN FREQUENCY RESPONSE MEASUREMENTS

Various hydraulic pulsing programs will be conducted to determine experimental frequency responses for identification of the linearized dynamics of propulsion system elements. These include the CTL-V program (LPOTP, interpump duct, accumulator), single engine tests, and the Main Propulsion Test (Sec. 4 of Ref. 11).

The measurement of frequency response for these tests is difficult. If the induced system responses are too low, the results will be inaccurate due to the high self noise of the test system from operation of turbomachines, thrust chambers, etc. If the induced system responses are too large, the results will be distorted by nonlinearities. In this section we estimate the random error in frequency response measurements due to system noise, and we consider other practical matters of significance to the accuracy of such measurements.

A schematic diagram for the problem at hand is shown in Figure 60. It depicts the use of an external excitation i(t) to produce the two system responses x(t) and y(t). As shown these responses are made up of system random self-noise contributions m(t) and n(t), in combination with the response signals u(t) and v(t) which are purely the result of the excitation i(t).
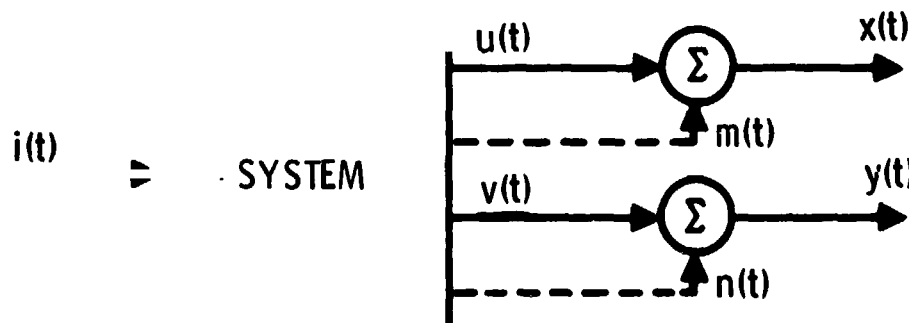
Figure 60. Schematic of Measurement Situation

We will be concerned with the use of sinusoidal excitation as a means to determine various frequency responses of the system. Reference is made frequently to Appendix F which was prepared by J.S. Bendat, a consultant for this investigation.

4.1   RANDOM ERROR IN DETERMINATION OF H_{xy}

As given in Eq. (F-13), the desired frequency response function $H_{xy}(f)$ can be estimated without bias by

$$\hat{H}_{xy}(f) = G_{iy}(f)\big/G_{ix}(f) \tag{46}$$

where $G_{ix}(f)$ and $G_{iy}(f)$ are cross-spectral density functions for the subscripted signals. We define the normalized mean-square error for the magnitude of $\hat{H}_{xy}(f)$

$$\epsilon^2(f) = E\left(\left|\hat{H}_{xy}(f)\right| - \left|H_{xy}(f)\right|\right)^2\big/\left|H_{xy}(f)\right|^2 \tag{47}$$

Assuming Gaussian statistics, the fractional error in $\left|\hat{H}_{xy}(f)\right|$ will be less than $\epsilon(f)$ with 68 percent probability, and less than $2\epsilon(f)$ with 95 percent probability. For the case of small errors and uncorrelated noise signals, the result is

$$\epsilon^2(f) \approx a_x^2(f) + a_y^2(f) \qquad (\epsilon^2 \ll 1) \tag{48}$$

and in the worst case with correlated noise signals, the result is

$$\epsilon^2(f) \approx [a_x(f) + a_y(f)]^2 \qquad (\epsilon^2 \ll 1) \tag{49}$$

where $a_x^2(f) = G_{mm}(f)\big/u_o^2(f)T(f)$ and $a_y^2(f) = G_{nn}(f)\big/v_o^2(f)T(f)$. The sinusoidal signal amplitudes $u_o(f)$ and $v_o(f)$ are at the frequency f. The analysis time for the sinusoidal signal at the frequency f is $T(f)$. This result is comparable to Eq. (F-50) except in two respects:

a. The two signal/noise ratios are not equated here.

b. The estimate of $E[|G_{iz}|^2]$ in Eq. (F-16) is halved based on the heuristic argument that, since i(t) is deterministic, the mean-square error in $|G_{iz}|$ corresponds to that of the mean value of narrow-band noise.

Note that the rms error ϵ is independent of the bandwidth B_e of the spectral analysis. An estimate of the error, however, is implicitly dependent on B_e because of uncertainty in the estimates of the noise spectral densities G_{mm} and G_{nn}. Such uncertainty decreases with the $B_e T_{total}$ product [equivalently the number of average n_d; see Eq. (F-47)], where T_{total} is the total analysis time for the noise signals. This uncertainty is expected to be relatively small for the various pulsing test programs since $B_e T_{total}$ should be relatively large. For example, a practical case is $B_e = 0.5$ Hz and $T_{total} = 50$ s, yielding a 20 percent uncertainty in G_{mm} and G_{nn} and a consequent 14 percent uncertainty in ϵ.

Another implicit influence of the bandwidth B_e is the fact that the estimate $\hat{H}_{xy}(f)$ will be some average over the bandwidth B_e. Thus, the expected rate of change of $H_{xy}(f)$ with frequency should be considered in establishing the analysis bandwidth so as to avoid unacceptable smoothing. In the case of the measurement of the elements of the LPOTP transfer matrix (CTL-V testing), the resulting functions are quite slowly varying with frequency (see Figures 32 through 39) and a relatively wide analysis bandwidth is acceptable from this standpoint.

4.2 SWEEP TESTING

One way to perform a frequency response test is to continuously change or sweep the excitation through the frequency range of interest. Another approach is to perform the testing at discrete values of frequency, holding the signal for some specified duration at each frequency. The time $T(f)$ in the error expression of Eq. (48) is the time that the excitation is maintained at the frequency f. For the swept case, $T(f)$ is taken to be the time that the excitation lies within the analysis bandwidth B_e.

For a linear sweep (that is, a constant rate of change of frequency $\dot{f}_o$), we have[*]

$$T(f) = B_e(f)/\dot{f}_o \tag{50}$$

The number of cycles of excitation, $N_B(f)$, occurring within the analysis bandwidth $B_e(f)$

$$N_B(f) = fT(f) = fB_e(f)/\dot{f}_o \tag{51}$$

showing that, for constant bandwidth and sweep rate, the number of cycles is proportional to the frequency.

For a logarithmic sweep (that is, rate of frequency change proportional to the frequency), we have $\dot{f}$ in Hz/s given by

$$\dot{f} = (\log_e 2/60)R_{\log} f = 0.0116\ R_{\log} f \tag{52}$$

where $R_{\log}$ is the common expression of sweep rate in octaves per minute. Therefore, the analysis time in seconds is

$$T(f) \quad \sim \frac{0}{\log_e 2}\ \log_e \left(\frac{f+B_e(f)/2}{f-B_e(f)/2}\right)$$

$$\doteq 86.6\ B_e(f)/R_{\log} f \qquad (B_e^2/3f^2 \ll 1) \tag{53}$$

where f is the mid-frequency of the band $B_e(f)$. Moreover, the number of cycles of excitation within a bandwidth $B_e(f)$ is

$$N_B(f) \doteq 86.6\ B_e(f)/R_{\log} \qquad (B_e^2/3f^2 \ll 1) \tag{54}$$

---

[*]The frequency being varied linearly is the true instantaneous frequency, which is proportional to the time rate of change of excitation phase. Thus, if the linear frequency variation is $f_o + \dot{f}_o t$, the excitation must have the form $\sin 2\pi[f_o + (\dot{f}_o/2)t]t$.

Observe that, for a constant bandwidth, N_B is independent of frequency. For example, if B_e = 1 Hz and R_{log} = 3 oct/min; at f=2 Hz, the analysis time T is 14.4 sec; at f=40 Hz, T = 0.72 sec; in both cases the number of cycles N_B = 29.

4.3   ACCURACY OF SINUSOIDAL AMPLITUDE

It is clear that some minimum number of cycles N_B is required to obtain an accurate estimate of the sinusoidal amplitude of a signal. Use of straight integration to obtain the mean-square value of a sinusoid yields an upper bound on the normalized error of $1/4\pi N$, where N is the number of cycles analyzed. To assure a fractional error of no more than ϵ_o in the estimate of the ratio of the amplitudes of two sinusoidal signals, the requirement on N is

$$N \geq 1/4\pi\epsilon_o \tag{55}$$

For example, for at most a 2 percent error in the estimated amplitude ratio, $N \geq 4$ cycles. Such a requirement may not prove to be very constraining for practical testing, but it should be kept in mind.

4.4   PLANNING A TEST

Given estimates of the noise spectra (G_{mm} and G_{nn}) based upon prior noise measurements and a desired maximum rms error ϵ_m for the determination of $|H_{xy}|$, we set the conditions [based upon Eq. (48) assuming uncorrelated noise]

$$a_x^2(f) \text{ and } a_y^2(f) \leq \epsilon_m^2 \big/ 2 \tag{56}$$

These conditions translate into conditions upon the sinusoidal amplitudes and associated analysis time

$$u_o^2(f)T(f) \geq 2G_{mm}(f)\big/\epsilon_m^2, \qquad v_o^2(f)T(f) \geq 2G_{nn}(f)\big/\epsilon_m^2 \tag{57}$$

4-5

An example is now created to help crystallize the various error matters related to the planning of a test for accurate frequency response measurements. One system response x(t) is considered for this example. Suppose that x(t) is a pressure variable, and that G_{mm} = 1 psi^2/Hz and B_e = 1 Hz over a 2 to 40 Hz frequency range of interest. Suppose also that ϵ_m = 0.05 (maximum rms error is 5 percent). The condition in Eq. (57) yields

$$u_o^2(f)T(f) \geq 2(1)\big/(0.05)^2 = 800$$

Table 6 shows the combinations of amplitude and associated minimum analysis time in the first two columns. The next three columns show for the lowest frequency of 2Hz: N_B, the minimum number of cycles required within the bandwidth [from $N_B(f) = fT(f)$ in Eq. (51)]; $\dot{f}_o$, the maximum constant sweep rate [from Eq. (50)]; and R_{log}, the maximum logarithmic sweep rate [from Eq. (53)]. The right-most three columns contain the same information for the highest frequency of interest of 40 Hz.

Observe that a high-frequency, low-amplitude signal imposes a severe requirement for slowness of a logarithmic sweep. Note also that the low-frequency, high-amplitude condition yields a requirement for only four cycles within the bandwidth, which is approaching the limit of concern for the accuracy of the sinusoidal amplitude itself [see Eq. (55)].

In planning an actual test, the various limits should be calculated based upon the best available pretest information for all of the system variables to be used for frequency response determinations and over the entire frequency range of interest. This should be done for several values of rms error. The results can then be employed to develop a logical test plan, based upon reasoned engineering judgment of all of the factors influencing accuracy.

Table 6. Results for a Test Planning Example (ϵ_m = 0.05,
B_e = 1 Hz, G_{mm} = 1 psi^2/Hz)

Amplitude u_o psi	Analysis Time T sec ($\geq$)	f = 2 Hz			f = 40 Hz		
		N_B cycles ($\geq$)	$\dot{f}_o$ Hz/sec ($\leq$)	R_{log} oct/min ($\leq$)	N_B cycles ($\geq$)	$\dot{f}_o$ Hz/sec ($\leq$)	R_{log} oct/min ($\leq$)
20	2	4	0.5	21.7	80	0.5	1.1
10	8	16	0.13	5.4	320	0.13	0.27
5	32	64	0.03	1.4	1280	0.03	0.07

4.5   CONCLUSION AND RECOMMENDATION

An engineering basis has been laid for the advance planning and
evaluation of propulsion tests for frequency response determinations. It is
recommended that the results developed herein be applied to the planning of
the applicable Shuttle propulsion tests.

APPENDIX A

EQUATIONS FOR MPS STABILITY ANALYSIS

A.1 FLUID DYNAMIC EQUATIONS FOR PROPULSION SYSTEM

The fluid dynamic equations for the elements of the propulsion system model are given below.

First Feedline Segment:

$$P_2 + Z_1 Q_t = 0 \tag{A-1}$$

$$(1 + s Z_2 C_{10}) P_2 - P_4 - Z_2 Q_t = 0 \tag{A-2}$$

Downcomer Segment:

$$P_6 - a_{11} P_4 - a_{12} \left| Q_t - sC \quad P_2 - sC_{24} P_4 \right| = 0 \tag{A-3}$$

$$Q_s - a_{21} P_4 - a_{22} \left| Q_t - sC_{10} P_2 - sC_{24} P_4 \right| = 0 \tag{A-4}$$

Downcomer Corner to Manifold:

$$(1 + s Z_4 C_{11}) P_6 - P_8 - Z_4 Q_5 = 0 \tag{A-5}$$

$$(1 + s Z_5 C_{12}) P_8 - P_{10} - Z_5 \left| Q_5 - sC_{11} P_6 \right| = 0 \tag{A-6}$$

$$(1 + s Z_6 C_{13}) P_{10} - P_{12} - Z_6 \left| Q_5 - sC_{11} P_6 - sC_{12} P_8 \right| = 0 \tag{A-7}$$

Manifold Continuity:

$$Q_{14} + 2Q_{18} - Q_5 + s \left| C_{11} P_6 + C_{12} P_8 + C_{13} P_{10} \right| = 0 \tag{A-8}$$

Manifold to Upper Engine LPOTP:

$$(1 + sZ_7C_{14}) P_{12} - P_{14} - Z_7Q_{14} = 0 \qquad \text{(A-9)}$$

$$(1 + sZ_8C_{15}) P_{14} - P_{16} - Z_8 \left| Q_{14} - sC_{14}P_{12} \right| = 0 \qquad \text{(A-10)}$$

$$P_{16} - P_{17} - Z_9 \left| Q_{14} - sC_{14}P_{12} - sC_{15}P_{.4} \right| = 0 \qquad \text{(A-11)}$$

Manifold to Lower Engine LPOTP:

$$(1 + sZ_{10}C_{16}) P_{12} - P_{18} - Z_{10}Q_{18} = 0 \qquad \text{(A-12)}$$

$$(1 + sZ_{11}C_{17}) P_{18} - P_{20} - Z_{11} \left| Q_{18} - sC_{16}P_{12} \right| = 0 \qquad \text{(A-13)}$$

$$P_{20} - P_{21} - Z_{12} \left| Q_{18} - sC_{16}P_{12} - sC_{17}P_{13} \right| = 0 \qquad \text{(A-14)}$$

Upper Engine LPOTP:

$$Q_{40} + sC_{pl}P_{17} - Q_{14} + s \left| C_3P_{40} + C_{14}P_{12} + C_{15}P_{14} \right| = 0 \qquad \text{(A-15)}$$

$$P_{40} - (m_1 + 1) P_{17} + Z_{\ell p}Q_{40} = 0 \qquad \text{(A-16)}$$

Upper Engine Inter-Pump Duct:

$$(1 + sZ_{13}C_{18}) P_{40} - P_{41} - Z_{40}Q_{40} = 0 \qquad \text{(A-17)}$$

$$(1 + sZ_{14}C_{19}) P_{41} - P_{42} - Z_{41} \left| Q_{40} - sC_{18}P_{40} \right| = 0 \qquad \text{(A-18)}$$

$$(1 + sZ_{15}C_{20}) P_{42} - P_{43} - Z_{42} \left| Q_{40} - sC_{18}P_{40} - sC_{19}P_{41} \right| = 0$$
$$\text{(A-19)}$$

$$(1 + Z_{43}Y_a) P_{43} - P_{44} - Z_{43} \left| Q_{40} - sC_{18}P_{40} - sC_{19}P_{41} - sC_{20}P_{42} \right| = 0$$
$$\text{(A-20)}$$

Upper Engine HPOTP:

$$Q_{44} + sC_{p2}P_{44} - Q_{40} + Y_aP_{43} + s\left[C_{18}P_{40} + C_{19}P_{41} + C_{20}P_{42}\right] = 0$$

$$\text{(A-21)}$$

$$P_{45} - (m_2 + 1)P_{44} + Z_{hp}Q_{44} = 0 \qquad \text{(A-22)}$$

Upper Engine Injector and Chamber:

$$P_{45} - [R_c + Z_j]Q_{44} = 0 \qquad \text{(A-23)}$$

$$P_{c1} - R_cQ_{44} = 0 \qquad \text{(A-24)}$$

Lower Engine LPOTP:

$$Q_{50} + sC_{p1}P_{21} - Q_{18} + s\left[C_3P_{50} + C_{16}P_{12} + C_{17}P_{18}\right] = 0 \qquad \text{(A-25)}$$

$$P_{50} - (m_1 + 1)P_{21} + Z_{\ell p}Q_{50} = 0 \qquad \text{(A-26)}$$

Lower Engine Inter-Pump Duct:

$$(1 + sZ_{17}C_{21})P_{50} - P_{51} - Z_{50}Q_{50} = 0 \qquad \text{(A-27)}$$

$$(1 + sZ_{18}C_{22})P_{51} - P_{52} - Z_{51}\left[Q_{50} - sC_{21}P_{50}\right] = 0 \qquad \text{(A-28)}$$

$$(1 + sZ_{19}C_{23})P_{52} - P_{53} - Z_{52}\left[Q_{50} - sC_{21}P_{50} - sC_{22}P_{51}\right] = 0$$

$$\text{(A-29)}$$

$$\left[1 + Z_{53}Y_a\right]P_{53} - P_{54} - Z_{53}\left[Q_{50} - sC_{21}P_{50} - sC_{22}P_{51} - sC_{23}P_{52}\right] = 0$$

$$\text{(A-30)}$$

Upper Engine HPOTP:

$$Q_{54} + sC_{p2}P_{54} - Q_{50} + Y_aP_{53} + s\left|C_{21}P_{50} + C_{22}P_{51} + C_{23}P_{52}\right| = 0$$

$$\text{(A-31)}$$

$$P_{55} - (m_2 + 1)P_{54} + Z_{hp}Q_{54} = 0 \qquad \text{(A-32)}$$

Lower Engine Injector and Chamber:

$$P_{55} - [R_c + Z_j]Q_{54} = 0 \qquad \text{(A-33)}$$

$$P_{c2} - R_cQ_{54} = 0 \qquad \text{(A-34)}$$

where the P_m and Q_n denote the pressures and absolute flows at different stations in the propulsion system (see Figure A-1). The coefficients C_m denote the local compliance values that are employed to represent the effect of compressibility in related elements of the feedline; the locations of these compliances are shown in Figure A-2. The coefficients Z_m denote the impedance associated with the various sections of the feedline. This impedance is defined by

$$Z = Ls + R$$

where L, R denote the inertance and resistance associated with the line segment. The terms C_{p1}, C_{p2}, $(m_1 + 1)$, and $(m_2 + 1)$ are the pump inlet cavitation compliance and pump gain associated with the LPOTP and HPOTP, respectively; the coefficient R_c denotes the resistance of the thrust chamber. The characteristics of the accumulators are defined by

$$Y_a = \left(\frac{s}{L_a}\right)\left|s^2 + 2\zeta_a\omega_a s + \omega_a^2\right|^{-1} \qquad \text{(A-35)}$$
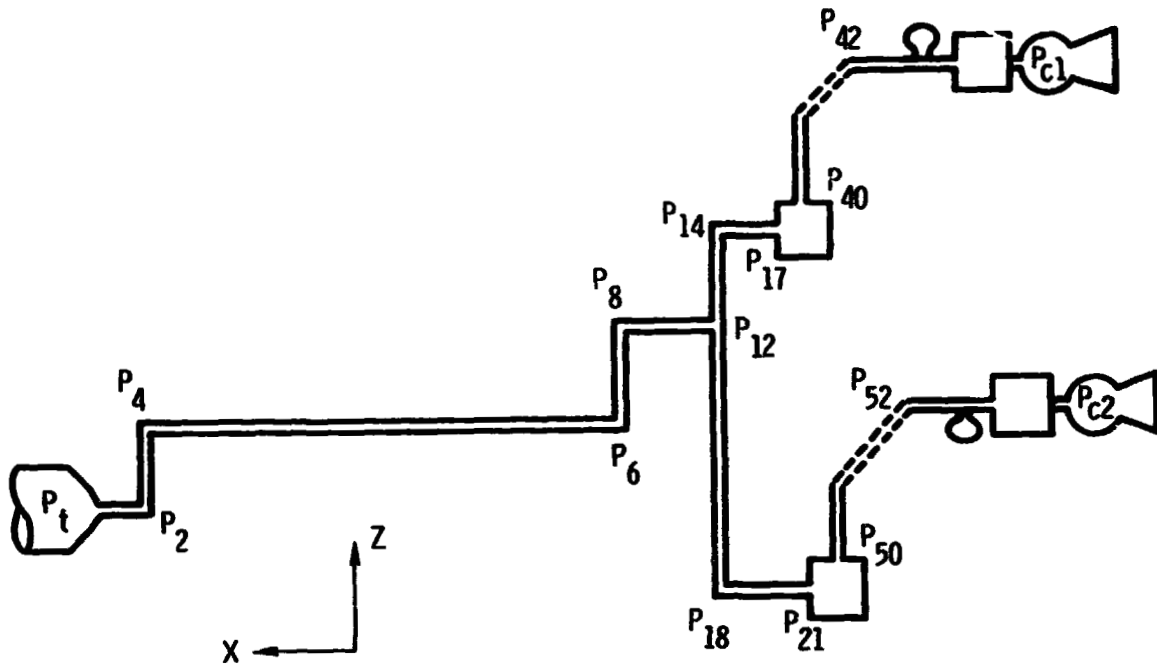
Figure A-1. MPS Fluid Pressure Variables
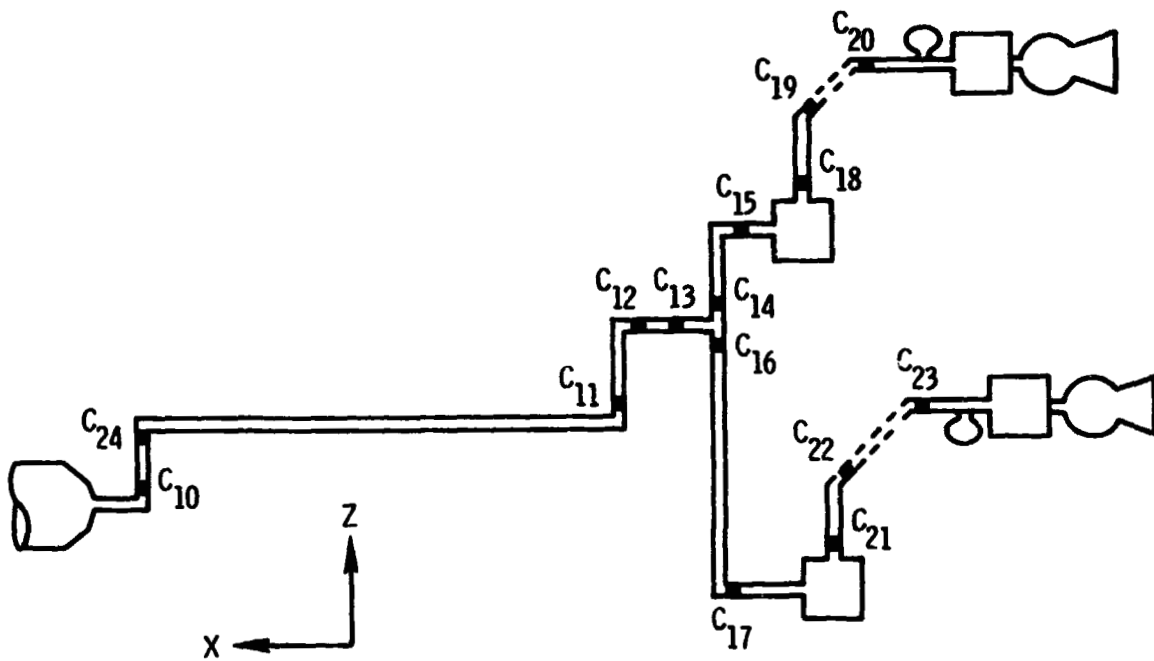
Figure A-2. MPS Distribution of Local Compliances

where L_a, ω_a and ζ_a denote the inertance, frequency (rad/sec), and damping of the accumulator, respectively. The frequency and damping ratio are defined by

$$\omega_a = (L_a C)^{-1/2}, \qquad \zeta_a = R_a C \omega_a / 2 \qquad (A-36)$$

where C and R_a denote the compliance and resistance of the accumulator. The coefficients a_{ij} are associated with the compressible flow solutions for the downcomer and are defined as follows:

$$a_{11} = a_{22} = \cosh \theta \qquad (A-37)$$

$$a_{12} = -Z_3 \frac{\sinh \theta}{\theta} \qquad (A-38)$$

$$a_{21} = -\theta \frac{\sinh \theta}{Z_3} \qquad (A-39)$$

where the parameter θ is defined by

$$\theta = s \tau \left(1 + \frac{R_3}{L_3 s} \right)^{1/2} \qquad (A-40)$$

where τ is the travel time for an acoustic wave in the downcomer segment; L_3 and R_3 denote the inertance and resistance associated with the downcomer.

The motion of the structure $\hat{X}$ is represented by a series of normal modes

$$\hat{X} = \sum_n q_n(t) \, \hat{\phi}_n(r) \qquad (A-41)$$

here $q_n(t)$ is the nth generalized coordinate and $\hat{\phi}_n(r)$ is the associated mode shape. The equation of motion for the kth generalized coordinate is

$$M_k \left| \ddot{q}_k + 2\zeta_k \omega_k \dot{q}_k + \omega_k^2 q_k \right| = \mathscr{P}_k(tb)\dot{Q}_R + P_t A_1 \phi_k^{(x)}(tb) + \sum_i \hat{F}_i \cdot \hat{\phi}_{ni} \qquad (A-42)$$

A-6

where $\mathscr{P}_k(tb)$ is the modal tank-bottom pressure and Q_R is the relative volume outflow from the propellant tank. The tank bottom pressure, P_t, is related to the vehicle motion by

$$P_t = \sum_n \mathscr{P}_n(tb) \, \ddot{q}_n \qquad (A-43)$$

The $\hat{F}_i$ comprises the drag forces on the feedline segments, the inter-pump ducts and discharge lines, the forces at the feedline corners, the forces on the LPOTP and HPOTP, and the forces on the thrust chambers.

APPENDIX B

NUMERICAL DATA FOR MPS STABILITY ANALYSIS

B.1   PROPULSION SYSTEM PARAMETERS

Resistance,[*]	MN s/m^5	(10^{-3} sec/in.^{2})
R_2	0.022	(1.32)
R_3	0.067	(3.97)
R_4	0.078	(4.62)
R_5	0.029	(1.68)
R_7	0.031	(1.81)
R_8	0.027	(1.61)
R_{10}	0.031	(1.81)
R_{11}	0.027	(1.61)
R_{40}	0.40	(23.5)
R_{41}	0.78	(46.0)
R_{42}	0.41	(24.0)
R_{43}	0.016	(9.6)
R_{50}	0.40	(23.5)
R_{51}	0.78	(46.0)
R_{52}	0.41	(24.0)
R_{53}	0.016	(9.6)
R_c	42.3	(2500)
$R_{\ell p}$	6.8	(400)
R_{hp}	44.7	(2640)
R_j	68.6	(4050)

---

[*]Resistance in SI units is based upon pressure divided by volume flow; in English units, weight flow is employed.

Inertance,[*]	10^{-3} MN s^2/m^5	$(10^{-3}$ $sec^2/in.^2)$
L_1	3.7	(0.22)
L_2	32.2	(1.9)
L_3	220.	(13)
L_4	22.0	(1.3)
L_5	14.4	(0.85)
L_6	5.1	(0.3)
L_7	22.0	(1.3)
L_8	22.0	(1.3)
L_{10}	23.7	(1.4)
L_{11}	20.4	(1.2)
L_{40}	104.	(6.0)
L_{41}	62.7	(3.7)
L_{42}	33.9	(2.0)
L_{43}	28.8	(1.7)
L_{50}	104.	(6.0)
L_{51}	62.7	(3.7)
L_{52}	33.9	(2.0)
L_{53}	28.8	(1.7)
$L_{\ell p}$	17.0	(1.0)
L_{hp}	42.4	(2.5)
L_j	84.7	(5.0)
L_a	18.6	(1.1)

---

[*]Inertance in SI units is based upon pressure divided by volume flow; in English units, weight flow is employed.

Compliance,[*]	$10^{-4} m^5/MN$	$(10^{-3} in.^2)$
C_{10}	9.6	(16.0)
C_{11}	5.6	(9.4)
C_{12}	9.6	(16.0)
C_{13}	5.2	(8.6)
C_{14}	1.8	(3.0)
C_{15}	2.3	(3.8)
C_{16}	1.9	(3.2)
C_{17}	2.3	(3.8)
C_{18}	0.36	(0.6)
C_{19}	0.6	(1.0)
C_{20}	0.45	(0.75)
C_{21}	0.36	(0.6)
C_{22}	0.6	(1.0)
C_{23}	(45	(0.75)
C_{24}	9.6	(16.0)

$\left.\begin{array}{c} C_{p1} \\ C_{p2} \end{array}\right\}$ See Table 1

Pump Gain

$\left.\begin{array}{c} m_1+1 \\ m_2+1 \end{array}\right\}$ See Table 1

Transit Time, sec

$\tau = 0.0657$

---

[*]Compliance in SI units is a volume change per unit pressure change; in English units, it is the weight of liquid displaced per unit pressure change.

Areas	$10^{-2} m^2$	$(in.^2)$
A_1	14.7	227
A_2	7.2	112
A_3	2.0	31
A_4	0.81	12.6
A_5	10.2	158

B.2   STRUCTURAL MODE DATA

Modal data are provided in the table for the second (L_2) and fifty-fourth (L_{54}) modes at liftoff. These modes proved to be of most interest in the stability calculations.

Item	L_2	L_{54}
ϕ_x (tb)	-0.0914	0.349
ϕ_x (3)	0.5659	0.232
ϕ_x (ℓ_{p1})	3.2914	16.8687
ϕ_x (ℓ_{p2})	1.389	1.8529
ϕ_x (hp1)	3.1962	11.4276
ϕ_x (hp2)	1.8797	0.5021
ϕ_x (e_1)	3.0383	12.454
ϕ_x (e_2)	1.7692	0.7461
ϕ_z (3)	-0.373	0.1963
ϕ_z (ℓ_{p1})	1.2527	-3.1785
ϕ_z (ℓ_{p2})	1.7007	1.8687
ϕ_z (e_1)	1.5065	-6.2163
ϕ_z (e_2)	1.7908	1.9191
$\mathcal{P}_k$ (tb)	-4.77×10^{-4}	-4.37×10^{-4}

The modal amplitudes in the table are normalized to a generalized mass of 1.1453×10^4 lb-sec^2/in. In the table, $\mathscr{P}_k$ (tb) refers to the modal tank-bottom pressure (given in units of lb-sec^2/in.^{3}); $\phi(e_1)$ and $\phi(e_2)$ denote the modal amplitudes at the upper and lower engine gimbal blocks, respectively.

APPENDIX C

SIMPLIFIED OMS STRUCTURAL MODEL DETAILS

Included in this appendix are the 11-DOF OMS mass and stiffness matrices, Tables C-1 and C-2, which are primarily based on RI/SD data. A summary of modal parameters for the primary axial modes and the local engine gimbal mode is presented in Table C-3.

Table C-1. OMS Pod Masses

DOF	Description	Value (lb, sec, in.)
1	RCS fuel tank - X	$0.443 + 2.116\,\nu$
2	RCS ox tank - X	$0.443 + 3.517\,\nu$
3	OMS fuel tank - X	$1.295 + 11.658\,\mu$
4	OMS ox tank - X	$1.554 + 19.248\,\mu$
5	OMS H_e tank - X	0.906
6	PCS thrusters cg - X	1.683
7	Engine X	0.649
8	Engine Y	0.649
9	Engine Z	0.649
10	Engine θ_y	3.246
11	Engine θ_z	2.247

μ denotes OMS fractional fill level

ν denotes RCS fractional fill level

Table C-2. OMS Pod Flexibility Matrix.
(lb, sec, in. units)

11 ROWS   11 COLS.

FLEX ROW COL	COL		COL		COL		COL		COL	
1 1 / 1 11	2	.262552E-04 / .290192E-06	3	.256272E-05 / .375287E-05	4	.478422E-05 / .648043E-05	5	.642912E-05 / .648043E-05	13	.295214E-05 / .057274E-07
2 2 / 2 11	2	.252277E-05 / .217711E-07	3	.289937E-04 / .644015E-05	4	.278137E-05 / .150449E-05	5	.267045E-05 / .306318E-05	10	.225872E-05 / .489245E-07
3 3 / 3 11	2	.478420E-05 / .612754E-08	3	.273137E-05 / .332125E-05	4	.117224E-04 / .180071E-06	5	.245004E-05 / .618480E-05	5	.198947E-05 / .207265E-07
4 4 / 4 11	2	.212912E-05 / .416336E-07	3	.207042E-05 / .209000E-05	4	.215024E-05 / .174939E-05	5	.364763E-05 / .257036E-05	13	.219548E-05 / .409266E-07
5 5 / 5 11	2	.205014E-05 / .241069E-06	3	.325872E-05 / .337147E-05	4	.198947E-05 / .250056E-05	5	.219243E-05 / .122412E-05	13	.083005E-04 / .49006E-05
6 6 / 6 11	2	.652345E-05 / .036957E-07	3	.262557E-05 / .268366E-05	4	.244939E-05 / .300631E-05	5	.261719E-05 / .347035E-05	5	.345753E-05 / .431495E-07
7 7 / 7 11	2	.375287E-05 / .181972E-06	3	.244016E-05 / .231321E-04	4	.382152E-05 / .143739E-05	5	.209008E-05 / .932066E-05	5	.399149E-05 / .743581E-06
8 8 / 8 11	2	.757944E-05 / .479063E-06	3	.450449E-05 / .143709E-05	4	.100071E-06 / .389293E-04	5	.174999E-05 / .243047E-05	5	.255066E-05 / .219574E-06
9 9 / 9 11	2	.648849E-05 / .187622E-08	3	.306318E-05 / .932066E-05	4	.618993E-05 / .249047E-05	5	.254016E-05 / .543559E-04	13	.122412E-05 / .114015E-05
10 10 / 10 11	2	.657274E-07 / .106029E-06	3	.494245E-07 / .743531E-06	4	.807255E-07 / .219574E-06	5	.409926E-07 / .114015E-05	13	.129006E-06 / .892515E-05
11 11 / 11 11	2	.693595E-06 / .267633E-06	3	.217711E-07 / .194975E-06	4	.912754E-06 / .479053E-06	5	.416332E-07 / .187622E-06	10	.241899E-06 / .166029E-06

Table C-3. OMS Structural Mode Summary

Fill Condition (%)		Primary Axial Mode				Engine Gimbal Mode			
OMS	RCS	Hz	M (lbm)	ϕ_{tf}	ϕ_{to}	Hz	M (lbm)	ϕ_{tf}	ϕ_{to}
100	100	10.35	5.82×10^4	1.693	2.155	44.84	284	-0.009	-0.003
	50	10.51	6.10×10^4	1.708	2.312	44.86	284	-0.008	-0.003
	1	10.60	6.42×10^4	1.716	2.430	45.03	372	-0.007	-0.001
75	100	11.57	4.14×10^4	1.631	1.922	44.85	284	-0.012	-0.004
	50	11.86	4.25×10^4	1.657	2.137	44.87	284	-0.011	-0.004
	1	12.02	4.51×10^4	1.669	2.288	45.03	357	-0.009	-0.001
50	100	13.05	3.05×10^4	1.509	1.533	44.87	284	-0.017	-0.006
	50	13.86	2.54×10^4	1.562	1.836	44.88	283	-0.017	-0.005
	1	14.20	3.22×10^4	1.579	2.037	45.04	352	-0.013	-0.002
25	100	17.62	2.21×10^4	1.433	1.139	44.93	283	-0.034	-0.010
	50	16.85	1.28×10^4	1.340	1.267	44.94	282	-0.033	-0.010
	1	18.08	1.06×10^4	1.359	1.500	45.07	338	-0.027	-0.003
10	100	25.10	6.55×10^3	0.769	1.120	45.10	282	-0.081	-0.018
	50	22.50	1.06×10^4	1.066	0.684	45.10	281	-0.079	-0.017
	1	21.87	3.88×10^3	1.026	0.874	45.16	282	-0.068	-0.007
3	100	26.16	4.49×10^3	0.547	0.472	45.58	303	-0.241	+0.002
	50	23.09	7.84×10^3	0.884	0.457	45.58	342	-0.244	+0.002
	1	23.54	3.17×10^3	0.807	0.570	45.55	296	-0.206	+0.003

APPENDIX D

OMS PROPULSION MODEL DETAILS

D. 1   FEEDLINES

In general, the allocation of nodal inertance, resistance and stiffness is accomplished in a straightforward manner based on line geometry, pressure budget and reduced bulk modulus data (accounting for pipe radial elasticity) presented in Tables D-1 and D-2. Specific complications associated with free bellows and engine manifold geometry, however, required special consideration.

The engine fuel line segment JKL and oxidizer line segment KL, respectively, have free bellows sections restrained by adjacent curved pipe sections cantilevered at the engine valve housing. The increased volumetric compliance due to the bellows is approximated on the basis of flexibility of the adjacent pipe sections illustrated in Figure D-1. The complementary strain energy due to bending is

$$U_c = \frac{1}{2} \int_0^{\theta^*} \frac{M^2}{EI} R d\theta$$

$$= \frac{1}{2} \int_0^{\theta^*} \frac{A^2 R^3 P^2}{EI} (1 - \cos\theta)^2 d\theta \qquad (D-1)$$

with θ^* equal to $\pi/2$ and π for the fuel and oxidizer circuits, respectively. In accordance with Castigliano's theorem, the volumetric compliance due to bellows is

$$\left(\frac{\theta}{P}\right)_{bellows} = \frac{1}{P} \frac{\partial U_c}{\partial P} \qquad (D-2)$$

Table D-1. OMS Fuel Circuit Hydraulic Properties

1. Line ($\rho_f = 8.138 \times 10^{-5}$ lb-sec²/in.⁴)

Segment	O.D. (in.)	t (in.)	ℓ (in.)	A (in.²)	Bulk Modulus (10⁵ psi)	Acceleration Head (in.)	ΔP (psi)
AB	1.5	0.03	11.3	1.6286	1.175	-11.3 (tank)	----
BC			20.0	3.2572*		----	4.0
CD			14.0	1.6286		-14.0 (tank)	----
DE			4.0			- 4.0 (tank)	----
EF			25.0			----	----
FG			28.0			-28.0 (gimbal)	----
GH			26.15			----	24.0
HI			13.2			+ 9.6 (gimbal)	----
IJ	1.5	0.03	8.37	1.6286	1.175	----	4.0
JKL	1.25	0.025	12.79	1.131	1.175	-10.9 (gimbal)	----
DE'	2.	0.035	7.4	2.9255	..158	----	----
E'F'	2.	0.03⁻	25.0	2.9255	1.158	+25.0 (tank)	----
F'G'	1.5	~0.03	10.0	3.2572*	1.175	---	----

2. Engine Manifold/Regen/Injector

Point/ Segment	Inertance (lb-sec²/in.⁵)	Volume (in.³)	Bulk Modulus (10⁵ psi)	Acceleration Head (in.)	ΔP (psi)
M/MN	2.85 × 10⁻⁴	37.0	1.5	- 4.0 (gimbal)	----
N/NO	9.75 × 10⁻⁴	37.0	1.5	+11.3 (gimbal)	12.5
O/OP	1.06 × 10⁻³	6.5**	1.5	+11.3 (gimbal)	73.5
P	2.70 × 10⁻⁴	N.A.	N.A.	----	7.0

*Two lines in parallel at double valve

**Estimate of stiffness includes injector structure (ΔP/ΔV ~10⁴ psi/in.³)

Table D-2. OMS Oxidizer Circuit Hydraulic Properties

1. Line ($\rho_f = 1.3525 \times 10^{-4}$ lb-sec^2/in.^{4})

Segment	O. D. (in.)	t (in.)	ℓ (in.)	A (in.^{2})	Bulk Modulus (10^5 psi)	Acceleration Head (in.)	ΔP (psi)
AB	1.5	0.03	9.6	1.6286	1.060	- 9.6 (tank)	----
BC			20.0	3.2572*		----	6.0
CD			19.6	1.6286		-16.0 (tank)	----
DE			4.0			- 4.0 (tank)	----
EF			5.4			----	----
FG			28.0			-28.0 (gimbal)	----
GH			29.445			----	34.0
HI			13.1			+13.1 (gimbal)	----
IJ	1.5	0.03	11.035	1.6286		----	7.0
JK	1.25	0.025	10.9	1.131		+ 7.02 (gimbal)	----
KL	1.25	0.025	11.13	1.131	1.060	- 2.83 (gimbal)	----
DE'	2.	0.035	6.0	2.9255	1.047	----	----
E'F'	2.	0.035	20.0	2.9255	1.047	+20. (tank)	----
F'G'	1.5	~0.03	10.0	3.2572*	1.060	----	----

2. Engine Manifold/Injector

Point/ Segment	Inertance (lb-sec^2/in.^{5})	Volume (in.^{3})	Bulk Modulus (10^5 psi)	Acceleration Head (in.)	ΔP (psi)
M/MN	3.96×10^{-4}	6.5**	1.3	----	71.0
N	4.49×10^{-4}	N.A.	N.A.	- --	7.0

*Two lines in parallel at double valve

**Estimate of stiffness includes injector structure ($\Delta P/\Delta V \sim 10^4$ psi/in.^{3})

Figure D-1. Free Bellows Dilatational Compliance Models
(R = 3.5 in., t = 0.025 in., d = 1.25 in.,
E = 3 x 10^7 psi)
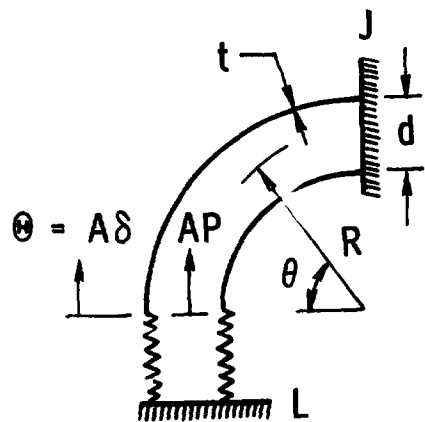
(a) FUEL
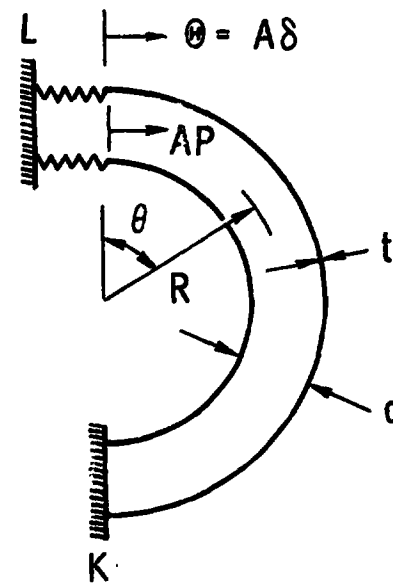
(b) OXIDIZER

For the fuel and oxidizer circuits, the respective values are

$$\left(\frac{\theta}{P}\right)_{fuel\ bellows} = \left(\frac{3\pi}{4} - 2\right)\frac{A^2 R^3}{EI} = 3.639 \times 10^{-5}\ in.^3/psi$$

(D-3)

$$\left(\frac{\theta}{P}\right)_{ox\ bellows} = \left(\frac{3\pi}{2}\right)\frac{A^2 R^3}{EI} = 4.815 \times 10^{-4}\ in.^3/psi$$

Thus, the effective hydraulic stiffnesses of the fuel line section JKL and oxidizer line section KL are approximated by

$$K_{JKL_{fuel}} = \left[\frac{\ell_{JKL} A_{JKL}}{B_{JKL}} + \left(\frac{\theta}{P}\right)_{fuel\ bellows}\right]^{-1}$$

(D-4)

$$= 6.269 \times 10^3\ psi/in.^3$$

$$K_{KL_{ox}} = \left[\frac{\ell_{KL} A_{KL}}{B_{KL}} + \left(\frac{\theta}{P}\right)_{ox\ bellows}\right]^{-1}$$

(D-5)

$$= 1.663 \times 10^3\ psi/in.^3$$

While the bellows produce significant local stiffness reduction in the feed system stiffness matrices, the effect on the propulsion system mode shapes and frequencies is small. This is due to the fact that the bellows are close to the chamber interfaces.

D.2 ENGINE MANIFOLD MODEL

The engine manifold assembly illustrated in Figure D-2 consists of a short fuel entry duct, a lower fuel distribution manifold, a fuel regenerative cooling assembly, upper fuel and oxidizer distribution manifolds, and fuel and oxidizer injector faces. A preliminary examination of the structural wall thicknesses and overall dimensions indicates that the dilatational structural compliance of the engine manifold is negligible. Therefore, compliance of the engine propellant circuitry is mainly due to the fluid bulk moduli.

FUEL

INJECTOR DETAIL

OX INLET

26.4 cm
(10.4 in.)

120 COOLANT
PASSAGES

62.5 cm
(24.6 in.)

FUEL INLET

LOWER FUEL DISTRIBUTION
MANIFOLD:

$R \approx 18$ cm (7 in.)

$A_{avg} = 5.4$ cm^2 (0.83 in.^{2})

42.2 cm
(16.6 in.)
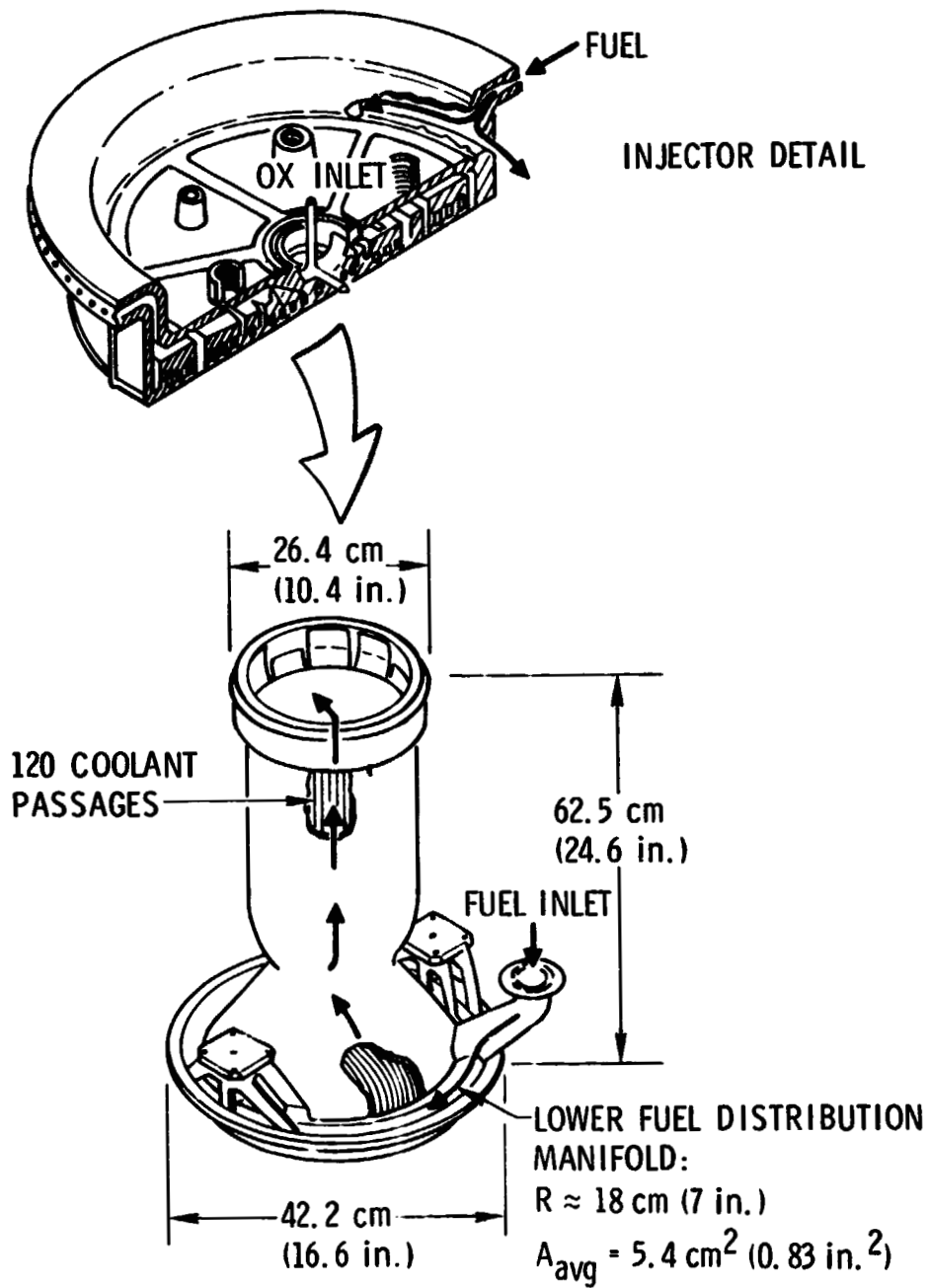
Figure D-2. OME Manifold Schematic

Calculation of the resistance and stiffness coefficients for the engine manifold model was based on volume and steady pressure drop data indicated in Tables D-1 and D-2. In contrast, estimation of the engine manifold inertance distribution was complicated by geometric details in spite of the general assumption of one-dimensional flow. A summary of component inertance values and individual methods of calculation are presented in Table D-3. The one component requiring special analytical treatment is the lower fuel distribution manifold.

On the assumption of uniform leakage flow into the regenerative cooling chamber, the circumferential manifold flow distribution is related to the fuel entry duct flow, Θ_{in}, as

$$\Theta(\theta) = \frac{\Theta_{in}}{2} \left(1 - \frac{\theta}{\pi}\right) \tag{D-6}$$

The perturbation in manifold flow kinetic energy, assuming a cross-sectional area distribution given by

$$A(\theta) = A_{avg} \left(1.5 - \frac{\theta}{\pi}\right) \tag{D-7}$$

is therefore

$$T = \frac{1}{2} \; 2 \int_0^\pi \rho \, \frac{\dot{\Theta}^2(\theta)}{A(\theta)^2} \, A(\theta) \, R d\theta \tag{D-8}$$

This results in the following expression for lower fuel manifold inertance

$$L \; \substack{\text{lower fuel} \\ \text{manifold}} = \frac{\partial^2 T}{\partial \dot{\Theta}_{in}^2} = \frac{\pi}{2} \, \frac{\rho R}{A_{avg}} \int_0^1 \frac{\left(1 - \frac{\theta}{\pi}\right)^2}{\left(1.5 - \frac{\theta}{\pi}\right)} \, d\left(\frac{\theta}{\pi}\right) \tag{D-9}$$

and numerical integration of this equation incorporating geometric data presented in Figure D-2 results in the inertance estimate given in Table D-3.

Table D-3. OME Manifold Inertance Distribution

Component	Inertance ($lb\text{-}sec^2/in.^5$)	Head (in.)	Method of Calculation
Fuel Entry Duct	2.7×10^{-4}	- 4.0	one-dimensional flow, detailed dimensions from ALRC drawing
Lower Fuel Manifold	3×10^{-4}	0	circumferential flow with uniform leakage to regenerative cooling channels, volume ~ 36 in.^{3}
Regenerative Cooling Chamber	1.65×10^{-3}	22.4	one-dimensional flow uniform distribution among channels, detailed dimensions from ALRC data, volume ~ 37 in.^{3}
Regenerative Chamber to Upper Fuel Manifold Interface	1.33×10^{-5}	0	119 holes, length ~ 0.3 in., diameter ~ 0.14 in., uniform flow distribution
Upper Fuel Manifold*	4.5×10^{-4}	0	volume ~ 6.5 in.^{3}, effective flow path length ~ 6 in.
Fuel Injector Face*	4.59×10^{-5}	0	based on ALRC supplied value for effective length/ area

*Oxidizer circuit components differ by ρ_o/ρ_f for the present analysis.

D.3 COMBUSTION DYNAMICS - APPROXIMATE STATE EQUATIONS

Since the present formulation and analysis approach requires a set of first-order, real, constant-coefficient differential equations, an approximation of Eq. (28) has been derived. The approximation was first used by us during Delta Stage II pogo studies in 1975. Relatively long time delays with τ_{df} greater than τ_{do} were originally anticipated: thus, Eq. (28) was first recast in the form

$$(1 + \tau_r s)P_c = e^{-\tau_{do}s} \bar{P}_c \qquad (D-10)$$

$$\bar{P}_c = R_{co}\dot{\Theta}_{io} + e^{-(\tau_{df} - \tau_{do})s} R_{cf}\dot{\Theta}_{if} \qquad (D-11)$$

The exponentials were then approximated in terms of fourth-order Padé expansions (Ref. 20) as

$$e^{-p} = \frac{1680 - 840p + 180p^2 - 20p^3 + p^4}{1680 + 840p + 180p^2 + 20p^3 + p^4} \qquad (D-12)$$

Substitution of the expansion into Eqs. (D-10) and (D-11) results in a pair of higher-order differential equations. Finally, incorporation of the state variable transformation described in Ref. 21 results in the set of first-order differential equations shown below. The approximation is extremely accurate for the range of parameters of interest.

$$
\begin{bmatrix} \dot{P}_c \\[4pt] \dot{x}_1 \\[4pt] \dot{x}_2 \\[4pt] \dot{x}_3 \\[4pt] \dot{x}_4 \\[4pt] \dot{x}_5 \\[4pt] \dot{x}_6 \\[4pt] \dot{x}_7 \\[4pt] \dot{x}_8 \end{bmatrix}
=
\begin{bmatrix}
-\dfrac{1}{\tau_r} & \dfrac{1}{\tau_r} & & & & & & & \\[6pt]
& & \dfrac{1}{\tau_{df}-\tau_{do}} & & & & & & \\[6pt]
& & & -\dfrac{1}{\tau_{df}-\tau_{do}} & & & & & \\[6pt]
& & & & \dfrac{1}{\tau_{df}-\tau_{do}} & & & & \\[6pt]
& \dfrac{-1680}{\tau_{df}-\tau_{do}} & \dfrac{-840}{\tau_{df}-\tau_{do}} & \dfrac{-180}{\tau_{df}-\tau_{do}} & \dfrac{-20}{\tau_{df}-\tau_{do}} & & & & \\[6pt]
& \dfrac{-40}{\tau_{df}-\tau_{do}} & & & & \dfrac{1}{\tau_{do}} & & & \\[6pt]
& \dfrac{800}{\tau_{df}-\tau_{do}} & & & & & \dfrac{1}{\tau_{do}} & & \\[6pt]
& \dfrac{-10480}{\tau_{df}-\tau_{do}} & & & & & & \dfrac{1}{\tau_{do}} & \\[6pt]
& \dfrac{99200}{\tau_{df}-\tau_{do}} & & & & \dfrac{-1680}{\tau_{do}} & \dfrac{-840}{\tau_{do}} & \dfrac{-180}{\tau_{do}} & \dfrac{-20}{\tau_{do}}
\end{bmatrix}
\begin{bmatrix} P_c \\[4pt] x_1 \\[4pt] x_2 \\[4pt] x_3 \\[4pt] x_4 \\[4pt] x_5 \\[4pt] x_6 \\[4pt] x_7 \\[4pt] x_8 \end{bmatrix}
$$

$$
+\;
\begin{bmatrix}
R_{cf}/\tau_r & R_{co}/\tau_r \\[4pt]
-40\,R_{cf}/(\tau_{df}-\tau_{do}) & \\[4pt]
800\,R_{cf}/(\tau_{df}-\tau_{do}) & \\[4pt]
-10480\,R_{cf}/(\tau_{df}-\tau_{do}) & \\[4pt]
99200\,R_{cf}/(\tau_{df}-\tau_{do}) & \\[4pt]
-40\,R_{cf}/\tau_{do} & -40\,R_{co}/\tau_{do} \\[4pt]
800\,R_{cf}/\tau_{do} & 800\,R_{co}/\tau_{do} \\[4pt]
-10480\,R_{cf}/\tau_{do} & -10480\,R_{co}/\tau_{do} \\[4pt]
99200\,R_{cf}/\tau_{do} & 99200\,R_{co}/\tau_{do}
\end{bmatrix}
\begin{bmatrix} \dot{\theta}_{if} \\[4pt] \dot{\theta}_{io} \end{bmatrix}
\qquad (D\text{-}13)
$$

D.4   CLOSED-LOOP STABILITY ANALYSIS CONSTRAINTS

Details of the constraint matrix employed in assembly of the coupled propulsion/structure system model are presented below in Table D-4.

Table D-4. OMS Closed-Loop Analysis Constraints

	Unconstrained Variable		Constrained Variable		
	Name	i	Name	j	ψ_{ij}
Fuel Line	Θ_{f1} (fuel tank I/F)	1	Θ_{f1}	1	1.
	Θ_{f2}	2	Θ_{f2}	2	1.
	Θ_{f3}	3	Θ_{f3}	3	1.
	Θ_{f4}	4	Θ_{f4}	4	1.
	Θ_{f5}	5	Θ_{f5}	5	1.
	Θ_{f6}	6	Θ_{f6}	6	1.
	Θ_{f7}	7	Θ_{f7}	7	1.
	Θ_{f8} (engine manifold I/F)	8	Θ_{f8}	8	1.
	X_{tf} (fuel tank motion)	9	X_e	21	ϕ_{tf}
	X_{bf} (fuel branch motion)	10	X_e	21	ϕ_{tf}
	X_e (engine motion)	11	X_e	21	1.
Oxidizer Line	Θ_{o1} (ox tank I/F)	12	Θ_{o1}	12	1.
	Θ_{o2}	13	Θ_{o2}	13	1.
	Θ_{o3}	14	Θ_{o3}	14	1.
	Θ_{o4}	15	Θ_{o4}	15	1.
	Θ_{o5}	16	Θ_{o5}	16	1.
	Θ_{o6}	17	Θ_{o6}	17	1.
	Θ_{o7}	18	Θ_{o7}	18	1.
	Θ_{o8} (engine manifold I/F)	19	Θ_{o8}	19	1.
	X_{to} (ox tank motion)	20	X_e	21	ϕ_{to}
	X_{bo} (ox branch motion)	21	X_e	21	ϕ_{to}
	X_e (engine motion)	22	X_e	21	1.
Engine Manifold	Θ_{ef1} (fuel line I/F)	23	Θ_{f8}	8	1.
	Θ_{ef2}	24	Θ_{f9}	9	1.
	Θ_{ef3}	25	Θ_{f10}	10	1.
	Θ_{ef4} (chamber I/F)	26	Θ_{f11}	11	1.
	Θ_{eo1} (ox line I/F)	27	Θ_{o8}	19	1.
	Θ_{eo2} (chamber I/F)	28	Θ_{o9}	20	1.
	X_e (engine motion)	29	X_e	21	1.
Pod	X_e (engine motion)	30	X_e	21	1.
	X_{tf} (fuel tank motion)	31	X_e	21	ϕ_{tf}
	X_{to} (ox tank motion)	32	X_c	21	ϕ_{to}
	Θ_{tf} (fuel tank outflow)	33	Θ_{f1}	1	1.
	Θ_{to} (ox tank outflow)	34	Θ_{o1}	12	1.

APPENDIX E

SOLUTION OF THE FIRST-ORDER DYNAMIC EQUATIONS

The dynamics of the OMS structural/propulsion system are described in terms of a set of first-order differential equations with constant coefficients of general form

$$\left| \dot{X} \right| - A \left| X \right| = B \left| F \right| \tag{E-1}$$

The matrix A is square and B is generally rectangular. For closed-loop stability analysis, the external forcing function $\left| F \right|$ is null, and for propulsion system frequency response analysis, the forcing function consists of structural interface accelerations.

The general homogeneous solution of Eq. (E-1)

$$\left| X \right| = \left| \overline{X} \right| e^{\lambda t} \tag{E-2}$$

is obtained by QR iteration (Ref. 22) which calculates the complete set of complex eigenvalues and eigenvectors. The set of column eigenvectors (ϕ) (generally complex), if numerically perfect, orthogonalize the dynamic equations as

$$\left(\diagdown \lambda \diagdown \right) \left| \xi \right| - \left(\phi^{-1} A \phi \right) \left(\xi \right) = 0 \tag{E-3a}$$

with

$$\left| X \right| = \phi \left| \xi \right| \tag{E-3b}$$

Evaluation of the numerical accuracy of the complex modal solution is accomplished by application of the Gerschgorin theorem (Ref. 22) which yields the following information:

a. Diagonal entries in $\phi^{-1}A\phi$ represent improved estimates of the eigenvalues, λ

b. Off-diagonal row and column sums

$$r_k = \sum_{\substack{j=1,n \\ j \neq k}} \left(\phi^{-1}A\phi\right)_{ij} \qquad \text{(E-4a)}$$

$$c_k = \sum_{\substack{i=1,n \\ i \neq k}} \left(\phi^{-1}A\phi\right)_{ij} \qquad \text{(E-4b)}$$

yield a radius R_k about $\left(\phi^{-1}A\phi\right)_{kk}$ within which the true eivenvalue λ_k must lie.

The maximum radius

$$R_k = \max(r_k, c_k) \qquad \text{(E-5)}$$

is used to assess accuracy of the eigenvalue, λ_k. The overall accuracy of the numerical eigenvalue solutions is evaluated based on the smallness of the radii and the shifts $\left[\lambda_k - \left(\phi^{-1}A\phi\right)_{kk}\right]$.

Modal forced response of Eq. (E-1) is conveniently calculated with knowledge of the homogeneous solutions. In the present study, frequency response subject to the harmonic forcing function

$$\left|F\right| = \left|F_o\right| e^{i\omega t} \qquad \text{(E-6)}$$

is required for study of propulsion system dynamics and open-loop stability.
The steady state modal dynamic solution of Eq. (E-1) incorporating Eq. (E-3b)
is

$$\left| \bar{X}(\omega) \right| = \phi \left(\frac{1}{i\omega - \lambda_k} \right) \phi^{-1} B \left| F_o \right| \qquad (E-7a)$$

Although truncated modal solutions may be calculated, the frequ ncy responses
calcul.ted in the present study include the contribution of all n des.

APPENDIX F

ERROR ANALYSIS OF TRANSFER FUNCTION MEASUREMENTS[*]

This is a summary of work conducted to analyze errors in transfer function (frequency response) measurements based upon noise/signal considerations and coherence functions between the measured data. Quantitative formulas are obtained that give the standard error in transfer function estimates obtained by using an external excitation signal. Proper interpretation of measured results depends upon evaluation of quantities discussed in this appendix.

F. 1 GENERAL DIAGRAM AND NOTATION

A diagram is shown in Figure F-1 of a general system whose transfer function $H_{xy}(f)$ is to be determined. Quantities in Figure F-1 have the following meanings:[**]

$i(t)$	=	measured external excitation signal
$u(t)$	=	input signal caused by $i(t)$
$v(t)$	=	output signal caused by $i(t)$
$m(t)$	=	input self-noise independent of $i(t)$
$n(t)$	=	output self-noise independent of $i(t)$
$x(t)$	=	measured input signal = $u(t) + m(t)$
$y(t)$	=	measured output signal = $v(t) + n(t)$

A special case of Figure F-1 occurs when $i(t) = 0$, corresponding to self-noise only, where $x(t) = m(t)$ and $y(t) = n(t)$. For this case, the transfer function $H_{xy}(f)$ will be denoted by $H_{mn}(f)$.

---

[*] The author of this appendix is J.S. Bendat, acting as a consultant to The Aerospace Corporation.

[**] An example of application to the CTL-V testing: $i(t)$ is the electrical signal to the suction pulser; $x(t)$ and $y(t)$ are the inlet pressure and flow to the LPOTP, respectively. The transfer function is one of those required for four-terminal definition of the LPOTP.
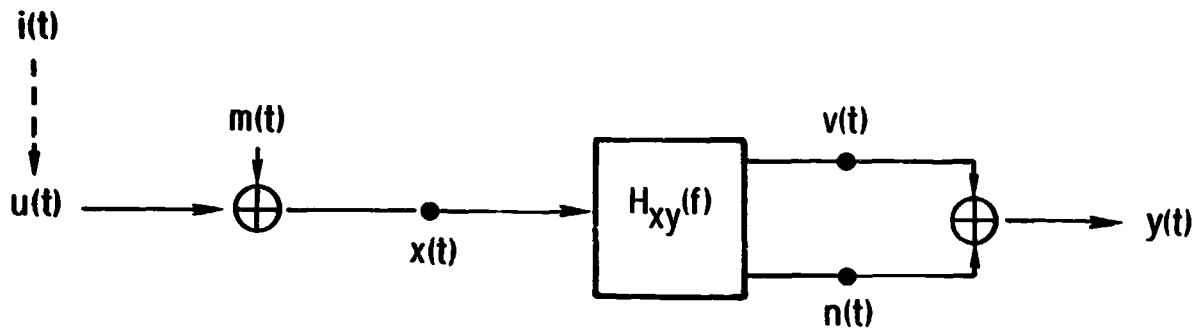
Figure F-1. System with External Excitation

From the measured signals, i(t), x(t) and y(t), autospectral (power spectral) density functions, cross-spectral density functions, and coherence functions can be computed. These will be denoted by:

$G_{xx}(f)$ = autospectral density function of x(t)

$G_{xy}(f)$ = cross-spectral density function between x(t) and y(t)

$\gamma^2_{xy}(f)$ = coherence function between x(t) and y(t)

with similar notations for $G_{yy}(f)$, $G_{ii}(f)$, $G_{ix}(f)$, $G_{iy}(f)$, $\gamma^2_{ix}(f)$ and $\gamma^2_{iy}(f)$. The coherence function between x(t) and y(t) is defined by

$$\gamma^2_{xy}(f) = \left| G_{xy}(f) \right|^2 \Big/ G_{xx}(f) G_{yy}(f) \qquad (F-1)$$

with similar definitions for $\gamma^2_{ix}(f)$ and $\gamma^2_{iy}(f)$.

As is well known, for any frequency f, $\gamma^2_{xy}(f)$ is bounded between 0 and 1 and is a measure of an ideal (constant parameter) linear relationship between x(t) and y(t).

The dependence upon f will now be omitted in all the following for-mulas for simplicity in notation, but should not be forgotten. For Figure F-1, since the self-noise terms m(t) and n(t) are independent of u(t) and v(t)

$$G_{xx} = G_{uu} + G_{mm}, \qquad G_{yy} = G_{vv} + G_{nn}, \qquad G_{xy} = G_{uv} + G_{mn} \tag{F-2}$$

Define the input noise-to-signal ratio a and the output noise-to-signal ratio β by

$$a = G_{mm}/G_{uu}, \qquad \beta = G_{nn}/G_{vv} \tag{F-3}$$

Then

$$G_{xx} = G_{uu}(1+a), \qquad G_{yy} = G_{vv}(1+\beta) \tag{F-4}$$

the coherence function γ_{xy}^2 is given by

$$\gamma_{xy}^2 = \left| G_{uv} + G_{mn} \right|^2 / G_{uu} G_{vv}(1+a)(1+\beta) \tag{F-5}$$

Thus, the coherence function is clearly a function of a and β, as well as the other terms shown.

F.2   SINGLE INPUT/SINGLE OUTPUT MODELS

For simple single-input/single-output models, where x(t) is a meas-ured stationary random input signal and y(t) is its associated measured output, the optimum constant parameter linear system between x(t) and y(t) has a transfer (frequency response) function given by

$$H_{xy} = G_{xy}/G_{xx} \tag{F-6}$$

In polar form

$$H_{xy} = \left| H_{xy} \right| e^{-j\phi_{xy}}$$ (F-7)

with gain factor $\left| H_{xy} \right|$ and phase factor ϕ_{xy}.

The output autospectral (power spectral) density function G_{yy} can be decomposed into two parts (see Figure F-2)

$$G_{yy} = \left| H_{xy} \right|^2 G_{xx} + G_{zz}$$ (F-8)

where

$$\left| H_{xy} \right|^2 G_{xx} = \gamma_{xy}^2 G_{yy}$$ (F-9)

is called the <u>coherent output power spectrum</u> and represents the portion of y(t) due to x(t). The second term

$$G_{zz} = \left(1 - \gamma_{xy}^2 \right) G_{yy}$$ (F-10)

represents the portion of y(t) due to unknown z(t) caused by extraneous noise, nonlinear effects, etc. Note that G_{zz} approaches zero as the coherence function γ_{xy}^2 approaches one.
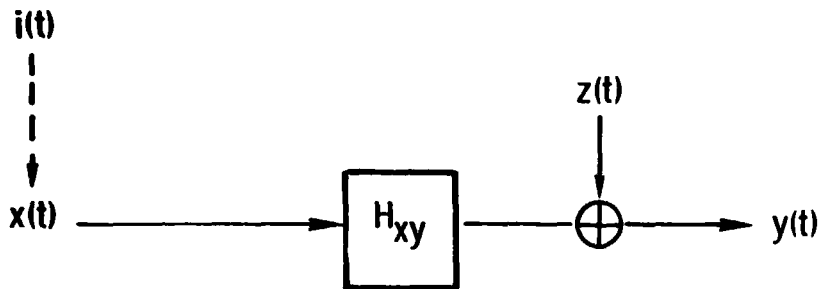

Figure F-2. Single-Input/Single-Output Model

Estimates of H_{xy} can be found by means of Equation (F-6) which do not involve the use of any external excitation signal i(t). These estimates will always be <u>biased</u> if extraneous noise is present at the input. By using i(t), however, it is possible to obtain unbiased estimates of H_{xy}. This will now be shown.

F.3   TRANSFER FUNCTION ESTIMATES USING EXTERNAL EXCITATION

The Fourier transform relation of Figure F-2, indicated by capital letters, is given by

$$Y = H_{xy}X + Z \qquad (F-11)$$

where all terms in Equation (F-11) are functions of frequency. When the external excitation signal i(t) is available, Equation (F-11) yields the result

$$G_{iy} = H_{xy}G_{ix} + G_{iz} \qquad (F-12)$$

Hence if the "expected value" of G_{iz} (denoted by $E[G_{iz}]) \approx 0$, which is a reasonable expectation in these applications, then

$$\hat{H}_{xy} = G_{iy}/G_{ix} \qquad (F-13)$$

will provide an <u>unbiased</u> estimate of H_{xy}. From Equation (F-12) observe that

$$\hat{H}_{xy} = H_{xy} + \left(G_{iz}/G_{ix}\right) \qquad (F-14)$$

Equation (F-13) will be used instead of Equation (F-6) to obtain estimates of the desired transfer function H_{xy}. The variance error in these estimates will now be indicated.

Assume that $\left| G_{iz} \right| \ll \left| G_{ix} \right|$, where $\left| G_{ix} \right|$ is essentially a large constant. Then

$$E\left[\left| \hat{H}_{xy} - H_{xy} \right|^2 \right] = E\left[\left| G_{iz}/G_{ix} \right|^2 \right] \approx E\left[\left| G_{iz} \right|^2 \right] \Big/ \left| G_{ix} \right|^2 \qquad (F-15)$$

It is also reasonable to assume that estimates of G_{iz} will be obtained by averaging over n_d independent estimates.[*] It then follows that (Ref. 23, p. 185)

$$E\left[\left| G_{iz} \right|^2 \right] \leqq G_{ii} G_{zz}/n_d \qquad (F-16)$$

The quantity

$$\left| G_{ix} \right|^2 = \gamma_{ix}^2 G_{ii} G_{xx} \qquad (F-17)$$

Hence, Equation (F-15) becomes

$$E\left[\left| \hat{H}_{xy} - H_{xy} \right| \right]^2 \leqq \hat{r}^2 \qquad (F-18)$$

where

$$\hat{r}^2 = G_{zz}/n_d \gamma_{ix} G_{xx} \approx \left(1 - \gamma_{xy}^2 \right) G_{yy} \Big/ n_d \gamma_{ix}^2 G_{xx} \qquad (F-19)$$

using Equation (F-10) for G_{zz}. Note that all terms in Equation (F-19) are measurable quantities.

Geometrically, Equation (F-18) describes a circle of radius $\hat{r}$ centered at $\hat{H}(f)$ as pictured in Figure F-3. In terms of the gain factor estimate $\left| \hat{H} \right|$

---

[*]The use of multiple estimates is employed in the fast Fourier transform (FFT) type of spectral analysis; more generally the term n_d can be replaced by the $B_e T$ product, where B_e is the effective analysis bandwidth and T is the total duration of the record. See Equation (F-47).

and the phase factor estimate $\hat{\phi}$, if $\hat{r} < |\hat{H}|$ then the "approximate" 68% confidence intervals for the actual gain factor $|H|$ and phase factor ϕ are given by

$$|\hat{H}| - \hat{r} \le |H| \le |\hat{H}| + \hat{r}$$

$$\hat{\phi} - \Delta\hat{\phi} \le \phi \le \hat{\phi} + \Delta\hat{\phi} \qquad \text{(F-20)}$$

where

$$\Delta\hat{\phi} = \sin^{-1}(\hat{r}/|\hat{H}|) \qquad \text{(F-21)}$$
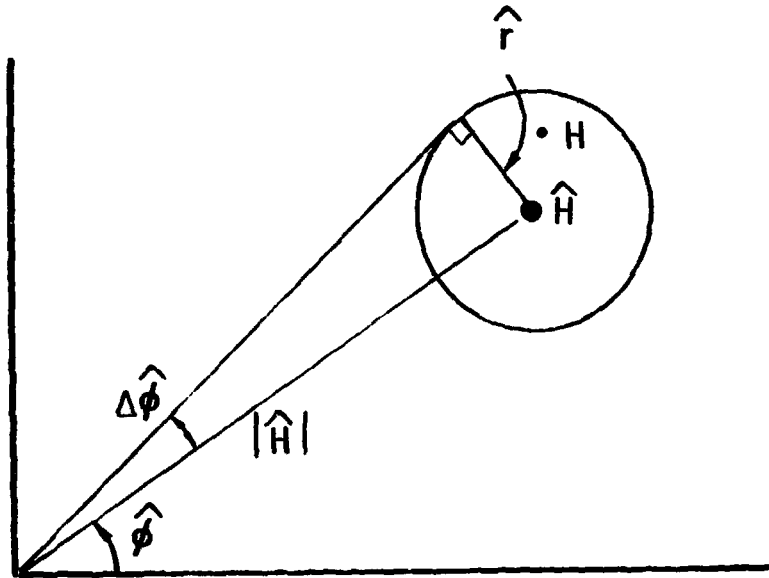

Figure F-3. Confidence Interval for Transfer Function Estimates

The standard error in these results can be estimated by ϵ where

$$\epsilon = \hat{r} \big/ |H| \approx \left(1 - \gamma_{xy}^2\right)^{1/2} \big/ n_d^{1/2} \; \gamma_{ix} \gamma_{xy} \tag{F-22}$$

using Equation (F-9) for $|H|$. For small ϵ, to obtain the "approximate" 95% confidence intervals for gain and phase, the radius $\hat{r}$ should be replaced by $2\hat{r}$ in Equations (F-20) and (F-21).

F.4 ESTIMATION OF NOISE-TO-SIGNAL RATIOS USING EXTERNAL EXCITATION

From $x(t) = u(t) + m(t)$ and $y(t) = v(t) + n(t)$, when $u(t)$ and $v(t)$ are due to $i(t)$, and $m(t)$ and $n(t)$ are independent of $i(t)$, it follows that

$$G_{ix} = G_{iu} + G_{im} = G_{iu} = A_{iu} G_{ii}, \qquad G_{iy} = G_{iv} + G_{in} = G_{iv} = B_{iv} G_{ii} \tag{F-23}$$

where A_{iu} and B_{iv} would be computed transfer functions. The quantities G_{uu} and G_{vv} then become

$$G_{uu} = \left| A_{iu} \right|^2 G_{ii} = \gamma_{ix}^2 G_{xx}, \qquad G_{vv} = \left| B_{iv} \right|^2 G_{ii} = \gamma_{iy}^2 G_{yy} \tag{F-24}$$

Now $G_{xx} = G_{uu} + G_{mm}$ and $G_{yy} = G_{vv} + G_{nn}$ give

$$G_{mm} = \left(1 - \gamma_{ix}^2\right) G_{xx}, \qquad G_{nn} = \left(1 - \gamma_{iy}^2\right) G_{yy} \tag{F-25}$$

Hence the noise-to-signal ratios

$$a = G_{mm}/G_{nn} = \left(1 - \gamma_{ix}^2\right)\big/\gamma_{ix}^2, \qquad \beta = G_{nn}/G_{vv} = \left(1 - \gamma_{iy}^2\right)\big/\gamma_{iy}^2 \tag{F-26}$$

Conversely, Equation (F-26) proves that

$$\gamma^2_{ix} = 1/(1+a), \qquad \gamma^2_{iy} = 1/(1+\beta) \qquad \text{(F-27)}$$

Note that $a = \beta$ if and only if $\gamma^2_{ix} = \gamma^2_{iy}$.

Values of γ^2_{ix} and γ_{ix} for various values of a as might be used in Equation (F-22) are shown in Table F-1.

Table F-1. γ^2_{ix} versus a [Eq. (F-27)]

a	γ^2_{ix}	γ_{ix}
0.05	0.952	0.976
0.10	0.909	0.953
0.15	0.870	0.933
0.20	0.833	0.913
0.25	0.800	0.894

F.5   SELF-NOISE CASE

The self-noise case corresponds to $i(t) = 0$ with $u(t) = 0$ and $v(t) = 0$. For this case, $x(t) = m(t)$ only and $y(t) = n(t)$ only. Here

$$G_{xx} = G_{mm}, \qquad G_{yy} = G_{nn}, \qquad G_{xy} = G_{mn} \qquad \text{(F-28)}$$

Equation (F-1) now yields

$$\gamma^2_{xy} = \gamma^2_{mn} = \left| G_{mn} \right|^2 \Big/ G_{mm} G_{nn} \qquad \text{(F-29)}$$

From Equation (F-6)

$$H_{xy} = H_{mn} = G_{mn}/G_{mm} \qquad \text{(F-30)}$$

with associated $\left| H_{mn} \right|$ and ϕ_{mn}.

F-9

These estimates of γ^2_{mn}, $\left| H_{mn} \right|$ and ϕ_{mn} should be compared to estimates of γ^2_{xy}, $\left| H_{xy} \right|$ and ϕ_{xy} found when signals are present due to $i(t)$. In particular, poor estimates of H_{mn} will be obtained if γ^2_{mn} is small.

F.6   HYPOTHETICAL NO-NOISE CASE

In this hypothetical case, it will be assumed that $m(t) = 0$ and $n(t) = 0$ so that $x(t) = u(t)$ and $y(t) = v(t)$. Here, Equation (F-1) yields

$$\gamma^2_{xy} = \gamma^2_{uv} = \left| G_{uv} \right|^2 \Big/ G_{uu} G_{vv} \qquad \text{(F-31)}$$

with $\gamma^2_{uv} = 1$ under ideal conditions. From Equation (F-6)

$$H_{xy} = H_{uv} = G_{uv} / G_{uu} \qquad \text{(F-32)}$$

with associated $\left| H_{uv} \right|$ and ϕ_{uv}.

These estimates of $\left| H_{uv} \right|$, ϕ_{uv} and $\gamma^2_{uv} = 1$ will be considered to be the desired (unknown) true values of H_{xy}.

F.7   GENERAL CASE OF CORRELATED NOISE

It is assumed here that the noise terms $m(t)$ and $n(t)$ are partially correlated with each other but not with the signals $u(t)$ and $v(t)$ that are due to $i(t)$. This case is covered by Equations (F-1) through (F-5). It is reasonable to assume that the two terms in $G_{xy} = G_{uv} + G_{mn}$ satisfy

$$\left| G_{mn} \right| < \left| G_{uv} \right| \qquad \text{(F-33)}$$

Bounds for γ^2_{xy} of Equation (F-5) will now be developed.

Two special situations can occur corresponding to $\left| G_{mn} \right|$ being parallel to $\left| G_{uv} \right|$ or $\left| G_{mn} \right|$ being perpendicular to $\left| G_{uv} \right|$.

Case A. $|G_{mn}|$ parallel to $|G_{uv}|$

For this situation

$$\left| G_{xy} \right| = \left| G_{uv} + G_{mn} \right| = \left| G_{uv} \right| \pm \left| G_{mn} \right| \qquad \text{(F-34)}$$

with $\phi_{xy} = \phi_{uv}$ as shown in Figure F-4.
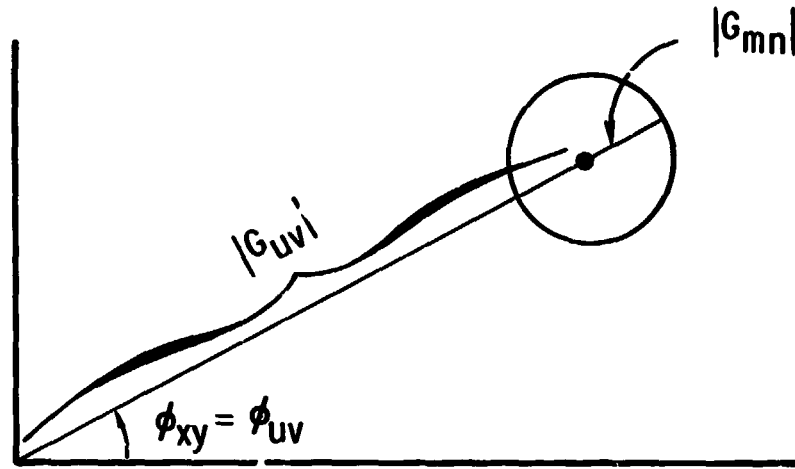
Figure F-4. $\left| G_{mn} \right|$ Parallel to $\left| G_{uv} \right|$

It follows that

$$\left| G_{xy} \right|^2 = \left| G_{uv} \right|^2 \left[1 \pm \left| G_{mn} \right| \Big/ \left| G_{uv} \right| \right]^2 = G_{uu} G_{vv} \left[1 \pm \gamma_{mn} (\alpha\beta)^{1/2} \right]^2 \qquad \text{(F-35)}$$

by setting

$$\left| G_{mn} \right|^2 = \gamma_{mn}^2 G_{mm} G_{nn}, \qquad \left| G_{uv} \right|^2 = G_{uu} G_{vv} \qquad \text{(F-36)}$$

$$\alpha = G_{mm}/G_{nn}, \qquad \beta = G_{nn}/G_{vv} \qquad \text{(F-37)}$$

Now, the coherence function γ_{xy}^2 of Equation (F-5) becomes

$$\gamma_{xy}^2 = \left[1 \pm \gamma_{mn}(\alpha\beta)^{1/2} \right]^2 \bigg/ (1+\alpha)(1+\beta) \qquad \text{(F-38)}$$

The maximum reduction in measured coherence will occur by choosing the minus sign in the numerator and by letting γ_{mn} approach one. Assuming $\alpha = \beta$, this will yield the lowest possible results

$$\gamma_{xy}^2 \approx (1-\alpha)^2 / (1+\alpha)^2 \qquad \text{(F-39)}$$

Values of γ_{xy}^2 and γ_{xy} for various values of α as might be used in Equation (F-22) are shown in Table F-2.

Table F-2. Minimum γ_{xy}^2 versus α [Eq. (F-39)]

α	γ_{xy}^2	γ_{xy}
0.05	0.819	0.905
0.10	0.669	0.818
0.15	0.546	0.739
0.20	0.444	0.667
0.25	0.360	0.600

Case B. $|G_{mn}|$ perpendicular to $|G_{uv}|$

For this situation

$$\left| G_{xy} \right|^2 = \left| G_{uv} + G_{mn} \right|^2 = \left| G_{uv} \right|^2 - \left| G_{mn} \right|^2 \qquad \text{(F-40)}$$

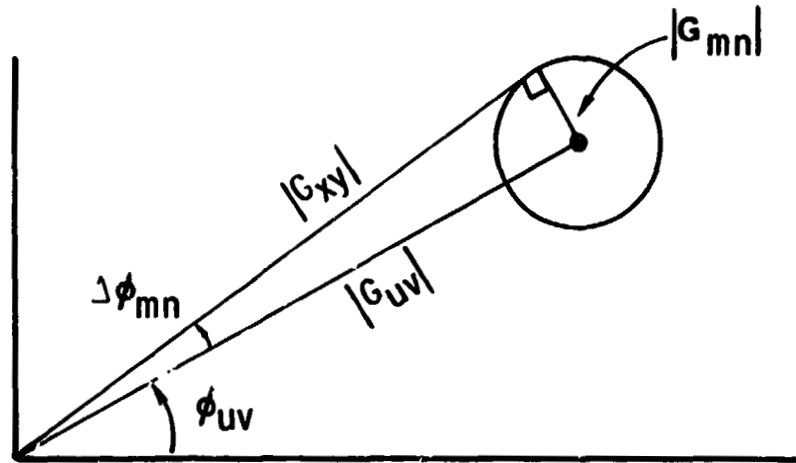with $\phi_{xy} = \phi_{uv} \pm \Delta\phi_{mn}$ as shown in Figure F-5.

Figure F-5. $|G_{mn}|$ Perpendicular to $|G_{uv}|$

By using Equations (F-36) and (F-37), it follows that

$$\left| G_{xy} \right|^2 = G_{uu} G_{vv} \left[1 - \gamma^2_{mn} \, \alpha\beta \right] \qquad (F-41)$$

Hence the coherence function γ^2_{xy} of Equation (F-5) becomes here

$$\gamma^2_{xy} = \left(1 - \gamma^2_{mn} \alpha\beta \right) \Big/ (1+\alpha)(1+\beta) \qquad (F-42)$$

As before, the maximum reduction in measured coherence will occur by letting γ_{mn} approach one. Assuming $\alpha = \beta$, this will yield the results

$$\gamma^2_{xy} \approx (1-\alpha^2)/(1+\alpha)^2 \qquad (F-43)$$

Values of γ^2_{xy} and γ_{xy} for various values of α as might be used in Equation (F-22) are shown in Table F-3.

Table F-3. Expected γ_{xy}^2 versus a [Eq. (F-43)]

a	γ_{xy}^2	γ_{xy}
0.05	0.905	0.951
0.10	0.818	0.905
0.15	0.739	0.860
0.20	0.667	0.817
0.25	0.600	0.775

F.8 STANDARD ERROR IN TRANSFER FUNCTION ESTIMATES

Return now to Equation (F-22) which gives the standard error ϵ in transfer function estimates $\hat{H}$ that are obtained by using the external excitation signal as given by Equation (F-13). Maximum values of ϵ will occur when γ_{xy}^2 and γ_{ix}^2 take on their minimum values. This will occur for γ_{xy}^2 from Equation (F-39) and for γ_{ix}^2 from Equation (F-27). Substitution of these results into Equation (F-22) gives

$$\epsilon \leq \frac{2}{(1-a)} \left[\frac{a(1+a)}{n_d} \right]^{1/2} \tag{F-44}$$

indicating how ϵ varies as a function of n_d and a.

To illustrate use of Equation (F-44), suppose $a = 0.10$, corresponding to $\gamma_{ix}^2 \approx 0.909$ and $\gamma_{xy}^2 \approx 0.669$ from Tables F-1 and F-2. Now

$$\epsilon \leq \frac{0.74}{\sqrt{n_d}}$$

Hence $n_d = 25$ gives $\epsilon \leq 14.7\%$ and $n_d = 100$ gives $\epsilon \leq 7.4\%$. In terms of ϵ, there will be about 68% confidence that measured values of $|\hat{H}|$ will be within $\pm \epsilon\%$ of the desired unknown true values $|H|$, and there will be about 95% confidence that measured values of $|\hat{H}|$ will be within $\pm 2\epsilon\%$ of the desired $|H|$.

Note that for small values of a, Equation (F-44) can be approximated by

$$\epsilon \leq 2\left(\frac{a}{n_d}\right)^{1/2} \tag{F-45}$$

F.9 RELATION OF NUMBER OF AVERAGES TO NOISE-TO-SIGNAL RATIOS

The number of n_d of independent averages can be related to the total available record length T_{total} by the formula

$$T_{total} = n_d T \tag{F-46}$$

where the subrecord length $T = 1/B_e$, the quantity B_e being the bandwidth resolution. Hence

$$n_d = T_{total}/T = B_e T_{total} \tag{F-47}$$

Multiplying numerator and denominator of the expression for the noise-to-signal ratio a in Equation (F-26) by B_e yields

$$a = G_{mm} B_e \Big/ \overline{u^2} = 2 G_{mm} B_e \Big/ u_o^2 \tag{F-48}$$

where $\overline{u^2}$ is the mean square value of $u(t)$ and u_o is the amp_l_ude of $u(t)$ if it is a sinusoid.

Substitution of Equation (F-47) into Equation (F-48) shows

$$a = G_{mm} n_d \Big/ \overline{u^2} T_{total} = 2 G_{mm} n_d \Big/ u_o^2 T_{total} \tag{F-49}$$

Thus, a increases as n_d increases and a decreases as T_{total} increases. Also, Equation (E-45) becomes now

$$\epsilon \leq 2\left[G_{mm}\Big/ \overline{u^2} T_{total}\right]^{1/2} = 2\left[2 G_{mm}\Big/ u_o^2 T_{total}\right]^{1/2} \tag{F-50}$$

where G_{mm} would be measured by Equation (F-25).

REFERENCES

1. Rubin, S., R.G. Wagner, and J.G. Payne, "Pogo Suppression on Space Shuttle--Early Studies," NASA CR-2210, March 1973.

2. Lock, M.H., and S. Rubin, "Passive Suppression of Pogo on the Space Shuttle," NASA CR-132452, April 1974.

3. Lock, M.H., and S. Rubin, "Active Suppression of Pogo on the Space Shuttle," NASA CR-134749, October 1974.

4. Lock, M.H., and S. Rubin, "Analysis of Pogo on the Space Shuttle: Accumulator Design Guidelines and Planar Multiengine Model Development," Report No. ATR-76(7475)-1, The Aerospace Corporation, El Segundo, California, September 1976.

5. "Prevention of Coupled Structure-Propulsion Instability (Pogo), NASA Space Vehicle Design Criteria (Structures)," NASA SP-8055, October 1970.

6. Ng, S., "Dynamic Response of Cavitating Turbomachines," Report No. E 183.1, Division of Engineering and Applied Science, California Institute of Technology, August 1976.

7. Payne, J.G., and S. Rubin, "Pogo Suppression on the Delta Vehicle," Report No. TR-0074(4704)-1, The Aerospace Corporation, El Segundo, California, June 1974.

8. Holt, J.F., "ACS Mule, General Root Finding Subroutine," Report No. TOR-0073(9320)-8, The Aerospace Corporation, El Segundo, California, March 1973.

9. "SSME Model, Engine Dynamic Characteristics Related to Pogo," Report No. RSS-8549-2, Rocketdyne Division, Rockwell International, Canoga Park, California, September 1973.

10. Ghahremani, F.G., and S. Rubin, "Empirical Evaluation of Pump Inlet Compliance," Report No. ATR-73(7257)-1, The Aerospace Corporation, El Segundo, California, August 1972.

11. Rockwell International Space Division, "Space Shuttle Pogo Data Manual," Report No. SD-74-SH-0111-A, December 1975.

12. Rockwell Internal Letter SSP/VSD-76-68, HGVT Quick Look Report, from L.S. Nogawski to R.H. Lassen, Rockwell International Space Division, Downey, California, 26 August 1976.

REFERENCES (Continued)

13. Brennan, C., and A.J. Acosta, "The Dynamic Transfer Function for a Cavitating Inducer," Journal of Fluids Engineering, Vol. 98, June 1976.

14. Anderson, D.A., R.J. Blade, and W. Stevans, "Response of a Radial-Bladed Centrifugal Pump to Sinusoidal Disturbances for Noncavitating Flow," NASA TN D-6556, December 1971.

15. Markowitz, M., and M.J. Morgan, "Delta Second Stage Pogo Analysis Report," MDAC Report A3-222-Delta-76-TM-2, September 1976 (Also summarized in "Solution to Delta Vehicle Second Stage Pogo Problem," MDAC WD Paper 2707, March 1977).

16. Estoueig, C., and J.J. Dordain, "Analyse de l'Effet du Lanceur Francais Diamant-B," No. 73.09/73 DLA/ED/EG, Centre National d'Etudes Spatiales, Bretigny-sur-Orge, France, 21 September 1973.

17. Pinson, L.D., "Longitudinal Spring Constants for Liquid-Propellant Tanks with Ellipsoidal Ends," NASA TN D-2220, November 1964.

18. Guyan, R.J., "Reduction of Stiffness and Mass Matrices," AIAA Journal, Vol. 3, No. 2, July 1971, pp. 1255-1261.

19. Harrje, David T., (ed.), "Liquid Propellant Rocket Combustion Instability," NASA SP-194, 1972.

20. Lanczos, C., Applied Analysis, Prentice-Hall, Inc., Englewood Cliffs, New Jersey (1956), p. 426.

21. DeRusso, P.M., R.J. Roy, and C.M. Close, State Variables for Engineers, John Wiley and Sons, New York (1965), pp. 333-336.

22. Isaacson, E., and H.E. Keller, Analysis of Numerical Methods, John Wiley and Sons, New York (1966), pp. 158-175, 135-140.

23. Bendat, J.S., and A.G. Piersol, Random Data, John Wiley and Sons, New York (1976).